The hyperthermal atomic oxygen beam interaction with solid surfaces and its application to low temperature oxidation processes

Hiroshi Kinoshita

The hyperthermal atomic oxygen beam interaction with solid surfaces and its application to low temperature oxidation processes

超熱原子状酸素ビームと固体表面との相互作用
およびその低温酸化プロセスへの応用

Hiroshi Kinoshita
木之下博

Contents

Introduction

About 50 years ago, we got space activities. Now, the activities are part of our life and are going to be larger and larger. Almost all the space activities are carried out near Earth, i. e., in Earth orbits. An altitude of 150 km is the lowest altitude at which a satellite in a circular orbit can orbit the Earth for at least one revolution without propulsion. Space shuttle and International Space Station can fly only near the orbits and these orbits are called low Earth orbit (LEO). The pressure in the LEO environment is about 10^{-6} ~ 10^{-8} Pa, which is far from a complete vacuum. The dominant species in the LEO environment is atomic oxygen (AO; ground state neutral). The orbital velocity of spacecraft is 8 km/s which corresponds to a mean AO collision energy of ~4.8 eV, and the actual flux of AO facing the orbital direction is quite high (~10^{15} atoms/cm^2)[1]. Therefore, spacecraft surfaces facing the orbital direction (ram surface) experience both very high energy and high flux with AO.

Space shuttle is the first reused spacecraft, i. e., can return directly from space. Furthermore, space shuttle has a cargo-bay in which the interior surface can be directed to ram direction by opening the bay, and the interior surface of the cargo-bay was not affected by the heat in reentry phase. After early space shuttle flight, it was discovered that some materials in the cargo-bay (mainly carbon-based materials, organic films, and tribological materials) showed surface degradations after a space flight[2]. The material degradations in the LEO environment are mainly observed in the surfaces facing the orbital direction. Considering this "ram effect", the degradation phenomenon was considered to be caused by hyperthermal AO collision[3]. After that, material exposure experiments in the LEO environment using space shuttle[4-10] and ground-based simulations[11-24] were started in order to predict the reliability of materials and to achieve low risk missions.

The samples in flight and ground-based experiments have mainly been selected from the practical materials for space use such as polymeric materials or paints. This is because the behavior of the space systems in the LEO environment is need to know in order to achieve low risk mission. Namely, the same materials, that would be used as a part of real space system, were exposed and tested in a real space environment. However, the problem was that the materials actually used in a space system are too wide variety and too much

complicated. It is not cost effective and not realistic that all of the candidate materials are tested in a real space environment. Therefore, the physics and chemistry that occur on the material surfaces in LEO must be researched to predict the reliability of the materials. In the case of material degradation due to AO attacks, the knowledge regarding AO reactivity with the materials is not clear enough to predict the reliability of the materials even after a number of research was carried out. The reason is the difficulty for simulating AO environment in the ground-based facilities.

Conventional methods for simulating AO environment in LEO, for example plasma asher, supersonic molecular beam, or ion beam methods, do not provide both high translational energy of 5 eV and of high flux of 10^{12} atoms/cm^2/s at the same time. However recent development of the laser detonation-type AO source, which is pioneered by Caledonia et al. [25-27], can generate AO beam in which translational energy ranges from 2 to 13 eV and fluxes of ~10^{15} atoms/cm^2/s. They use a pulsed valve and a TEA CO_2 laser to generate a high-energy, intense AO beam. This laser detonation-type AO source can generate broad AO beam with both translational energies over 5 eV and fluxes over 10^{14} atoms/cm^2/s with exposure area of 1000 cm^2, and suitable for AO exposure tests of the engineering materials for space use.

From the view point of physical chemistry of the gas-surface collisions, a number of gas-surface interactions, such as Ar beam with Ge surface[28], AO/O_2 beam with Si surface[29], H beam with Cl adsorbed on Cu surface[30] etc, have been studied using supersonic beam sources. However, the translational energies of the beam species formed by these supersonic beam sources are less than a few eV (they are depending on the mass of the species, but velocity was limited by that of the light carrier gas in the beam). Therefore, the gas-surface reaction of the hyperthermal neutral atoms with surfaces at collision energies higher than a few eV range has not been investigated intensively, because of the lack of the beam source. The laser detonation-type beam source can accelerate the light weight atom such as AO more than 5 eV with maintaining a high flux. Thus, the laser detonation-type beam source opens the door to new experiments using high-energy, intense neutral beams.

In this study, the fast AO beam facility, which equipped a laser detonation-type AO source, time-of-flight beam characterizing system, and *in-situ* surface analysis systems, were developed. Even though the laser detonation-type AO source has been built in some space related organizations in Europe (ESTEC, ONERA) and some universities in U.S.A.

(Montana State Univ., Caltech), *in-situ* analysis capability of the target surface is original in this work. The reactions of hyperthermal AO beam with solid surfaces are focused in this study as well as correlating the flight data obtained by space shuttle flights.

Chapter 1 describes space environment near Earth. In this chapter, Earth's atmosphere, general aspects of LEO environment, environmental factors of material degradation are summarized. In addition, past flight experimental results and typical ground-based facilities for simulating AO in LEO are also mentioned.

In chapter 2, two AO beam facilities for *in-situ* AO analysis which have been developed in this study are described. These AO sources were based on the laser-breakdown phenomenon. One of the AO facilities used a Q-switched YAG laser and a current-loop-type pulsed supersonic valve (PSV). This AO facility was equipped with Auger electron spectroscopy (AES) and scanning tunneling microscopy (STM) for investigating the surface composition and morphological change without receiving any effect from ambient air. The other AO facility used a TEA CO_2 laser and a solenoid-type PSV, and included X-ray photoelectron spectroscopy (XPS) to investigate the chemical information of the AO-exposed surfaces without breaking the vacuum. The later system was same as the laser detonation-type AO source originally developed by Physical Sciences Inc. (PSI)[25-27]. The beam characterization of these AO sources were carried out using a time of flight (TOF) system and a quartz crystal microbalance (QCM) with silver electrodes. In addition to these two facilities, the laser detonation-type AO with a rotatable quadrupole mass spectrometer (QMS), which is located in Jet Propulsion Laboratory (JPL), was also used for investigating the TOF spectra of the reactive products from the surface. A brief description of the ion beam-type AO source formerly developed was also given in this chapter.

In chapter 3, the reaction dynamics of hyperthermal AO beam with highly oriented pyrolytic graphite (HOPG) was studied. Since HOPG (0001) is chemically stable and atomically flat, HOPG is one of the materials most commonly used in gas-surface reaction studies. On the other hand, AO reaction with graphite is important for predicting the survivability of the carbon-based materials (such as carbon fiber reinforce plastic (CFRP) or carbon fiber reinforce carbon (CFRC)) used in the LEO environment. The TOF distributions of the scattered AO and reaction products and the XPS and STM data were interpreted to build a reaction scheme of the hyperthermal AO beam with carbon surface.

In chapter 4, the interactions of hyperthermal AO beam with pyromellitic-

dianhydride (PMDA)-oxydianiline (ODA) polyimide polyimide films are described. Polyimide is widely used as a material for passive thermal control of the satellites, and, thus, directly exposed to the LEO space environment. Kapton-H (DuPont) is one of the most widely used PMDA-ODA polyimide in the aerospace applications. It has been widely known that Kapton-H film is eroded by hyperthermal AO bombardment in LEO, and is one of the reference materials to evaluate the other material's erosion rate. However, the reaction mechanism of Katpon-H with hyperthermal AO has not been established yet. In this chapter, not only Kapton-H, but also spin-coated polyimide film were used for analyzing the change in surface chemistry and its mass change during AO exposure. The mechanism of carbon abstraction from polyimide film caused by hyperthermal AO exposure are discussed based on the experimental data and the model calculation. Another point of interest on AO reaction with polyimide is the effect of air exposure before the analyses. All of the flight samples were suffered to being exposed to ambient air before the analyses. The surface chemical change due to the ambient air exposure on the eroded Kapton-H film was investigated by XPS in this thesis for the first time.

A potential of the laser detonation-type AO source to surface modification studies is demonstrated in chapter 5. This type of the source can deliver pulses of AO with translational energies in the range 2 ~ 15 eV and fluxes of about 10^{14} atoms/cm^2/s over the area of 1000 cm^2. Also the other kinds of atoms such as noble gases[31], halogen atoms[32], nitrogen atoms[32], CO_2 molecules[33] etc., can be accelerated by simply changing the precursor gas. These features are suitable as a surface modification or process technology. Capability of the broad AO beam oxidation of Si(001) at room temperature was demonstrated in this chapter. Silicon dioxide (SiO_2) has been widely used as an insulating layer for metal-oxide-semiconductor (MOS) devices. In general, SiO_2 layers are typically formed by high-temperature thermal oxidation processes in semiconductor industories. However, for the oxidation technology of the future ultra large-scale integration (ULSIs), it is necessary to develop a reliable low-temperature oxidation process. The 5 eV AO beam formed by the laser detonation-type source was applied for the oxidation of silicon. From the experimental results, the reaction mechanism of the hyperthermal beam oxidation as well as the advantage of beam technique for the low-temperature oxidation are shown.

Throughout the research described in this thesis, the importance of translational energy of AO beam to simulate the reaction (or degradation) in LEO is demonstrated. Since

not all of the space environmental effect (SEE) community members understand AO degradation mechanism of space materials importance, the contribution of this work to the SEE community will be remarkable. In order to achieve low risk mission in the growing human activities in LEO, SEE on the space materials would become more and more important in the next century, and this work is the first step of the systematic study in Japan.

References

1) Anderson, B. J. Ed.,"Natural orbital environment guidelines for use in aerospace vehicle development", NASA TM-4527, (1994).

2) L. J. Lenger, "Oxygen Atom Reaction with Shuttle Material at Orbital Altitudes -- Data and Experiment Status", AIAA-83-0073, (1983).

3) D. E. Hunton, "Shuttle Grow", Scientific American, November (1989), pp. 92.

4) D. G. Zimcik, C. R. Maag, "Results of Apparent Atomic Oxygen Reactions with Spacecraft Materials During Shuttle Flight STS-41G", Journal Spacecraft and Rockets, vol. 25 , (1988), pp. 162-168.

5) T. Ngo, E. J. Snyder, W. M. Tong, R. S Williams, M. S. Anderson, " O atom etching of graphite in low earth orbit", Surface Science, vol. 314 ,(1994), pp. L817-L822.

6) S. L. Koontz, L. J. Leger, J. T. Visentine, D. E. Hunton, J. B. Cross, C. L.Hakes, "EOIM-III mass spectrometry and polymer chemistry: STS-46", Journal Spacecraft and Rockets, vol. 32 , (1995), pp. 483-495.

7) D. E. Brinza, S. Y. Chung, T. K. Minton, R. H. Liang: Final report on the NASA/JPL evaluation of oxygen interactions with materials-3 (EOIM-3), JPL Publication 94-31, (1994).

8) T. K. Minton, T. A. Moore, 1994, "Molecular Beam Scattering from ^{13}C-Enriched Kapton and Correlation with the EOIM-3 Carousel Experiment", Proceeding 3rd LDEF Retrieval Meeting, Williamsburg AL, 1113-1117.

9) Whitaker, A. F. et al.: Orbital atomic oxygen effects on thermal control and optical materials -STS-8 results, AIAA paper 85-0416, (1985).

10) J. B. Whiteside, E. Kamykowski, W. D. Rooney, R. Schulte, M. Stauber, " Effects of 69 Months in Low Earth Orbit on Kapton Antenna Structures", Journal Spacecraft and Rockets, vol. 31, (1994), pp. 860-865.

11) M. Tagawa, M. Matsushita, M. Umeno, N. Ohmae, "Laboratory Studies of Atomic Oxygen Reactions on Spin-Coated Polyimide Films", Proceeding 6th International Symposium on Material in a Space Environment, Noordwijk, The Netherlands, SP-368, (1994), pp. 189-194.

12) J. B. Cross, D. A. Cremers, "Atomic oxygen surface interactions -mechanistic study using ground-based facilities", AIAA Paper No. 85-0473, (1985).

13) A. K. Stark, L. A. Berglund, M. Tagawa, N. Ohmae, "Effect of Atomic Oxygen on the mechanical Properties of Highly Graphitzed Carbon Fibers", Carbon, vol. 32, (1994), pp. 641-644.

14) M. Tagawa, M. Tomita, M. Umeno, and N. Ohmae, "Atomic Oxygen Generators for Surface Studies in Low Earth Orbit", AIAA Journal, vol 32, (1994), pp. 95-100.

15) Orient, O. J. et al., "Recombination of 5-eV O(3P) atoms with surface-adsorbed NO: spectra and their dependence on surface material and temperature", Physical Review A, vol. 45, (1992), pp. 2998-3003.

16) M. A. Golub, T. Wyderen, "Reaction of atomic oxygen (O(3P)) with various polymer films", Polymer Degradation and Stability, vol. 22, (1988), pp. 325-338.

17) M. A. Golub et al.," ESCA study of Kapton exposed to atomic oxygen in low earth orbit or downstream from a radio-frequency oxygen plasma", Polymer Communications, vol. 29, (1988), pp. 285-288.

18) S. L. Koontz et al."Atomic oxygen testing with thermal atom systems: a critical evaluation", Journal of Spacecraft and Rockets, vol. 28, (1991), pp. 315-323.

19) S. L. Koontz, L. Leger, K. Albyn, J. B. Cross, "Vacuum ultraviolet radiation/atomic oxygen synergism in materials reactivity", Journal of Spacecrafts and Rockets, vol. 27, (1990) pp. 346-348.

20) E. Grossman, Y. Noter, Y. Lifshits, "Oxygen and VUV irradiation of polymers: atomic force microscopy (AFM) and complimentary studies", Proceeding. 7th Int. Symp. Materials in Space Environment, Toulouse, France, ESA SP-399, (1997), pp. 217-223.

21) B. A. Banks et al., "Simulation of the low earth orbital atomic oxygen interaction with materials by means of an oxygen ion beam", NASA TM-101971 (1989).

22) Z. A. Iskanderova, J. I.Kleiman, Y. I. Gudimienko, R. C. Tennyson, "Influence of content and structure of hydrocarbon polymers on erosion by atomic oxygen", Journal of Spacecraft and Rockets, vol. 32, (1995) pp. 878-884.

23) M. Tagawa, M. Tomita, N. Ohmae, M. Umeno, "Atomic oxygen generators for surface studies in low earth orbit", AIAA Journal, vol. 32, (1994), pp. 95-100.

24) G. S. Arnold, D. R. Peplinski, "Reaction of High-Velocity Atomic Oxygen with Carbon", AIAA Journal, vol. 24 (1986) pp. 673-677.

25) G. E. Caledonia, R. H. Krech, "Energetic Oxygen Atom Material Degradation Studies", AIAA paper 87-0105, 1987.

26) G. E. Caledonia, R. H. Krech, B. D. Green, "A High Flux Source of Energetic Oxygen Atoms for Material Degradation Studies", AIAA Journal, vol. 25, (1987), pp.59-63.

27) B. Cazaubon, A. Paillous, J. Siffre, R. Thomas, "Five-Electron-Volt Atomic Oxygen Pulsed-Beam Characterization by Quadrupolar Mass Spectrometry", Journal of Spacecraft and Rockets, vol. 33, (1996) pp. 870-876.

28) A. Amirav, M. J. Cardillo, P. L. Trevor, C. Lim, J. C. Tully, "Atom-surface scattering dynamics at hyperthermal energies", Journal of Chemical Physics, vol. 83 (1987) pp. 1796-1807.

29) J. R. Engstrom, T. Engel, "Atomic versus molecular reactivity at the gas-solid interface: The adsorption and reaction of atomic oxygen on the Si(100) surface", Physical Review B, vol. 41 (1990) pp. 1038-1041.

30) C. T. Rettner, D. J. Auerbach, "Distinguishing the Direct and Indirect Products of a Gas-Surface Reaction", Science, vol. 263 (1994) pp. 365-367.

31) T. K. Minton, J. W. Seale, D. J. Garton, A. K. Frandsen, "Dynamics of Atomic-Oxygen-Induced Degradation of Materials", Proceeding of Protection of Materials and Structures from the LEO Space Environment, Toronto, Canada, April (1998), paper no. A2.

32) P. G. Konstantions, T.A. Moore, T. K. Minton, "Hyperthermal neutral beam etching," J. Vac. Sci. Technol. A, vol. 13, (1995), pp. 959-965.

33) T. K. Minton, J. W. Seale, D. J. Garton, J. Zhang, "Mechanism of polymer erosion in low Earth orbit: Implication for ground-based atomic oxygen testing", Proceeding of 44th International SAMPE symposium and Exhibition, Long Beach, CA, May (1999), pp. 1051-1063.

34) T. K. Minton, M. Tagawa, G. M. Nathanson, "Energy accommodation in gas-surface collision: relevance to Mars aerobraking", 8th International symposium on Materials in a Space Environment, Arcachon, France, Jane (2000), submitted.

Chapter 1

Space environment near the earth

1. 1 Earth's atmosphere

The earth's atmosphere has many regions which have different characteristics[1]. In general, the earth's atmosphere is divided into the troposphere, the stratosphere, the mesosphere, the thermosphere, and the exosphere (see Figure 1.1).

1) The troposphere starts at the earth's surface and extends to an altitude of 10 km. Almost all clouds and weather occur in the troposphere. It contains about 99 % of the atmosphere's water vapor and 90 % of the air.

2) The stratosphere extends from the tropopause to an altitude of 48 ~ 53 km. The temperature of the stratosphere increases slightly with altitude which results in vertical stability. Air flow in the stratosphere is mostly horizontal. Ozone, an isotope of

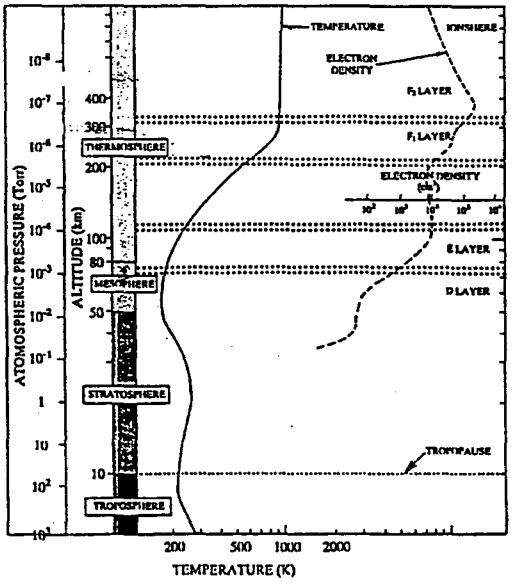

Figure 1.1 Atmosphere regions of the Earth[1].

oxygen, is present in the ozone layer which varies in altitude from 20 to 35 km above the earth.

3) The mesosphere extends from the stratopause at the lower boundary to an altitude of about 80 km. Above about the altitude of 48 km there are not enough atmospheres for even a high altitude ramjet to operate. Above this altitude both fuel and oxidizer must be carried for a rocket engine to provide thrust.

4) The thermosphere extends from an altitude of 80 km to 320 km ~ 600 km. At an altitude above 100 km wings and other lift and control surfaces no longer work since the atmosphere is too thin to generate lift and aerodynamic stabilization. The thermal temperature of the constituents varies approximately exponentially from - 100 K at 100 km to 500 ~ 1500 K at 1000 km, depending on solar cycle, altitude, and local time, with excursions to 2000 K during high levels of geomagnetic activity. An altitude of 150 km is the lowest altitude at which a satellite in a circular orbit can orbit the earth for at least one revolution without propulsion. At this altitude it takes 87.5 minutes to complete one revolution of the earth. This altitude is the most commonly accepted definition of where space begins but it is not explicitly stated in any treaty or international agreement. An altitude of 130 km is about the lowest altitude (perigee) at which a satellite in an elliptical orbit can pass through the earth's atmosphere and still remain in orbit. Space shuttle and International Space Station (ISS) can fly only in these orbits and these orbits are called low Earth orbit (LEO).

5) The exosphere begins where the thermosphere ends and extends out into space. In this region the density of atoms and molecules of the atmospheric gases is quite low. Typically, individual atoms travel about 250 km in 20 minutes before colliding with another atom. Stationary satellite is flying in an altitude of 36000 km with the same speed of the earth's rotation, thereby keeping the satellite stationary over a particular spot on the earth. Its orbit is called geosynchronous Earth orbit (GEO).

1.2 LEO environment

1.2.1 Residual atmosphere

The variations of the neutral atmosphere at orbital altitudes between about 100 and 1000 km are plotted in Figure 1.2[1]. This is the region in which material degradation has been observed. The dominant species in this region is AO. He, NO, N, and Ar are also present below the 1 % level. As spacecraft between 100 and 1000 km are moving at about 8 km/s, the resulting impact energy of the particles can reach values on the forward (or ram) surface of the spacecraft well in excess of 5 eV (varying from 4.6 eV for N to 10.25 for O_2).

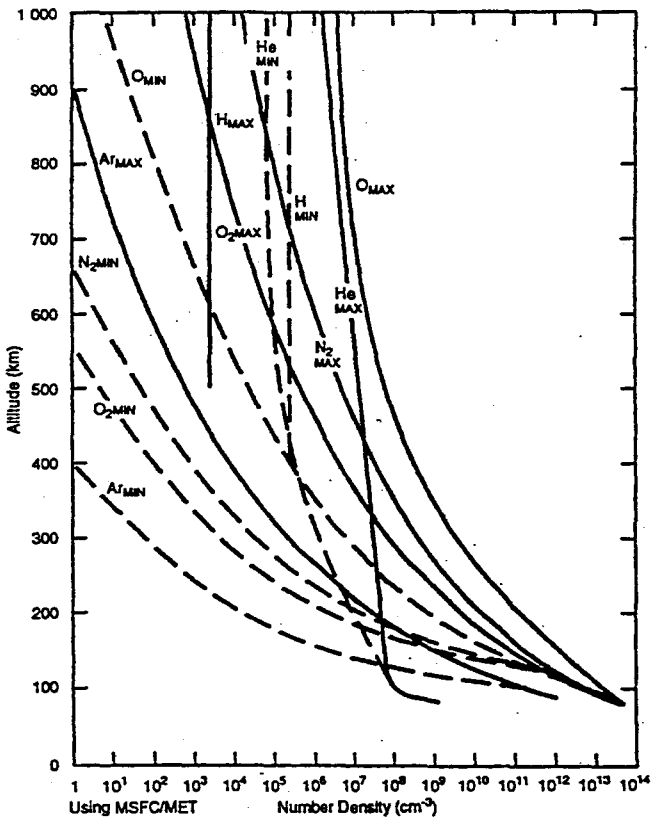

Figure 1.2 Residual neutral atmosphere profiles for average geophysical condition[1].

1.2.2 Atomic oxygen

The dominant species in the LEO environment is AO (ground state neutral), which is produced by dissociation of O_2 by the vacuum UV (VUV, 100~200 nm),

$$O_2+h\nu\ (VUV) \Rightarrow 2O \qquad (1).$$

Whereas two AO react each other only when the catalysis species exist,

$$O+O+M(\text{catalysis species}) \Rightarrow O_2+M \qquad (2).$$

Since velocity of reaction (2) decreases with decreasing the density of the atmosphere, the density of AO increases with increasing the altitude. In addition, since specific gravity of AO is lighter than those of O_2 and N_2, AO goes to upper the earth's atmosphere due to atmosphere diffusion. So that AO becomes the dominant species in the LEO environment.

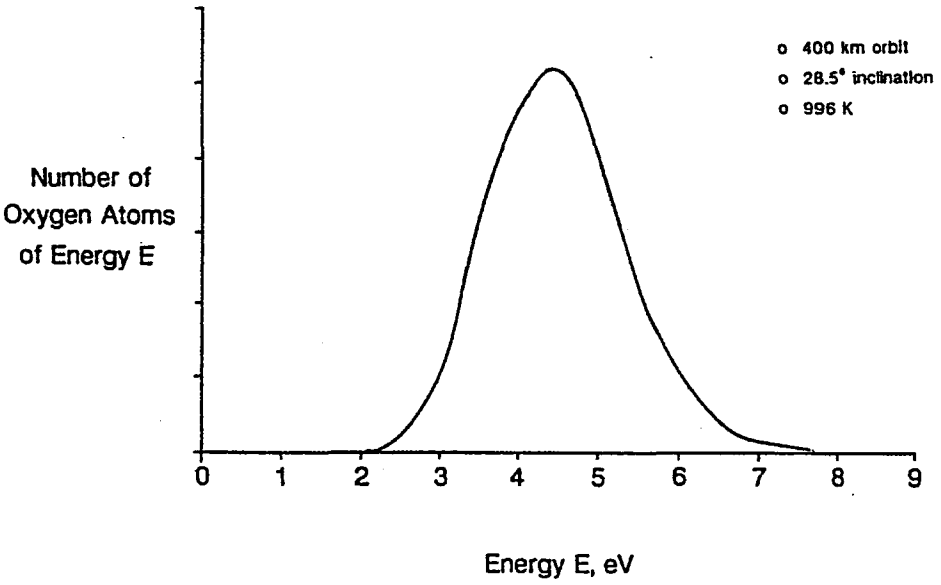

Figure 1.3 Typical AO translational energy distribution in the LEO environment[2].

AO concentration in the LEO environment is 10^6~10^9 atoms/cm^3, which depends on the altitude. However, since the orbital velocity of spacecraft is nearly 8 km/s, the actual flux of AO impinging on an orbiting spacecraft is quite high (~10^{15} atoms/cm^2). The spacecraft orbital velocity of 8 km/s corresponds to a mean AO energy of ~4.8 eV. The ambient temperature in LEO is of th e order of 1000 K, and the FWHM of the AO translational distribution is over 2 eV. Figure 1.3 shows the typical AO translational energy distribution in the LEO environment[2]. Spacecraft surfaces facing the orbital direction (ram surface) experience both very high relative interaction energies and high fluxes with AO and other ambient particles, while trailing surfaces experience essentially no collisions with these particles. The material degradations in the LEO environment are mainly observed in the surfaces facing the orbital direction. Considering this "ram effect", hyperthermal AO collision is considered to be one of the most critical factors that influence the material degradation in the LEO environment.

1.2.3 Hyperthermal AO interaction with solid surfaces

Important phenomena on material surfaces due to hyperthermal AO observed in the LEO environment are shown in Figure 1.4. Material degradation is divided into two types, volatile reaction (1) and oxidation (2). The volatile reaction leads to mass loss of materials and is observed in mainly carbon-based materials and organic polymers. The eroded surfaces of there materials are also oxidized (2). Silver shows only the oxidation reaction because of the non-volatile nature of its oxide. Many of metals and semiconductor materials surface are oxidized by AO reaction, and details of there volatile and non-volatile oxidize formation are described with later chapters in this thesis. The another important phenomenon observed in the LEO environment is glow (3), which is called "space shuttle glow". This grow is emitted from the reaction of hyperthermal AO with NO, which may adsorb on the spacecraft surface. Both material degradations and glow are serious problems for the design of spacecraft.

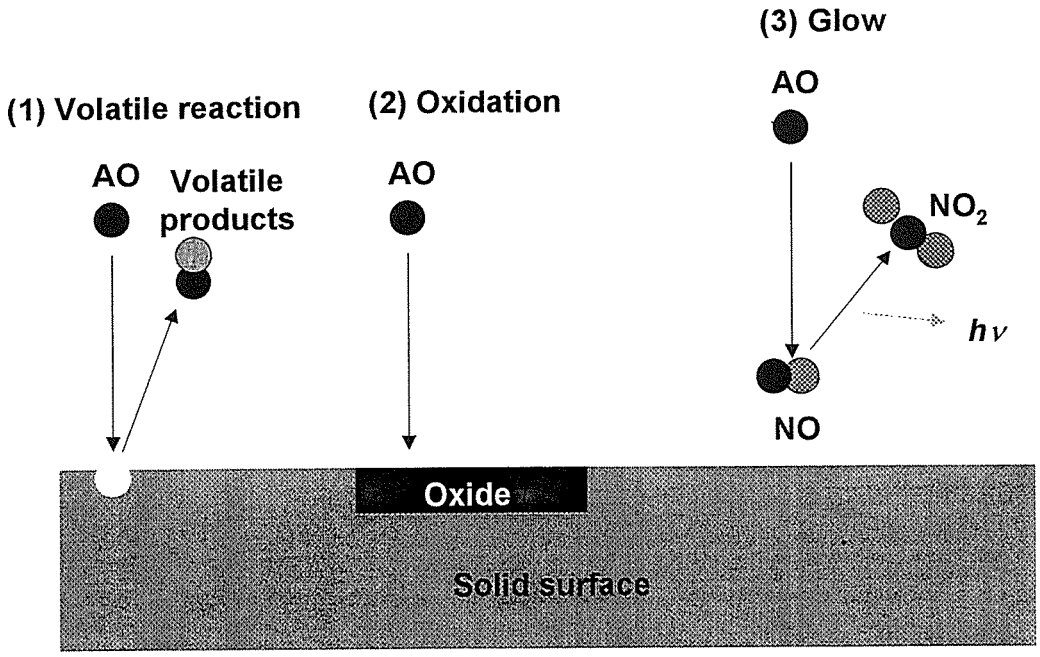

Figure 1.4 The irradiance of the Solar spectra in space environment.

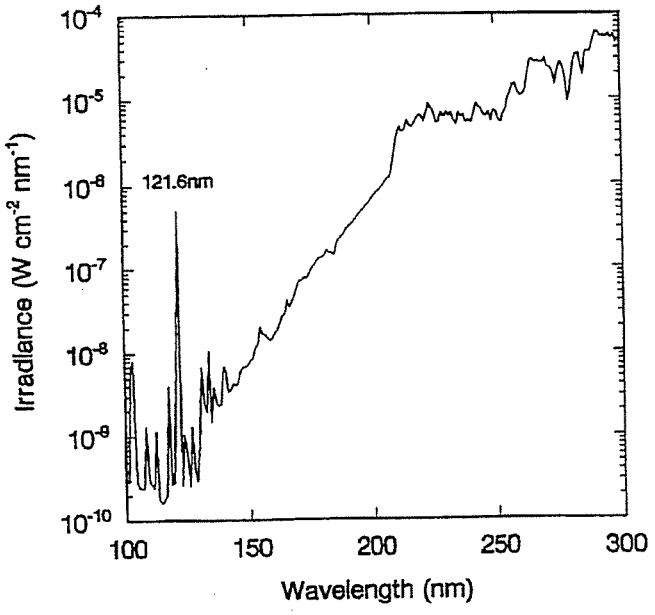

Figure 1.5 Phenomena on material surfaces due to hyperthermal AO observed in the LEO environment[3].

1.2.4 Other degradation factors in LEO

In addition to hyperthermal AO, there are many environmental factors of material degradations in space such as ultraviolet (UV) and vacuum UV (VUV), plasma environment (ions and electrons), radiation, meteoroids and space debris, and so on. Furthermore, the presence of synergetic effects of hyperthermal AO bombardment and these environmental factors should be considered.

1) Ultraviolet and vacuum ultraviolet radiation

UV/VUV radiation has been found to contribute significantly to the material degradation in Earth orbital spacecraft. UV/VUV radiation is occurring at all Earth orbits. The solar spectral irradiance in space environment is shown in Figure 1.5[3]. In the region of highest energy, 100~150 nm, the major component (~80 %) of the irradiance is due the Lyman-alpha line of atomic hydrogen occurring at 121.6 nm. At wavelengths higher than 150 nm the flux increases dramatically with by far the greatest flux occurring in the 200 to 300 nm region. Many organic polymers absorb this spectral region between 100 ~ 300 nm and show degradations. In addition, it has been reported the presence of synergetic effect of AO and UV/VUV radiation in some materials[4,5].

2) Plasma environment

Ionized gases are encountered around the earth. They cause a multitude of problems, the most serious of which is the electrostatic charging of satellite surfaces when energetic plasma is injected near the busy geostationary orbit e.g. during magnetospheric storms and substorms. Discharges can severely disturb operations and even result in the loss of satellites.

3) Radiation

The earth has a radiation. It is populated by protons of energies in the 10 ~ 100 MeV range, which readily penetrate spacecraft. High dose of radiation damages materials and instruments, induces single event (computer error) and is a hazard to astronauts.

4) Meteoroids and Space Debris

Meteoroids and space debris are directed to spacecraft surface with quite high velocities (over 4 km/s). Meteoroids and space debris can seriously damage satellites (see Figure 1.6)[6]. Increasing space activities add to the debris problem in popular orbits while the meteoroid environment is an ever-present though sporadic feature.

1.3 GEO environment

The satellite at GEO is flying with the same speed of the earth's rotation, thereby keeping the satellite stationary over a particular spot on the earth. However, the GEO environment is out of the earth's atmosphere. The degree of vacuum of the LEO environment is 10^{-4}~10^{-6} Pa, whereas that of the GEO environment is below 10^{-10} Pa. The dominant species in the GEO environment is hydrogen atom, which do not affect on materials. Therefore, neutral species interaction with material surface is no problem in the GEO environment. The problems of spacecraft's mission in the GEO environment are unexplained operation of electronic circuits and degradation of thermal control components due to the charging by electrons, radiation, and UV/VUV radiation.

1.4 Material degradations due to AO exposure in LEO

1.4.1 Beginning of the problem

The orbiter of the space transport system (STS), generally called space shuttle, has a cargo-bay in which the interior surface can be directed to ram direction by opening the bay. Furthermore, the interior surface of the cargo-bay is not affected by the heat in reentry phase. Engineers examining the shuttle after its early flights observed significant changes in the condition of many of the materials in the cargo-bay. After spaceflight, some samples were dull, light yellow and opaque[7]. Kapton-H, a polyimide film used extensively for thermal insulation, is generally translucent, glossy and deep amber in color. The carbon coating on two metal spheres that served as sensors for electric-field measurements had been eroded away completely. Silver films were badly oxidized. Thermal-control paints had lost their

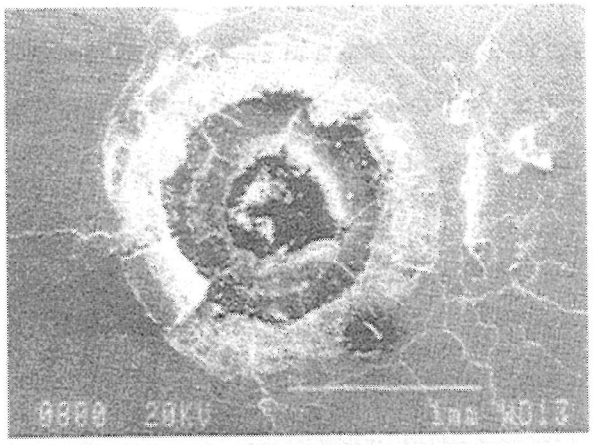

Figure 1.6 Typical debri impact hole in the Hubble space telescope solar arrays[6].

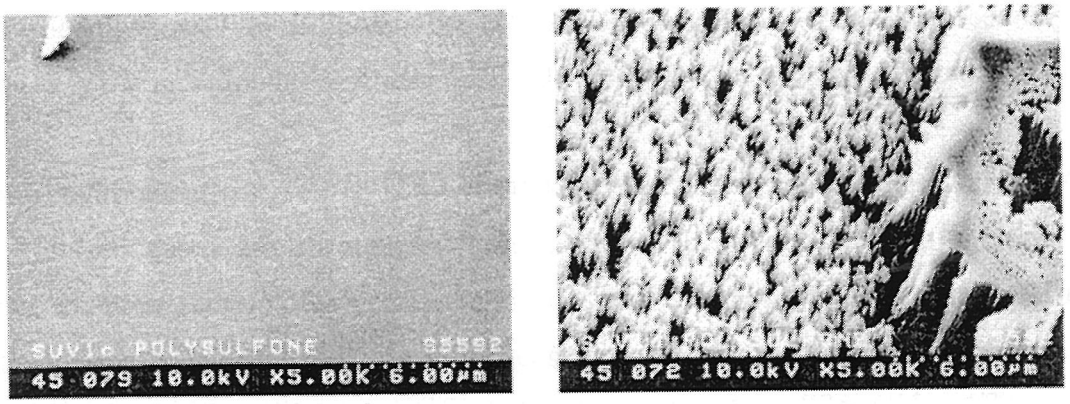

Figure 1.7 The SEM photograph of polysulfone film before (a) and after exposure of the LEO environment (b). The total ram exposure time at 230 km was 42.25 hours in STS-46 mission[18].

gloss. When the erosion of shuttle surfaces was first discovered, a group of NASA engineers and scientists led by Lubert J. Leger proposed that the phenomenon was caused by reactive AO[6]. After these observations, material exposure experiments in LEO were started using space shuttle to investigate interactions of material surfaces with AO in the LEO environment. In addition, simulators for the AO environment have been developed for carrying out ground-based experiments, because the large number of materials/flight conditions have to be studied and flight scheduling is limited.

1.4.2 Flight experiments

Flight experiments have yielded the quantitative data available on the effects of the orbital environment on surfaces and materials. The flight experiments were conducted during space shuttle flights STS-2[8], STS-3[8], STS-4[8,9], STS-5[10], STS-8[11], STS-17[11], STS-32[12], STS-41G[13], STS-44[14], STS-46[15] and so on. Long Duration Exposure Facility (LDEF)[16] and Space Flyer Unit (SFU) material exposure experiments were conducted using satellites, which is deployed in LEO and retrieved by shuttles. In parallel with these experiments, Russian Space Agency (RSA) and European Space Agency (ESA) has carried out flight experiments using "Mir" space station. In these flight experiments, LDEF[17] provide most of the materials degradation data.

After the flight, the sample were basically returned to the laboratory, where they were weighed to determine how much mass they had lost and then photographed at high magnification under a scanning electron microscope (SEM) (see Figure 1.7)[18]. The profiles of the samples were measured with high accuracy to determine how thick a layer had been etched away, and composition of each sample was determined in search of possible chemical changes.

1.4.3 Ground experimental facilities

In ground-based facilities it is quite difficult both to produce a relative translational energy of 5 eV and to exceed the flux of over 10^{12} atoms/cm^2/s, which correspond to AO

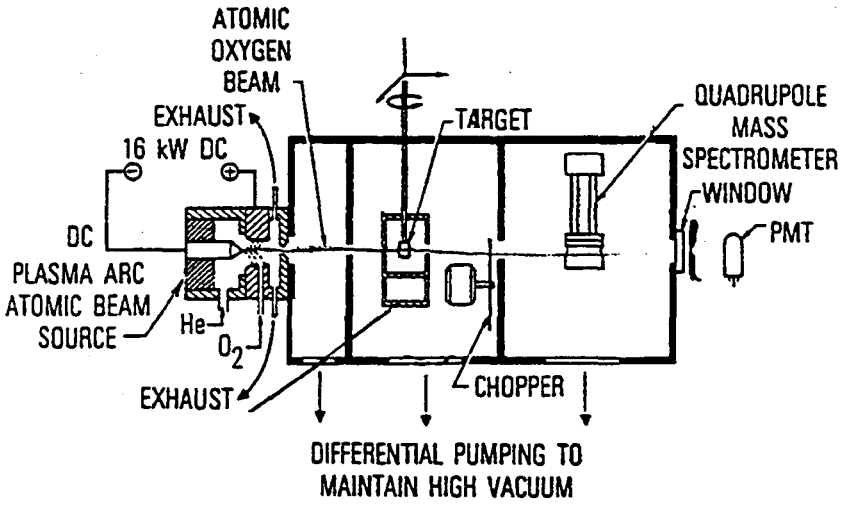

Figure 1.8 The supersonic beam-type AO source developed by G. S. Arnold et al.[19].

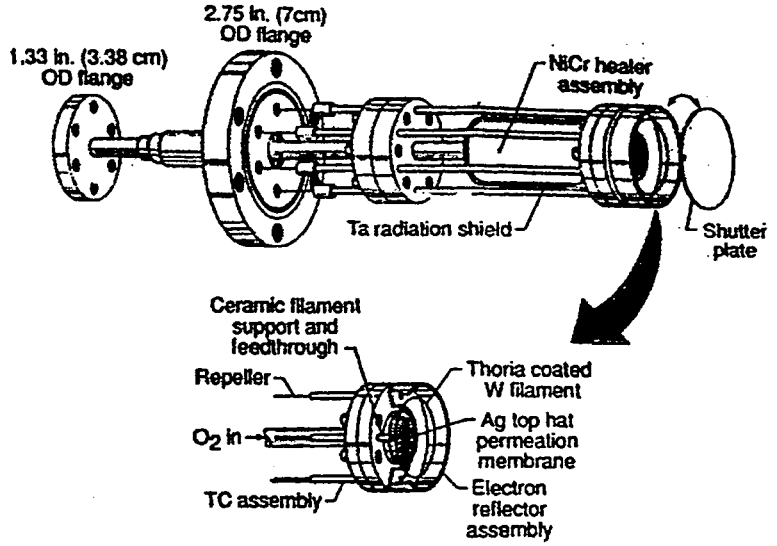

Figure 1.9 The ESD-type AO source developed by R. A. Outlaw et al.[20].

environment in LEO, at the same time. Conventional plasma asher facilities or radio-frequency (RF) microwave plasma systems have been used for investigation of the AO reaction. However, the translational energy of AO provided by these experimental facilities is close to thermal region. It is widely recognized that the reaction mechanism of hyperthermal AO with solid surface is quite different from that of thermal AO. For example, the needle-like surface is observed at the polysulfone surface exposed to hyperthermal AO (see Figure 1.7), however, exposed to thermal AO, generated by conventional plasma others, does not show such a feature. Therefore, it is necessary to use hyperthermal AO beam when evaluating the material degradation in the LEO environment.

An ion beam-type AO source can accelerate AO to 5 eV, however, its flux is low typically below 10^{12} atoms/cm^2/s. G. S. Arnold et al. have developed the hyperthermal AO source using supersonic beam technique[19]. The schematic of this source is shown in Figure 1.8. A plasma is formed in helium by a DC ark. A small amount of O_2 (typically ~2 % of total gas flow) is injected downstream of the arc into the gas flow, where it is thermally dissociated into oxygen atoms by the hot helium. Typical AO flux generated by this AO source is on the order of 10^{15} ~ 10^{16} atoms/cm^2/s. However, the beam velocity is 3.5 km/s

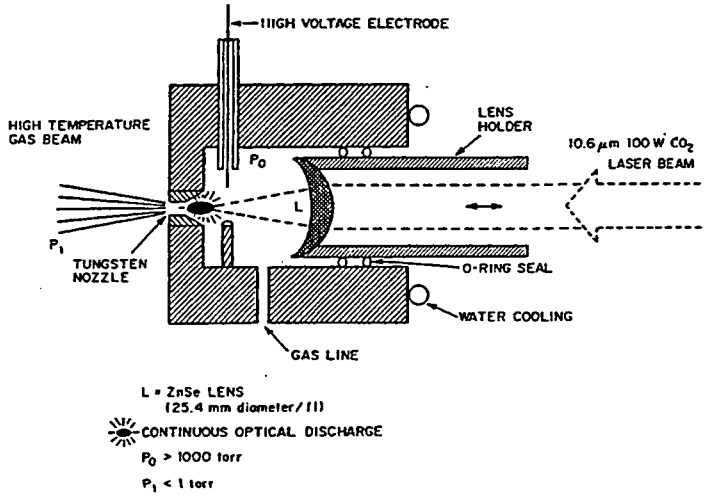

Figure 1.10 The optical discharge-type AO source developed by J. B. Cross et al.[21].

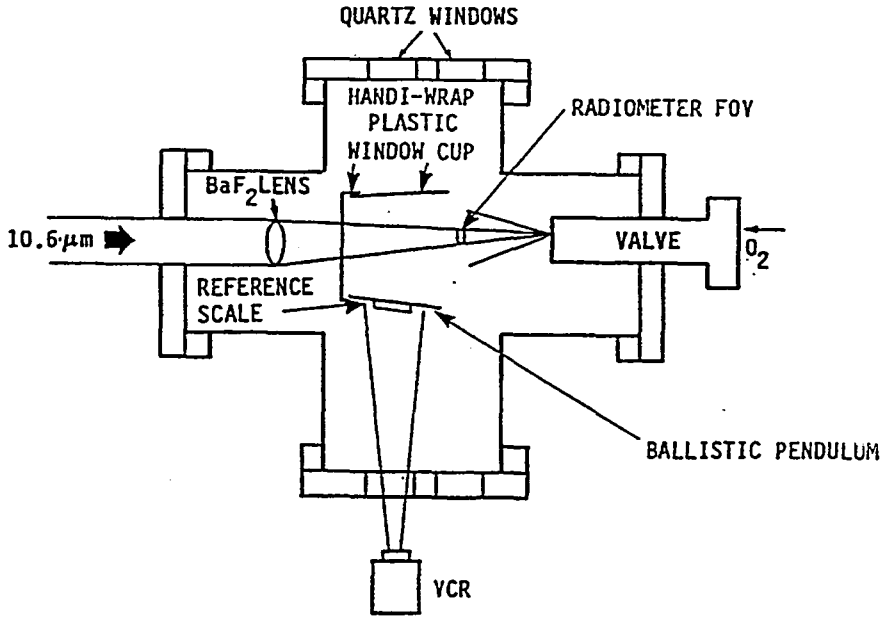

Figure 1.11 The laser detonation-type AO source developed by G. B. Caledonia et al.[22].

which corresponds to an AO translational energy of 1.7 eV. R. A. Outlaw et al. have developed the hyperthermal AO source using electron-stimulated desorption (ESD) phenomenon[20]. Figure 1.9 represents the schematic of the source. The instrument combines the mechanisms of O_2 dissociation and transport through a hot Ag membrane to provide a continuous source of O atoms to a vacuum interface where they are subsequently emitted into the vacuum space by ESD. A translational energy of AO generated by this AO source is ~5 eV, and the flux of AO is 4.5×10^{13} atoms/cm^2/s. This AO source is reported to be suitable to the requirement of the simulator for the AO environment by the constructure. However, actual potential of this source is unclear. J. B. Cross et al. have developed the hyperthermal AO source using optical discharge phenomenon[21]. The schematic of the source is shown in Figure 1.10. A high temperature plasma (<30,000 K) is produced in the throat of a hydordynamic expansion nozzle by sustaining a cw optical discharge in a gas using a high power cw CO_2 laser. Gas mixtures are expanded through the nozzle/discharge region creating energetic atoms and molecules. An oxygen atoms beam generated by this AO

source has been produced with a flux of 10^{18} atoms/cm^2/s, however, the translational energy is as low as 2 ~ 3 eV.

The laser detonation-type AO source, which is pioneered by Caledonia et al.[22], is shown in Figure 1.11. They use a pulsed valve and pulsed CO_2 laser to generate of high-energy intense AO beam. In the concept of the laser-detonation method, an incoming laser beam is focused into molecular oxygen ejected by the pulsed valve in the throat of a nozzle. The resulting high-pressure plasma is formed and detonation wave is initiated by a high-power laser-induced breakdown of oxygen. With a short duration laser pulse, the detonation wave quickly becomes a blast laser wave, which propagates to the nozzle exit plane, converting all of the high pressure of the gas behind it into a propelling force. The high energy of the laser-produced plasma is converted effectively to velocity of the exhaust gases. The laser detonation-type AO source can generate AO which translational energy ranges from 2 to 13 eV and fluxes of ~10^{15} atoms/cm^2/s, these are enough to the requirements for the AO environment simulator.

References

1) B. J. Anderson, Ed.: Natural orbital environment guidelines for use in aerospace vehicle development, NASA TM-4527 (1994).

2) B. A. Banks, "Atomic Oxygen", LDEF Materials Data Analysis Workshop, NASA CP 10046, July (1990).

3) Space Simulation, NASA-298, "Proposed Specification for the Solar Constant and Air Mass Zero Solar Spectral Irradiance", Paper No. 82, (1972), pp. 955-968.

4) M. Tagawa, T. Suetomi, H. Kinoshita, M. Umeno, N. Ohmae, "Surface Reaction of a Low Flux Atomic Oxygen Beam with a Spin-Coated Polyimide Film: Synergetic Effect of Atomic Oxygen and Ultraviolet Exposure", Transactions of the Japan Society for Aeronautical and Space Sciences, vol. 42, (1999), pp. 40-45.

5) J. I. Kleiman et al., "Surface Structure and Properties of Polymers Irradiated with Hyperthermal Atomic Oxygen", Surface and Interface Analysis, vol. 23, (1995), pp. 335-341.

6) M. Rival, J. C. Mandevill, "Hypervelocity Impact on Solar Arrays: Analysis of Secondary Particles Ejection and Implications for Environment", Proceeding. 7th Int. Symp. Materials in Space Environment, Toulouse, France, ESA SP-399, (1997), pp. 469-475.

7) D. E. Hunton, "Shuttle Glow", Scientific America, November (1989), pp. 92-98.

8) L. J. Lenger, "Oxygen Atom Reaction with Shuttle Material at Orbital Altitudes -- Data and Experiment Status", AIAA-83-0073, (1983).

9) P. N. Peters, R. C. Linton, E. R. Miller, "Resuls of Apparent Atomic Oxygen Reactions on Ag, C, and Os

Exposed during the Shuttle STS-4 Orbits", Geophysical Research Letters, vol. 10, (1983), pp. 569-571.
10) W. S. Slemp, AIAA Paper 83-2633, (1983)
11) J. T. Visentine (compiler), NASA-TM-100459, vols. 1 & 2, (1988)
12) R. C. Tennyson, W. D. Morision, J. E. Klemberg, L. Martinu, M. U. Wertheimer, D. G. Zimick, AIAA Paper 92-2152, (1992).
13) D. G. Zimcik, C. R. Maag, " Result of Apparent Atomic Oxygen Reaction wit Space Materials During Shuttle Flight STS-41G", Journal Spacecraft and Rockets, vol. 25 , (1988), pp. 162-168.
14) A. Dunnet, T. D. Kirkendal, Proccedings of the European Space Power Conference, ESA-SP 320 (1991).
15) R. A. Synowicki, J. S. Hale, Blaine Spady, M. Reiser, S. Nafis, J. A. Woollam, "Thin Film Matrials Exposure to Low Earth Orbit Aboard Space Shuttle", Journal Spacecraft and Rockets, vol. 32, (1995), pp. 97-102.
16) J. B. Whiteside, E. Kamykowski, W. D. Rooney, R. Schulte, M. Stauber, " Effects of 69 Months in Low Earth Orbit on Kapton Antenna Structures", Journal Spacecraft and Rockets, vol. 31, (1994), pp. 860-865.
17) The LDEF Archive System is designed to provide spacecraft designers and space environment researchers a single point access to all available resources from LDEF. LDEF had a nearly cylindrical structure, and its 57 experiments were mounted in 86 trays about its periphery and on the two ends. LDEF remained in space for ~5.7 years and completed 32,422 Earth orbits; this extended stay increased its scientific and technological value toward the understanding of the space environment and its effects.
18) D. E. Brinza, S. Y. Chung, T. K. Minton, R. H. Liang: Final report on the NASA/JPL evaluation of oxygen interactions with materials-3 (EOIM-3), JPL Publication 94-31, (1994).
19) G. S. Arnold, D. R. Peplinski, " Reaction of High-Velocity Atomic Oxygen with Carbon", AIAA Journal, vol. 24 (1986) pp. 673-677.
20) R. A. Outlaw, M. R. Davidson, "Small Ultrahigh Vacuum Compatible Hyperthermal Oxygen Atoms Generator", Journal of Vacuum Science Technology A12, (1994), pp. 854-860.
21) J. B. Cross, D. A. Cremers, "Atomic Oxygen Surface Interaction-Mechanistic Study Using Ground Based Facilities", AIAA-85-0473, (1985).
22) G. E. Caledonia, R. H. Krech, B. D. Green, "A High Flux Source of Energetic Oxygen Atoms for Material Degradation Studies," AIAA Journal, vol. 25, (1987), pp.59-63.

Chapter 2
Experimental facilities

Abstract

Two AO beam facilities for *in-situ* AO analysis are described. These AO sources were based on the laser-breakdown phenomenon. One of the AO facilities used a Q-switched YAG laser and a current-loop-type PSV. This AO facility equipped with STM and AES, and the other AO facility used a TEA CO_2 laser and a solenoid-type PSV, and equipped with XPS. The later system was the laser detonation-type AO source originally developed PSI. The beam characterization of these AO sources were carried out using a TOF system and a QCM with silver electrodes. The former system generated AO beam with the mean translational energy of 4.7 eV and the flux of 4.0×10^{12} atoms/cm^2/s at a sample position of 32 cm away from a breakdown point. The later system can deliver a hyperthermal AO beam with translational energy of approximately 5 eV and flux over 3×10^{14} atoms/cm^2/s at a sample position of 47 cm away from a nozzle throat. The CO_2 laser-type hyperthermal AO source contains hyperthermal O_2 component as well as hyperthermal AO component, whereas the former system didn't contain hyperthermal O_2 component. In addition to these facilities, the laser detonation-type AO with a rotatable QMS, which is located in JPL, and the ion beam-type AO source formerly developed were also briefly described in this chapter.

2.1 The AO beam facility using a Q-switched YAG Laser

2.1.1 General layout

Figure 2.1 shows the configuration of the fast AO beam facility with the Q-switched YAG laser. This system consisted of four vacuum chambers; (a) AO source chamber, (b) TOF chamber, (c) AES chamber, and (d) preparation chamber. These chambers were evacuated by a 700 l/s oil diffusion pump (DP), a 300 l/s turbo molecular pump (TMP), a 300

l/s sputter ion pump (IP), and a 150 l/s TMP, respectively. The vacuum pressure of each chamber was 10^{-6}, 10^{-6},10^{-8}, and 10^{-5} Pa, respectively. The AO source and the TOF chambers were differentially pumped through an orifice with a square hole of 4 mm^2, and the AO beam along the beam axis was only allowed to enter the ionizer of QMS in the TOF chamber. The pressure of the TOF chamber was kept in 10^{-5} Pa even when the vacuum of AO source chamber falls instantly to 10^{-3} Pa at the moment of the introduction of oxygen gas for fast AO beam formation. The other chambers were connected each other with UHV-gate valves. The transfer rods installed in the facility were used to transfer the sample between the AO source chamber and the AES chamber without breaking vacuum.

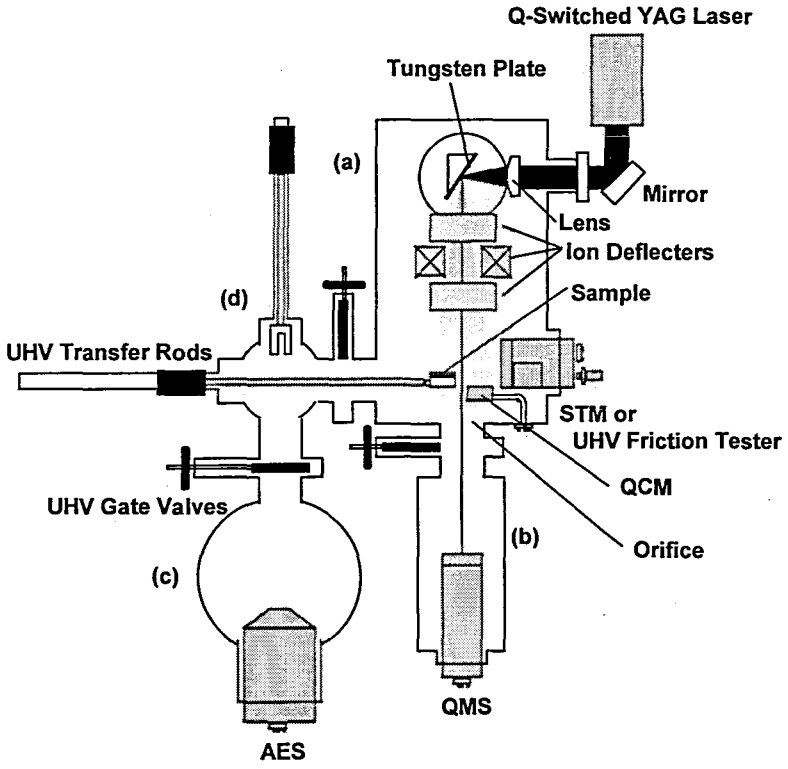

Figure 2.1 A schematic drawing of the AO facility using a Q-switched YAG laser (plane view). This system consisted of four UHV-chambers, connected each other with UHV-gate valves. (a) AO source chamber, (b) TOF chamber, (c) AES chamber, and (d) preparation chamber. UHV-STM and UHV-friction tester were equipped in the AO source chamber.

2.1.2 Hyperthermal AO beam source

A detail of the AO source developed in this study is shown in Figure 2.2. A 99.95 % pure oxygen gas was introduced parallel to the tungsten surface through the orifice (1.0 mm in diame ter) of the PSV. The PSV was a current loop-type PSV which provides faster operation (60 μs) than solenoid-type valves. The plenum pressure of the PSV was kept at $6 \times 10^5 \sim 1 \times 10^6$ Pa. A Q-switched YAG laser (200 mJ/pulse) was used to decompose oxygen gas to AO. The laser beam was aligned by two infrared mirrors, and focused at the nozzle of the PSV with a quartz lens (80 mm in focal length). This lens was mounted on a manipulator so that the focal point of the laser was adjustable from the outside of vacuum.

The laser was introduced perpendicular both to PSV and to AO beam axes. This configuration reduced the sample from being exposed to undecomposed thermal O_2. Laser irradiation caused the emission of seed electrons from the tungsten plate located close to the

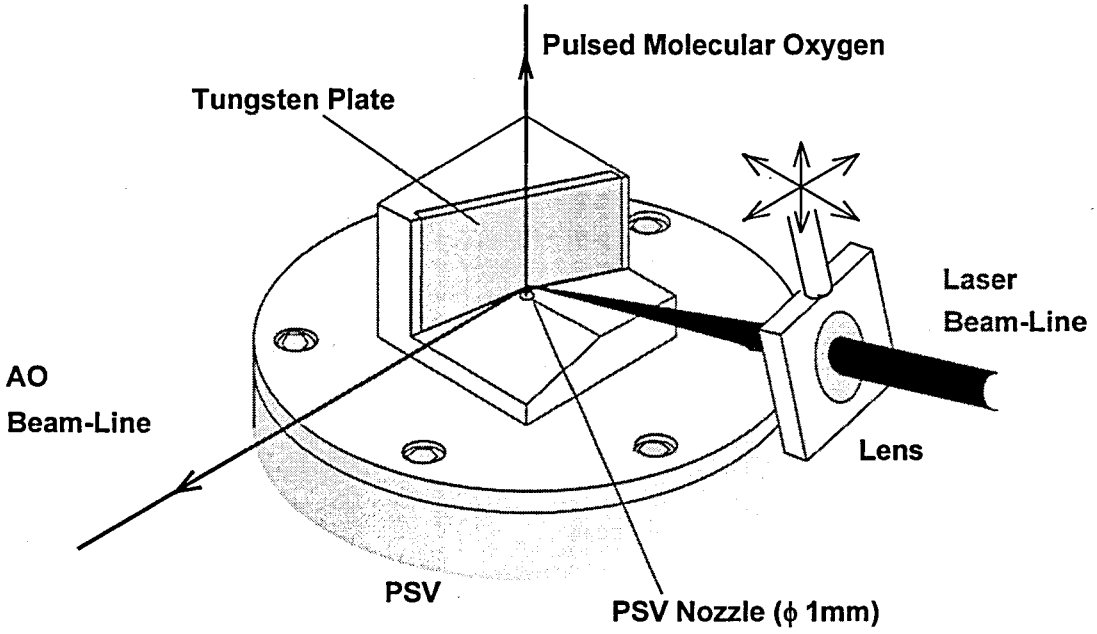

Figure 2.2 Details of the laser detonation-type AO beam source using a Q-switched YAG laser. Oxygen gas was introduced from the nozzle of PSV, and the AO beam was created perpendicular both to the PSV and to the laser axes.

nozzle of the PSV, which made the formation of laser-induced plasma easier. Once plasma is formed, infrared laser light is absorbed to the plasma in front of the tungsten plate. Therefore, laser abrasion, which vaporizes tungsten atoms (source of contamination), occurs only before the plasma formation. To minimize this contamination problem relating to the tungsten abrasion, the angle of tungsten surface against the AO beam axis was carefully adjusted. Since the angular distribution of metal atoms abraded from surfaces is thought to be a cosine distribution, the surface normal of the tungsten was directed 80° off-axis from the beam axis. Namely, the angle between the tungsten surface and the AO beam was less than 10° (see Figure 2.2). This configuration minimizes tungsten contamination of the specimen surfaces from the tungsten plate, and in fact no tungsten (179 eV) was detectable by AES from the AO-exposed graphite surfaces (see Figure 2.3).

The content of the AO beam depends strongly on the focus position of the laser. To obtain lower ion component and higher AO flux in the beam, proper amount of

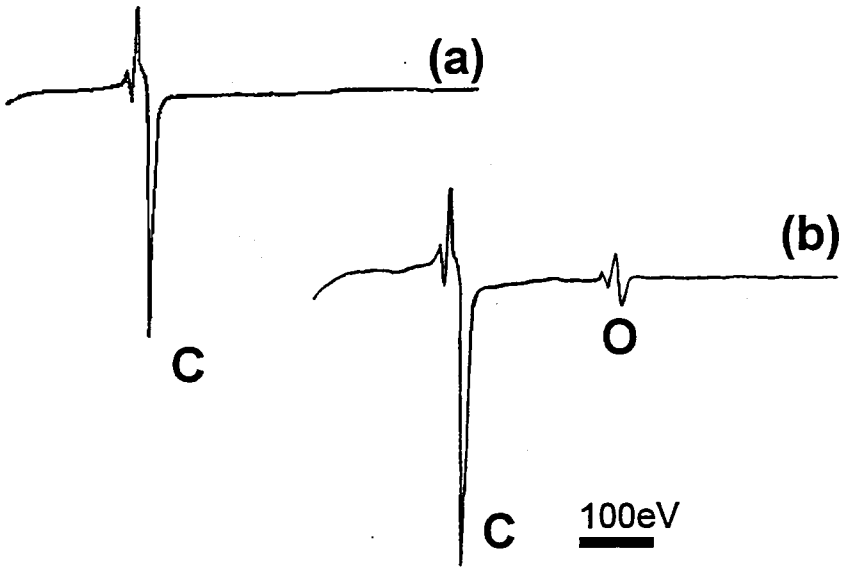

Figure 2.3 The AES spectra of the graphite surface before (a) and after hyperthermal AO exposure using a Q-switched YAG laser-type AO source with a AO fluence of 1.4×10^{17}atoms/cm^2(b). Only Carbon-KLL peak (252eV) is observed before AO exposure. After AO exposure, Oxygen-KLL (512 eV) peak is appeared. No tungsten peak (179 eV) was observed by AES from the AO-exposed graphite.

undecomposed O_2 is needed between the breakdown point and the sample. This adjustment was made by changing the focus position and the delay of the laser firing. These two parameters also influence strongly the translational energy of the AO beam. Therefore, these settings were tuned with monitoring TOF distribution of the AO beam, obtained by the QMS aligned in the AO beam axis.

A digital signal unit was used to adjust the delay time of laser firing, which defined the beam condition (the translational energies and the fluxes of AO and O_2, and the composition). The digital signal unit was also used to set the repetition rate of the AO source. Although the maximum repetition rate of the laser and PSV are 10 and 20 Hz, respectively, the AO source was usually operated at 1 Hz. This is because of the limitation of the pumping speed of the AO source chamber.

To eliminate oxygen ions existing in the AO beam, an electromagnetic ion deflection system was placed in the AO source chamber. A magnetic field generated by a pair of permanent magnets was perpendicular to the AO beam axis. Two sets of electrostatic deflection plates were installed in the magnetic field. One located at 4 cm away from the PSV, the other at 24 cm away from the PSV. Each deflector had two parallel electrodes and +0.1 kV and -3 kV were applied to one of the electrodes of each deflector, whereas the other electrodes were grounded. With the operation of this ion deflection system, no ion signal was observable in the TOF distribution.

2.1.3 Characterization of the hyperthermal AO beam

The composition and translational energy of the AO beam were monitored by the TOF measurement system with QMS. Distance between the breakdown point and the ionizer of QMS was 132.3 cm. Translational energy of the species in the beam was calculated using TOF data and the flight length. The beam passed through the orifice entered directly the ionizer of the QMS in the TOF chamber. The ion species formed in the ionizer were extracted with the kinetic energy of 70 eV, and then selected by the quadrupole mass analyzer. The selected ions were collected by a channeltron. The output of the channeltron was amplified by a fast I-V amplifier, and digitized by a 40 MHz 8-bit A/D converter installed in a personal computer (PC), and then was stored in the PC every 2 μs. A

time of arrival of the output signal from the channeltron was measured with respect to the laser firing.

The mass spectrometer is a number density detector. Moreover, the ionization probability of incoming species in the ionizer of the detector is proportional to the residence time in this ionizer. The relationship between relative flux *I(t)* through the detector and the output signal *N(t)* of the detector will be given by

$$I(t) \propto v \cdot N(t) \qquad (1)$$

where v is the velocity of molecules incoming into the ionizer. If these molecules are ejected at same time from the nozzle throat, the relationship of $v = L/t$ (where L is the flight length of molecule and t is the flight time) can be used. Therefore, equation (1) corresponds to

$$I(t) \propto \frac{1}{t} \cdot N(t) \qquad (2).$$

Every mass charge ratio (m/e) from 1 to 200 was scan-surveyed and only 16 and 32, which correspond to AO and O_2, were detected. These signals were detected only when ionizer was turned on. This fact shows that there contained no ion component in the beam. Figure 2.4 represents typical TOF distributions *N(t)/t* of m/e = 16 (a) and m/e = 32 (b). Compensation was made for the TOF distribution; i.e., the flight time of ions in QMS (from the ionizer to the channeltron) was subtracted in order to calculate the translational energy. The flight time of the ion species formed in the ionizer is proportional to the square root of its mass, because all the ions were accelerated by the same potential difference between the ionizer and the channeltron. The ion flight time of m/e = 16 and 32 were estimated to be 4 μs and 6 μs, respectively, from the TOF data of free expanded argon and neon gases. The time zero in Figure 2.4 corresponds to the laser firing. The detected signal at m/e = 16 include the signal originated from O_2, which cracked to O^+ in the ionizer. The cracked O^+ appeared at the same flight time of O_2 (m/e = 32) and the peak height was estimated to be 7.7 % of the O_2 peak. This was measured from the TOF data of free expanded O_2. After the cracking signal was subtracted from the original TOF distribution, none of signals at a flight time of 1530 μs were obvious (Figure 2.4 (a)). In the m/e = 16 spectrum, a peak at

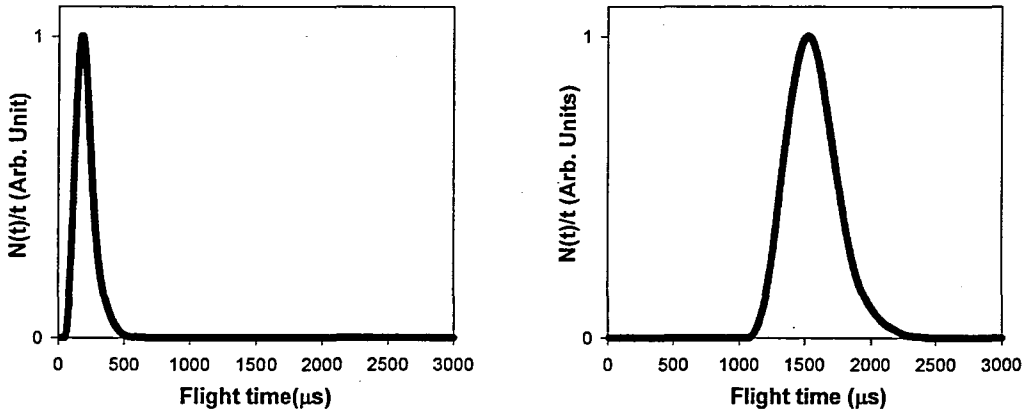

Figure 2.4 Typical TOF distributions of m/e = 16 (a) and m/e = 32 (b) generated from a AO source using the Q-switched YAG laser. The time zero corresponds to the laser firing. The m/e=16 peak originated from O_2 cracking was removed in the spectrum (a).

180 μs came from hyperthermal AO component in the beam. In contrast in the m/e = 32 spectrum, the peak at 1530 μs which corresponded to the free expansion of the surplus O_2 is obvious; no fast peak is observed. I t is known that the laser detonation-type hyperthermal AO source contains hyperthermal O_2 component as well as hyperthermal AO[1]. This hyperthermal O_2 has its kinetic energy twice as high as AO, and influences of hyperthermal O_2 in the beam have to be estimated and compensated from the data which is not an easy task. In contrast, the AO source described here did not include hyperthermal AO component in its AO beam. This is one of the features of this AO source.

We transformed TOF distribution *N(t)* into transitional energy distribution *P(E)* as follows: The relationship between translational energy E of species and t is just

$$E = \frac{1}{2} \cdot mv^2 = \frac{1}{2} \cdot m\left(\frac{L}{t}\right)^2 \qquad (3)$$

where m is mass of the molecule. Therefore, we find the following equation,

$$dE = \frac{1}{2} \cdot mL^2 \cdot \frac{1}{t^3} dt \qquad (4).$$

The $P(E)$ is proportional to the flux (i.e., $P(E)dE \propto I(t)dt$), which lead to the relationship between $P(E)$ and $I(v)$ given by

$$P(E) \propto I(t)\frac{dt}{dE} \propto \frac{1}{t} \cdot N(t) \cdot t^3 = N(t) \cdot t^2 \qquad (5).$$

Using the equation (5), the transitional energy distribution $P(E)$ of AO beam was calculated from the TOF distribution. Figure 2.5 is the transitional energy distribution $P(E)$ of AO beam calculated from Figure 2.4 (a). It is obvious that the mean translational energy of the AO component reaches 4.7 eV, and its full width at half maximum (FWHM) is 5.5 eV.

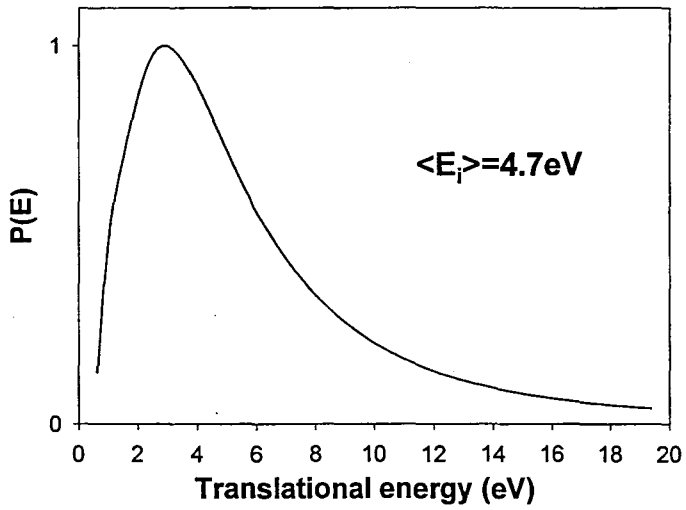

Figure 2.5 Typical translational energy distribution of the AO component in the beam converted from the data shown in Figure 2.4 (a). The mean energy is 4.7 eV, and FWHM is 5.5 eV.

In the space environmental effect community, the erosion rate of polyimide film is the standard for measuring the AO flux[2]. In this study, the flux of AO beam was measured using QCM with silver electrodes[3]. This is because the QCM method for AO flux measurement is more sensitive than using polyimde film erosion rate and can realizes *in-situ* measurement of AO flux. The resonant frequency of QCM decreased with time only when AO beam was irradiated to QCM as shown in Figure 2.6. This is caused by a mass gain of the silver electrode due to the formation of silver oxide. Since silver is not oxidized by O_2 but by AO at room temperature, formation of silver oxide signifies AO reaction at the silver surface. Resonance frequency shift Δf of QCM is expressed in the formula;

$$\Delta f = -f_o^2 \Delta W / NA\rho \qquad (6).$$

where f_o is the resonance frequency of QCM, ΔW the mass change, N the frequency constant, A the electrode area, and ρ the density of quartz. Since N, A, ρ, f_0 are known values, one can calculate the mass change (ΔW) of the sensor crystal from the frequency shift (Δf) of

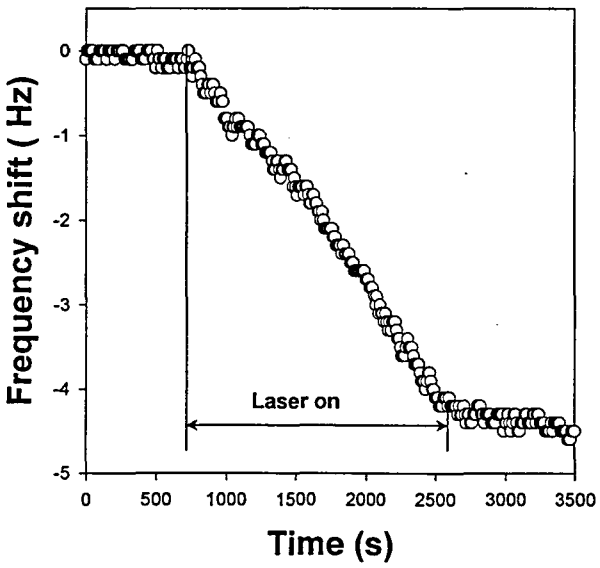

Figure 2.6 Typical frequency shift of QCM during the operation of the AO source. The AO flux is measured from the slope of the graph. The AO flux of 4.0×10^{12} atoms/cm^2/s is calculated from this graph.

QCM. From the slope of Figure 2.6, the AO flux was calculated to be 4.0×10^{12} atoms/cm^2/s at the sample position of 32 cm away from the breakdown point. The reaction and accommodation probabilities were assumed to be 1.0 in this calculation, so that the flux calculated by this equation is a lower bound of the AO flux. To measure accurate AO flux with a QCM with silver electrodes, we need to know the accommodation and the reaction coefficient of the AO/silver system. The flux of AO beam in this source is fairly low, but is corresponding to that in the altitude of 500 km in the LEO environment.

2.1.4 AES and STM

The AES system equipped in this facility was based on PHI model SAM-545A scanning Auger electron spectrometer. This AES system consisted of a single path cylindrical mirror analyzer (CMA) with the coaxial 10 kV electron gun, and 5 kV ion gun for sputtering purpose. Modification of the system was made for sample transfer from the AO source chamber. This AES system had an electron beam scanning control and a secondary electron detector, so that an analysis point on the AO exposed surface can be selected by a scanning electron microscopy (SEM) image.

The homemade STM system was attached directly to the AO source chamber. The piezoelectric transducer (PZT) tripod (X, Y, Z-axes) was used for fine positioning and for scanning of the tip, while coarse positioning of the tip (Z-axis) was done by a micrometer head from the outside of vacuum chamber. This STM had a maximum scanning area of 10 μm × 10 μm. The stroke of the tip driven by the PZT was also 10 μm. The STM was digitally controlled by a personal computer (PC) through a 16-bit AD/DA converter, i. e., software control. Figure 2.7 shows the block diagram of the control circuit and computer interface of the STM system. The sample bias voltage and the driving signals of PZTs were applied through the D/A converter, and the tunneling current was measured through the A/D converter. Feedback control of the tip motion was governed by software and no special hardware was attached to the system. This mean that modifying the control method of the tip for the software control is quite easier, faster, and lower cost than the other STM systems. Scanning tunneling spectroscopy (STS) can also be done with this system. Figure 2.8 shows

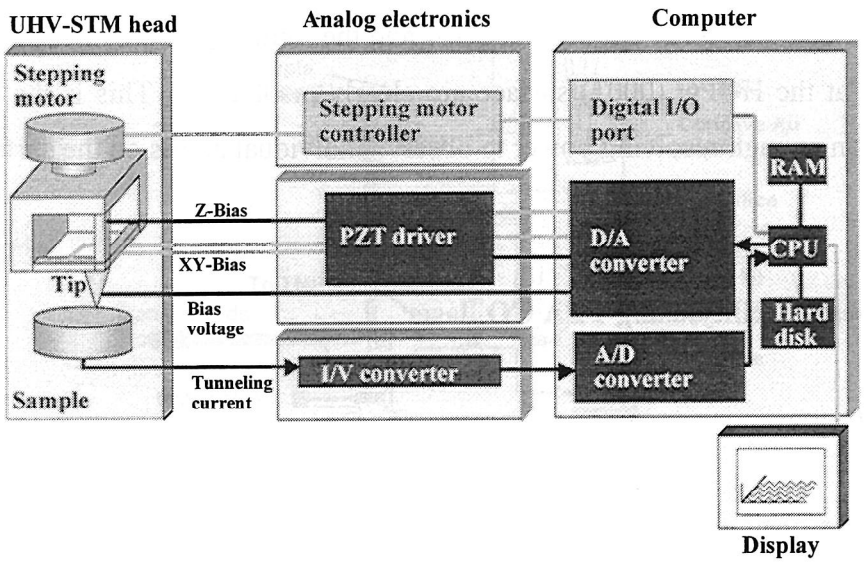

Figure 2.7 Block diagram of the control circuit and computer interface of the STM System.

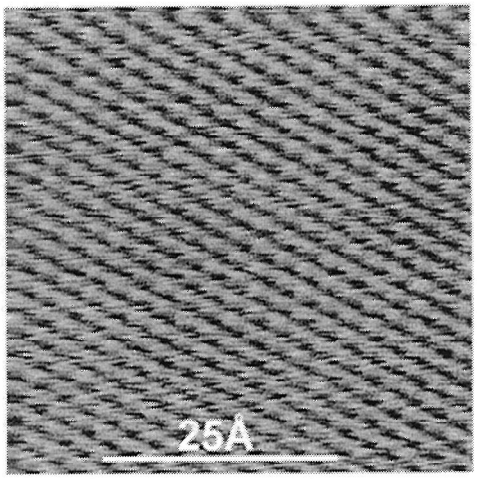

Figure 2.8 The high resolution STM image of the cleaved HOPG surface. Scanning area is 50 x 50 Å. The alpha and beta sites at a HOPG (0001) surface are clearly resolved.

a high resolution STM image of a HOPG surface. Platinum wire with 0.3mm diameter was used as a tip material, and was mechanically finished into a tip shape. The scanning area was 50 × 50 Å, and the tunnel current was 5 nA and the sample bias was 10 mV. The alpha and beta sites at the HOPG (0001) surface are clearly resolved[4]. This is the evidence that this STM has an enough resolving power to observe individual atoms on the surface.

2.2 The AO beam facility using TEA CO_2 laser

2.2.1 General layout

Figure 2.9 shows the overall configuration of the fast AO beam facility using TEA CO_2 laser. This system consists of five vacuum chambers; (a) AO source chamber, (b) reaction chamber, (c) TOF chamber, (d) XPS chamber and (e) preparation chamber. These chambers were evacuated by a 1500 l/s TMP, a 500 l/s TMP, a 300 l/s TMP, a 300 l/s sputter IP, and a 150 l/s TMP, respectively. The vacuum pressure of each chamber were kept in 10^{-6}, 10^{-7}, 10^{-9}, 10^{-8}, and 10^{-5} Pa, respectively. The AO source chamber, the reaction chamber and the TOF chambers were differentially pumped through orifices with diameters of 12 mm and 8 mm, respectively. Since this system was built based on the YAG laser-type AO facility, the layout of the chambers except the AO source is same as that of the YAG laser-type AO facility.

2.2.2 Hyperthermal AO beam source

A detail of the AO source developed in this study is shown in Figure 2.10. This AO source used a TEA CO_2 laser (7 J/pulse) and a solenoid-type PSV. This configuration is originally developed by Caledonia et al. of Physical Science Inc[5]. A 99.95 % pure molecular oxygen was introduced into the nozzle throat within 250 μs. The plenum pressure of the PSV was kept at 18×10^6 Pa. The laser light was focused to the ejected O_2 by means of the concave Au mirror placed 50 cm away from the nozzle. During the laser flush, high

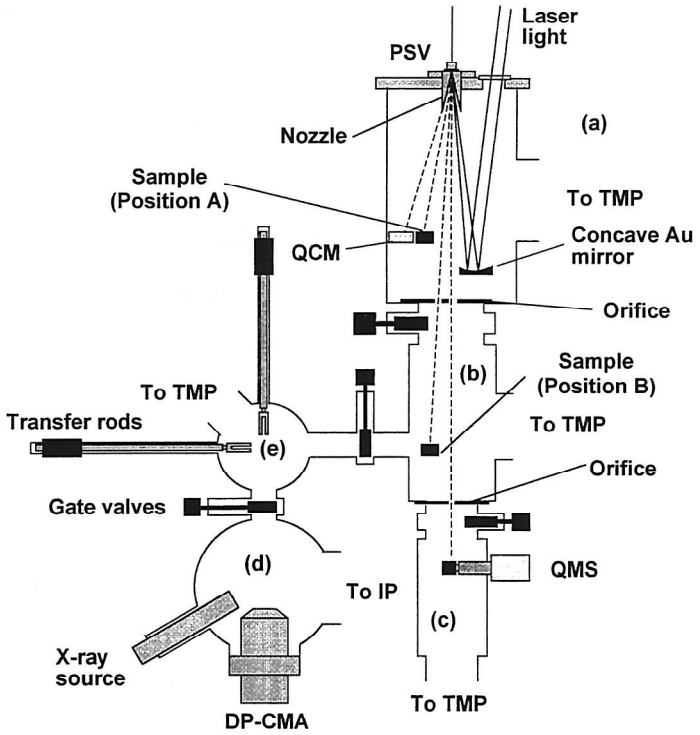

Figure 2.9 A schematic drawing of the AO facility using a TEA CO_2 laser (plane view). This system consists of five UHV-chambers, connected each other with UHV-gate valves. (a) AO source chamber, (b) reaction chamber, (c) TOF chamber, (d) XPS chamber, and (e) preparation chamber.

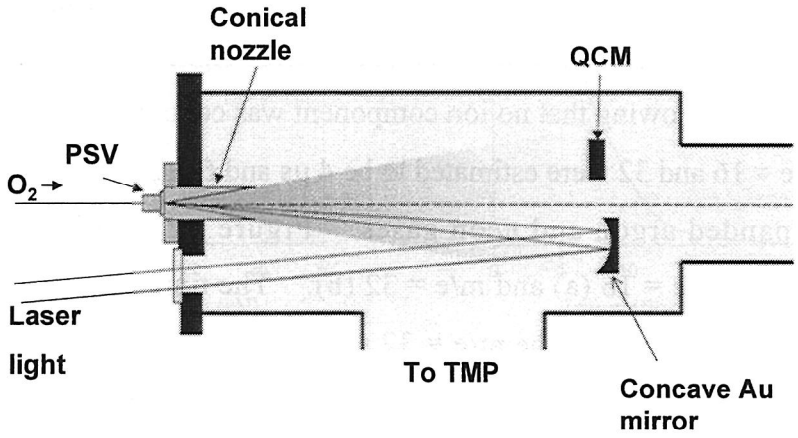

Figure 2.10 Details of the laser detonation-type AO beam source using a TEA CO_2 laser.

temperature plasma and the subsequent laser-initiated detonation wave are being created. When laser light is off, its plasma expands through the nozzle with electron-ion recombination. Expanding the gas's temperature and dropping its density, the velocity of the gas increases.

The TTL electronics was used to adjust the delay time of laser firing, which defined the beam condition (the translational energies and the fluxes of AO and O_2, and the composition). The TTL electronics was also used to set the repetition rate of the AO source, and the AO source was usually operated at 1 Hz.

2.2.3 Characterization of the hyperthermal AO beam

The composition and the translational energy of the AO beam were monitored by the TOF measurement system with QMS. The system is the same as that used in the YAG-laser based AO beam facility described in Section 2.1. In this TOF system, we used a multichannel scalar (MCS) for measuring TOF distributions to eliminate the delay of the analog circuit. The electron counting output of the channeltron was amplified by a pulse amplifier. The time of arrival of the output signal from the channeltron was measured with respect to the laser firing.

When every mass charge ratio (m/e) from 1 to 200 was scan-surveyed, only 16 and 32, corresponding to AO and O_2, were detected. These signals were detected only when ionizer was turned on, showing that no ion component was contained in the beam. The ion flight time of m/e = 16 and 32 were estimated to be 4 μs and 6 μs, respectively, from the TOF data of free expanded argon and neon gases. Figure 2.11 represents typical TOF distributions *N(t)* of m/e = 16 (a) and m/e = 32 (b). The time zero in Figure 2.11 is the moment of the laser firing. In the m/e = 32 spectrum, the peak at 325 μs comes from hyperthermal O_2 and the peak at 2550 μs arises from thermal O_2component. The m/e = 16 signal included the signal originated from O_2 that cracked to O^+ in the ionized region. The cracked O^+ appeared at the same flight time of O_2 (m/e = 32) and the peak height was estimated to be 9 % of the O_2 peak, measured from the TOF data of free expanded O_2. After the cracking signal from O_2 was subtracted from the original TOF distribution, none of the

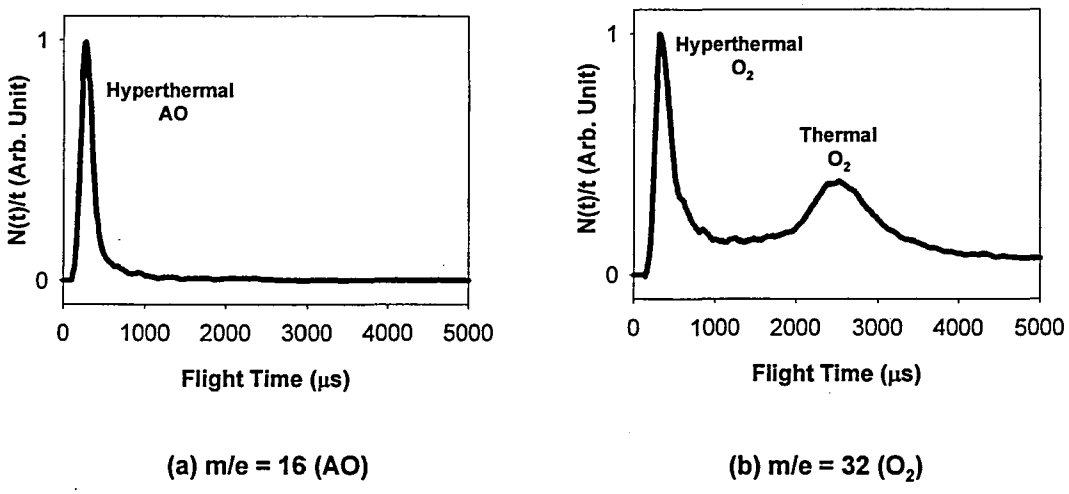

Figure 2.11 Typical TOF distributions of m/e = 16 (a) and m/e = 32 (b) in the AO beam generated from the AO source using the TEA CO_2 laser. Beam composition is 45% hyperthermal AO, 31 % hyperthermal O_2, and 24% thermal O_2.

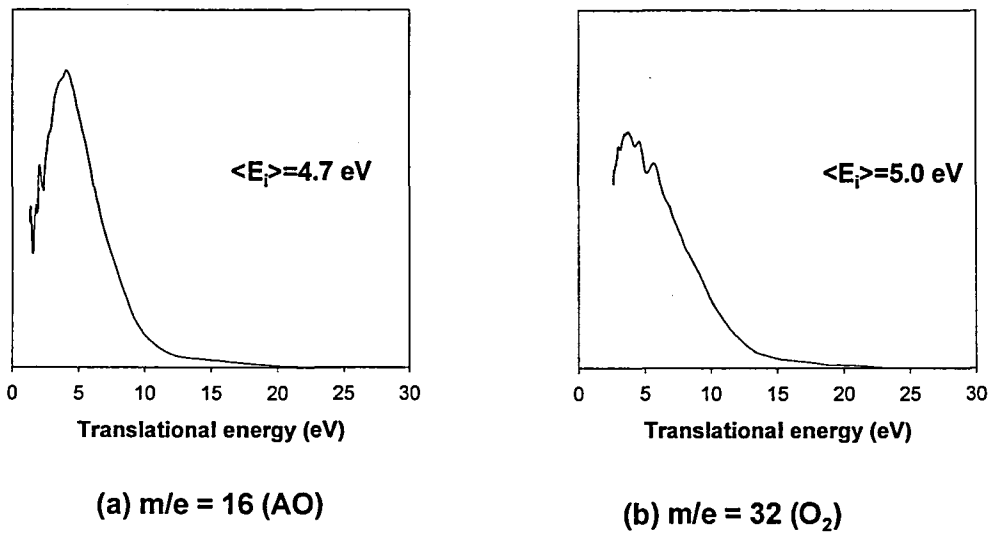

Figure 2.12 Typical translational energy distributions of the AO (a) and O_2 (b) components in the beam converted from the data shown in Figure 2.11 (a) and (b), respectively. Typical mean energies of the hyperthermal AO and O_2 are 4.7eV and 5.0eV, and these FWHM's are 5.5 eV and 6.4 eV, respectively.

signals at a flight time of 2550 μs are obvious as shown in Figure 2.11 (a). In the m/e = 16 spectrum, the peak at 260 μs came from hyperthermal AO component in the beam. The composition of the beam was calculated from the peak area of each component in the spectra using the relative ionization cross section of AO and O_2 are 0.6 : 1[6]. The result was as follows: hyperthermal AO; 45%, hyperthermal O_2; 31%, and thermal O_2; 24%. Translational energy distribution of the species in the beam were calculated using equation (5) with the flight length of 205.0 cm. Figure 2.12 shows the transitional energy distributions *P(E)* of AO and O_2 converted from Figure 2.11. It is obvious that representative mean energies of the hyperthermal AO and O_2 are 4.7 eV and 5.0 eV, respectively, and FWHMs are 5.5 eV and 6.4 eV, respectively.

A flux of AO in the beam was measured using the QCM with silver electrodes. A typical QCM data is demonstrated in Figure 2.13. From the slope of the graph, the AO flux was calculated to be 3.1×10^{14} atoms/cm^2/s at the sample position of 47 cm away from the nozzle. Although, the beam generated from the AO source contained the hyperthermal O_2 component, the AO flux was two orders larger than the YAG laser-type AO source and approximately corresponds to that in the altitude of 250 km in LEO environment.

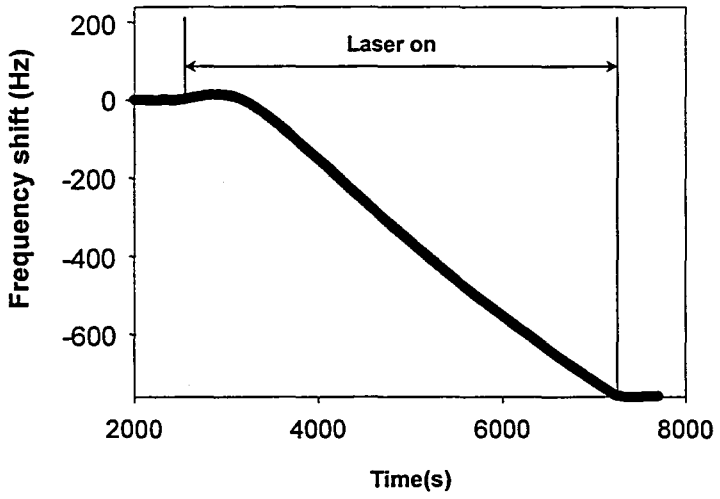

Figure 2.13 Typical frequency shift of QCM during the operation of the AO source. The AO flux is measured from the slope of the graph. The AO flux of 3.1×10^{14} atoms/cm^2 is calculated from this graph.

2.2.4 XPS

The XPS system equipped in this facility consists of a 200 W dual anode X-ray source (Mg and Al, non-monochromatic, TA-10, VSW, England) and a double-path cylindrical mirror analyzer (DP-CMA, DESA-100, STAIB INSTRUNMENTE, Germany). The deconvolutions of the spectra were carried out using computer software. The samples between the reaction chamber and the XPS chamber can be transferred using the transfer rods without breaking the vacuum.

2.3 Other AO beam facilities

2.3.1 The hyperthermal AO beam facility with the rotatable QMS

The AO beam source with a rotatable QMS located at Jet Propulsion Laboratory (JPL) was also used to measure the scattered AO and the reactive products. Figure 2.14 shows a schematic diagram of the facility. This system consists of two vacuum chambers; (a) AO source chamber and (b) main scattering chamber. The AO source chamber was evacuated with 1800 l/s oil DP with a water baffle that was cooled with a refrigerated liquid. The main scattering chamber was evacuated with two cryopumps (CP) and a liquid nitrogen-cooled cryopanel covered the bottom of the chamber. The pressure in the AO source chamber rose to ~6.7×10^{-2} Pa during introducing O_2 and that in main scattering chamber remained $\leq 2.6 \times 10^{-5}$ Pa. The fast AO source attached was the laser detonation-type AO source which was the same as that described in Section 2.2. The AO source used a 5 J/pulse Alltec CO_2 laser and a PSV that was a home-built piezoelectric pulsed molecular beam valve[7]. The AO beam passed through a skimmer with diameter of 1 mm and a synchronized chopper wheel was directed to a sample surface. In addition to a triple differentially pumped ionizer, the rotatable QMS had been carefully designed to detect the reactive products. Any product entering the ionizer was passed though into another differentially pumped region. This means that when species pass through the ionizer without being ionized, almost the species cannot be scattered back into the ionizer. The rotatable QMS had Daly-type ion counter, and

the signal from the ion counter was stored using MCS system. From the TOF data of free expanded gases, the ion flight time for a singly-charged ion of mass m has been estimated to be in μs by the formula $\alpha(m)^{1/2}$ where the parameter α is a function of ion energy and other mass spectrometer parameters. In the setting used in this experiment, α was evaluated to be 2.24. The flight paths from the nozzle throat to sample (L_i) and the sample to the ionizer region of the detector (L_f) were 93 cm and 33.5 cm, respectively, and the detector viewing angle was 3°. The sample and the rotatable QMS detector could be rotated in the same axis, i.e., scattered molecules ejected from a target can be measured as a function of incident and final scattering angles θ_i and θ_f.

The rotatable QMS detector could also be positioned such that the detection axis coincides with the beam axis in order to determine the beam species and their velocity distribution. Figure 2.15 represents typical TOF distributions of m/e = 16 (a) and m/e = 32 (b), which correspond to AO and O_2, respectively. The cracking signal from O_2 in the TOF distribution of AO was subtracted from the original TOF distribution. The time-zero in Figure 2.15 corresponds to the la ser firing. In the m/e = 16 spectrum, the peak at 156 μs came from hyperthermal AO component in the beam. In the m/e = 32 spectrum, the peak at

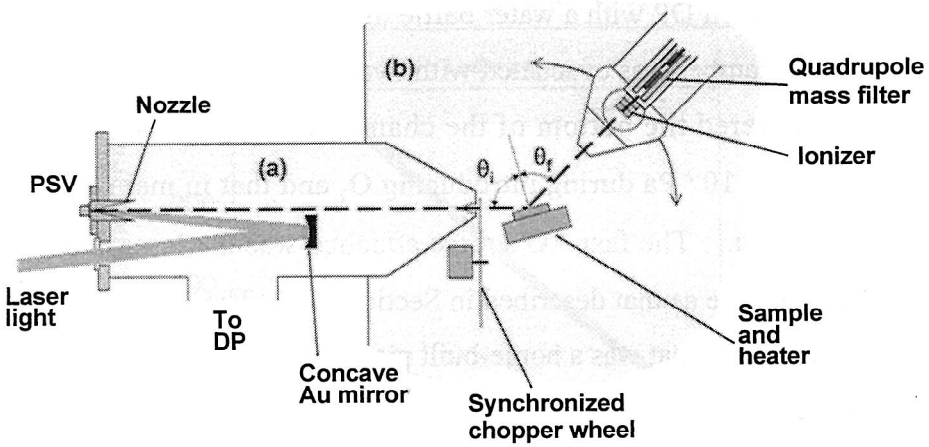

Figure 2.14 The AO facility located at Jet Propulsion Laboratory California Institute Technology. This system consists of two vacuum chambers; (a) AO source chamber and (b) main scattering chamber.

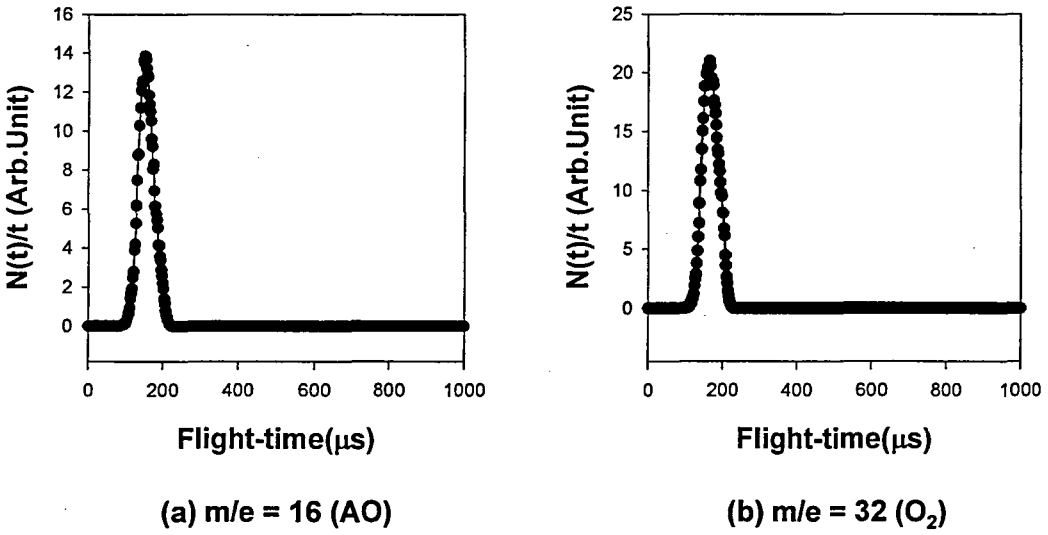

Figure 2.15 Typical TOF distributions of m/e = 16 (a) and m/e = 32 (b) in the AO beam generated from the AO source with the rotatable QMS. The TOF distribution of O_2 in (b) doesn't show thermal component. Beam composition is 56% hyperthermal AO and 44 % hyperthermal O_2.

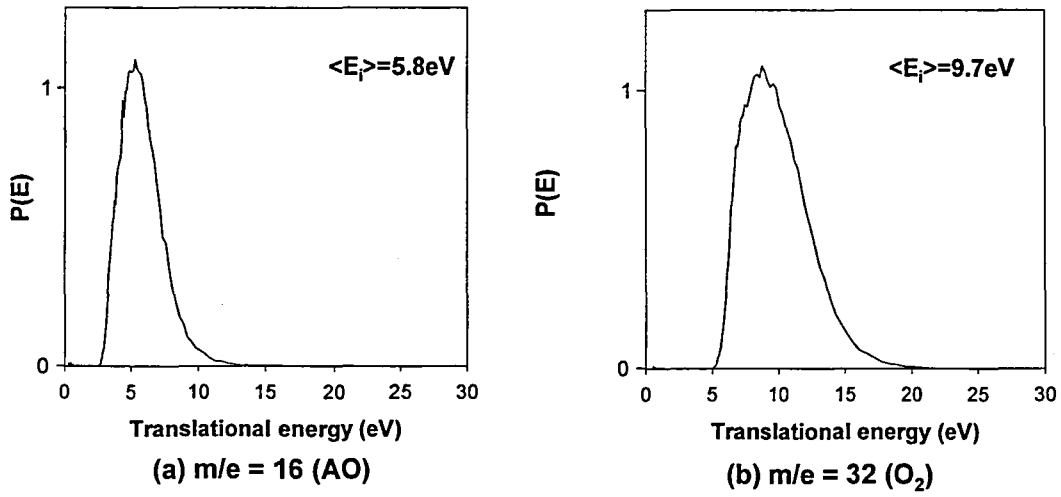

Figure 2.16 Typical translational energy distributions of the AO (a) and O_2 (b) components in the beam converted from the data shown in Figure 2.15 (a) and (b), respectively. Representative mean energies of the hyperthermal AO and O_2 are 5.8 eV and 9.7 eV, and these FWHMs are 3.4 eV and 6.0 eV, respectively.

182 μs arose from hyperthermal O_2, and thermal O_2 component did not exist because it was blocked by the synchronized chopper wheel. The composition of the beam was calculated from the peak area of each component in the spectra using the relative ionization cross section of AO and O_2 are 0.6 : 1. The result was as follows: hyperthermal AO: 56% and hyperthermal O_2: 44%. Figure 2.16 shows the transitional energy distributions *P(E)* of AO and O_2 shown in Figure 2.15. We used the equation (5) to calculate the translational energy and the flight length of 126.5 cm. The mean energies of the hyperthermal AO and O_2 are 5.8 eV and 9.7 eV and these FWHMs are 3.4 eV and 6.0 eV, respectively. Since the AO beam was pass through synchronized chopper wheel, these FWHMs are narrower than that of the AO source described in Section 2.2. The AO flux in the beam, which was estimated from the erosion yield of Kapton-H film, was estimated in the order of 10^{14} atoms/cm^2/s at the sample surface. This facility is now located at Montana State University, Bozeman, Mt.

2.3.2 The ion beam-type AO source

Figure 2.17 schematically represents the ion beam-type AO source used in this study. The length of the facility was about 1.5m. The chamber was evacuated with a differential pumping system consisting of three DP and one TMP. The vacuum was maintained in the order of 10^{-5} Pa in the beam line, and 10^{-6} Pa in the reaction chamber under operational conditions. A Penning ionization gauge (PIG) ion source, which has been known as an electron impact ionization source, was chosen as an oxygen plasma producer. The reason for choosing this type of ionization source is that an ion beam which has a small FWHM of a beam energy is obtained, although the lifetime of its tungsten filament is not long enough in the oxygen plasma. To compensate for this shortcoming, multiple tungsten filaments were placed in the ion source. The exchange tungsten filaments were managed by switching the terminal without causing the vacuum to leak. The PIG ion source was operated at a typical discharge voltage of 60 V with an oxygen pressure of 10^{-1} Pa. A discharge current of more than 700 mA was obtained under these experimental conditions. To avoid inflow of oxygen gas downstream of the facility, the ion source chamber was evacuated by an independent vacuum pumping system with a sufficient pumping speed. Oxygen ions generated in the

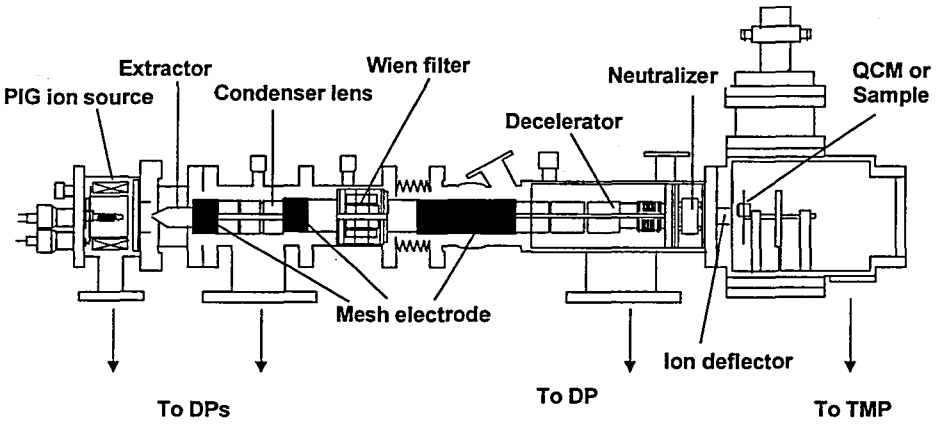

Figure 2.17 The ion beam-type AO source used in this study.

oxygen plasma were extracted with the single hole extraction system, the hole diameter being 1 mm. The divergence of the oxygen beam was about 7°, and the beam was focused by the condenser lenses located next to the extraction electrode. The condenser lens consisted of three electrodes whose diameter is 40 mm. Voltages of the first and the third electrodes are –900 V, which was the same voltage as the extraction voltage, and that of the second electrode was typically kept at –270 V. Impurity ions contained in the oxygen beam were eliminated with a mass filter. A high transmittance and small size were required for the mass filter used in this facility, rather than a high resolution of mass/charge ratio. Thus, a Wien filter 6 cm in length was inserted in the beam line. Magnetic shields with permalloy were attached to both sides of the filter to minimize the influence of leakage of the magnetic field from the Wien filter. The Wien filter also has a role as a bandpass velocity filter. This contributes to the realization of the oxygen ion beam with a small FWHM. Thus, the pure O_2^+ beam enters the deceleration lens consisting of 13 electrodes. This type of decelerator is called a chemical accelerator, and the voltage of each electrode is determined experimentally. The neutralization of oxygen ions was carried out using the decomposition-recombination reaction of oxygen ions under the effect of electrodes in a neutralizer. The high reaction rate of this combination is known by the chemical reaction,

$$O_2^+ + e^- \Longleftrightarrow O_2^* \Rightarrow 2O \qquad (7).$$

In accordance with this reaction, the discharge condition of oxygen at the PIG ion source has been determined experimentally to produce as many O_2^+ ions as possible. Translational energy of O_2^+ ions depends on only the voltage gap between a plasma voltage V_a in the PIG ion source and a voltage V_n in the neutralizer, i.e. V_a- V_n. Considering the reaction (7), translational energy of AO generated corresponds to $(V_a - V_n)/2$. Residual oxygen ions remaining after neutralization were eliminated by an ion deflector placed in front of the samples. Samples and QCM with silver electrodes were mounted on the sample holder that can be rotated along the beam axis. A Faraday cup and viewing hole were equipped on the holder to measure the beam current and to align the axis of the facility straight. The AO flux was measured using the QCM and was calculated to be 4.0×10^{12} atoms/cm^2/s at the sample position.

References

1) B. Cazaubon, A. Paillous, J Siffre, and R. Thomas, "Five-electron-volt atomic oxygen pulsed-beam characterization by quadrupolar mass spectrometry", Journal of Spacecraft and Rockets, vol. 33, (1996), pp. 870-876.

2) M. R. Reddy, "Review Effect of Low Earth Orbit Atomic Oxygen on Spacecraft Materials", Journal of Materials Science, vol. 30 (1995) pp. 281-307.

3) V. Matijasevic, E. L. Garwin, R. H Hammond, "Atomic Oxygen Detection by Silver-coated Quartz Deposition Monitor", Review of Scientific Instruments, vol. 61, (1990), pp.1747-1749.

4) D. Tomanek, S. G. Louie, 1988, First-principles calculation of highly asymmetric structure in scanning-tunneling-microscopy image of graphite, Physical Review B37, (1988), pp. 8327-9336.

5) G. E. Caledonia, R. H. Krech, B. D. Green, "A High Flux Source of Energetic Oxygen Atoms for Material Degradation Studies," AIAA Journal, vol. 25, (1987), pp.59-63.

6) P. B. Cazaubon and B. R. Thomas, "Utilization of Mass Spectrometry for Characterization of the Interaction of Hyperthermal O-atom Beams with materials," Proceedings of 7th International Symposium on Material in a Space Environment, Toulouse, France, SP-399, (1997), pp.185-193.

7) D. Proch and T. Trick, "A High-Intensity Multi-Purpose Piezoelectric Pulsed Molecular Beam Source", Review of Scientific Instruments, vol. 60, (1989), pp. 713.

Chapter 3

Reaction of hyperthermal atomic oxygen with highly oriented pyrolytic graphite

Abstract

In order to investigate the fundamental reaction of hyperthermal AO with solid surfaces, reaction of hyperthermal AO beam with basal plane of HOPG(0001) has been studied using XPS, molecular beam techniques and STM. XPS spectra taken from the AO-exposed HOPG surface indicated the existence of surface oxide. The oxygen coverage reached the saturated value, moreover, the saturated oxygen coverage decreased with increasing sample temperature T_s. The TOF distribution of scattered AO from the AO-exposed HOPG surface showed inelastic scattering and trapping desorption processes. The volatile species from the AO-exposed HOPG surface were only CO and CO_2 with bimodal TOF distributions. The initial reaction site of the AO-exposed HOPG surface was observed as a protrusion in STM images. In contrast, a hillock-like structure was formed on the surfaces at high AO fluences. From the density of protrusion, the reaction yield of hyperthermal AO with the defect-free HOPG (0001) surface was estimated to be 1.0×10^{-3}, which was two orders lower than that in flight experiment. This discrepancy was explained by the formation of the hillock-like structure on the AO-exposed HOPG surface at high AO fluence.

3.1 Introduction

In order to investigate the degradation phenomenon due to the hyperthermal AO attack in the LEO experiment, both flight and ground-based experiments have been conducted. Samples in these experiments have mainly been selected from the practical materials for space use such as polymeric materials or paints. This is because the behavior of these

materials with hyperthermal AO in the LEO environment are practically important in order to achieve low risk missions. However, the reactions of such practical materials are complicated because of their complex chemical structure. Therefore, it has been difficult to specify the fundamental physics and chemistry at the AO-exposed surfaces.

We report herein the reaction dynamics of hyperthermal AO beam with HOPG in order to investigate the fundamental reaction of hyperthermal AO with solid surfaces. HOPG is all most single crystal of graphite and the HOPG (0001) surface (basal plane) is a chemically stable and atomically flat. For these properties, HOPG is one of the materials most commonly used in the investigations of gas-surface reactions. From the engineering point of view, AO reaction with graphite is important to know for predicting the survivability of the carbon-based materials used in the LEO environment. This is because mechanical property of carbon fiber depends on the graphite layers at the peripheral of the fiber. The TOF distributions of the scattered molecules and volatile products from the HOPG surface were measured by molecular beam techniques. Analyses of the HOPG surfaces were performed by XPS and STM.

3.2 Experiments

Two fast AO beam facilities were used in the study. One facility at JPL was equipped with a rotatable mass spectrometer detector and was used for analyzing the fluxes and energies of the scattered species as well as those of the reactive products from the HOPG surfaces. The other facility at Osaka University was for the surface characterization of the AO-exposed HOPG surfaces and was equipped XPS and STM. The details of these facilities been presented in chapter 2. Both facilities had the same type of AO source, i. e., laser detonation-type AO beam sources originally invented by PSI[1]. The AO beams generated at the AO sources were characterized by the TOF spectra as written in the sections 2.2.3 and 2.3.1.

HOPG crystals (Union Carbide Corporation, grade ZYA) were cleaved in air and immediately installed into the vacuum chamber. The HOPG (0001) surfaces were exposed to the energetic AO beam at sample temperatures ranging between 300 K and 600K. In STM measurement, the mechanically finished Pt wire was used as a tip. The STM images

were taken in air at room temperature by the constant-current mode at the sample bias voltage of +10 mV, and at the tunneling current of 1 to 8 nA.

3.3 Profile fitting for TOF distributions of the scattered molecules

The mass spectrometer is a number density detector. Moreover, the ionization probability of incoming species in the ionizer of the detector is proportional to the residence time in the ionizer. Thus, the relationship between relative flux $I_{in}(t)$ through the detector and the output signal $N_{out}(t)$ of the detector will be given by

$$I_{in}(t) \propto v \cdot N_{out}(t) \qquad (1)$$

where v is the velocity of molecules. If we neglect the distribution of the arrival time of the incoming AO species, the relationship of $v = L/t$ (where L is the flight length of molecule and t is the flight time) can be used. Therefore, equation (1) can be rewritten as follows;

$$I_{in}(t) \propto \frac{1}{t} \cdot N_{out}(t) \qquad (2).$$

Moreover, according to the relationship of $I_{in}(v)dv \propto I_{in}(t)dt$ and $dv = -\frac{1}{t^2}dt$, the velocity distributions $I_{in}(v)$ can be described by

$$I_{in}(v) = I_{in}(t) \cdot \frac{dt}{dv} \propto t^2 \cdot I_{in}(t) \qquad (3).$$

The translational energy distributions $P(E)$ is proportional to the flux (i.e., $P(E)dE \propto I(v)dv$), which lead to the relationship between $P(E)$ and $I_{in}(v)$ given by

$$P(E) = I_{in}(v) \cdot \frac{dv}{dE} \qquad (4).$$

There is the relationship of $E = \frac{1}{2}mv^2$, thus $dE = mv \cdot dv$. Therefore, equation (4) can be rewritten as follows;

$$P(E) \propto \frac{1}{v} \cdot I_{in}(v) \qquad (5).$$

These equations have been applied successfully for analyzing many TOF distributions observed in the molecular beam technique with a chopper wheel.

However, in the case when the pulse width of the incident beam is not short enough, the distribution of the time-zero in the TOF spectra should be considered. The broadening distribution of time-zero leads to the broadening of TOF spectra of the scattered molecules, i. e., the calculated flux and energy of the scattered molecules have large errors. Thus, a quality of the data analysis of the TOF distributions of the scattered molecules affected greatly by the incident beam velocity distribution. In order to analyze the TOF distribution $N_{rec}(t)$ recorded by QMS with a relatively large incident beam velocity distribution, we propose the use of fitting function $N_{fit}(t)$ by modifying the original function given by Hurst et al.[2] in order to employ the time-zero of the TOF distribution that was corresponded to the laser firing.

The $N_{fit}(t)$ consisted of the flight time t_i from the nozzle throat to the sample surface (= L_i/v_i, where L_i is the flight time of incident species and v_i is the incident velocity), and the flight time t_f from the surface to the ionizer (= $t - t_i = L_f / v_f$, where t is the recorded time with respect to the laser firing as time-zero, L_f the flight length of the scattered species and v_f the final velocity). In this study, we assumed that residence time in surface was negligible small. An incident specie with the incident velocity of v_i yielded the single-particle scattering velocity distribution R which gives the final velocity distribution. The distribution R is independent of the AO flux, $D(t_i)$, at the sample surface. Therefore, taking into account all these contributions, $N_{fit}(t)$ is described by the following equation,

$$N_{fit}(t) = \int_0^t D(t_i) \cdot R\left(\frac{L_f}{t-t_i}, \frac{L_i}{t_i}\right) \frac{dt_i}{t-t_i} \qquad (5).$$

In many system, it is seen a bimodal TOF spectrum of the scattered species when a hyperthermal beam is scattered at a solid surface[5]. As is described in the following section, all TOF distributions of the scattered molecules consisted these two components. So that we assumed the velocity distributions R_s for the slow component and R_f for the fast component, independently. The slow component usually consists of the scattered species that are in thermal equilibrium with the sample surface. Therefore, the slow component approximately follows the Maxwell-Boltzmann (M-B) distribution[3]. Therefore, R_s can be written as

$$R_s(v_f) = A{v_f}^3 \exp\left(\frac{-m{v_f}^2}{2kT_{eff}}\right) \tag{6}$$

subject to

$$\int_{v_f=0}^{v_f=\infty} R_s(v_f)dv_f = 1$$

where m is the mass of the scattered molecule, T_{eff} is the effective translational temperature, which is close to the surface temperature T_s, k is Boltzmann constant and A is a constant. $R_s(v_f)$ is, thus, independent of the incident velocity of the incoming molecule. In contrast, the fast component is described using a form corresponding to a shifted M-B velocity distribution[3]. So, we assume that R_f is written as

$$R_f(v_f, v_i) = B{v_f}^3 \exp\left(\frac{(v_f - v_a(v_i))^2}{\alpha_a(v_i)^2}\right) \tag{7}$$

subject to

$$\int_{v_f=0}^{v_f=\infty} R_f(v_f, v_i)dv_f = 1$$

where, v_a is a flow velocity, α_a is a spreading parameter and B is the constant. The v_a and α_a

may be expected to decrease with decreasing the velocity of incident species. In fact, it has been reported that the decrease of v_a was observed when velocity of incident species was decreased[2]. In this study, we assumed the velocity of the scattered molecules relates to that of the incident species, and v_a and α_a are represented in the following experimental equations;

$$v_a\left(\frac{L_i}{t_i}\right)=\frac{L_i}{t_A+t_B\cdot t_i}$$
$$\alpha_a\left(\frac{L_i}{t_i}\right)=\frac{L_i}{t_C+t_D\cdot t_i} \qquad (8)$$

where t_A, t_B, t_C, and t_D are fitting parameters. Using equations (7) and (8), equations (6) can be expressed by the following equation;

$$N_{fit}(t)=\int_0^t D(t_i)\left\{N_f R_f\left(\frac{L_f}{t-t_i},\frac{L_i}{t_i}\right)+N_s R_s\left(\frac{L_f}{t-t_i}\right)\right\}\frac{dt_i}{t-t_i} \qquad (9).$$

The respective normalization constants, N_f and N_s, determine the contribution of the fast and slow components to the whole TOF spectrum. All TOF distributions of the scattered molecules obtained in this study were curve-fitted using the equation (9) with a known $D(t_i)$ calculated from the profile of the incident beam. The mean translational energies and fluxes of the fast and slow components of the scattered molecules were also calculated using equation (9).

3.4 Results and discussion

3.4.1 Surface oxidation

The XPS survey spectra taken from the HOPG surface before and after exposure to hyperthermal AO beam with AO fluence of 8.3×10^{17} atoms/cm^2 at T_s = 300 K are displayed in Figures 3.1 (a) and (b), respectively. The XPS spectrum before the AO exposure shows

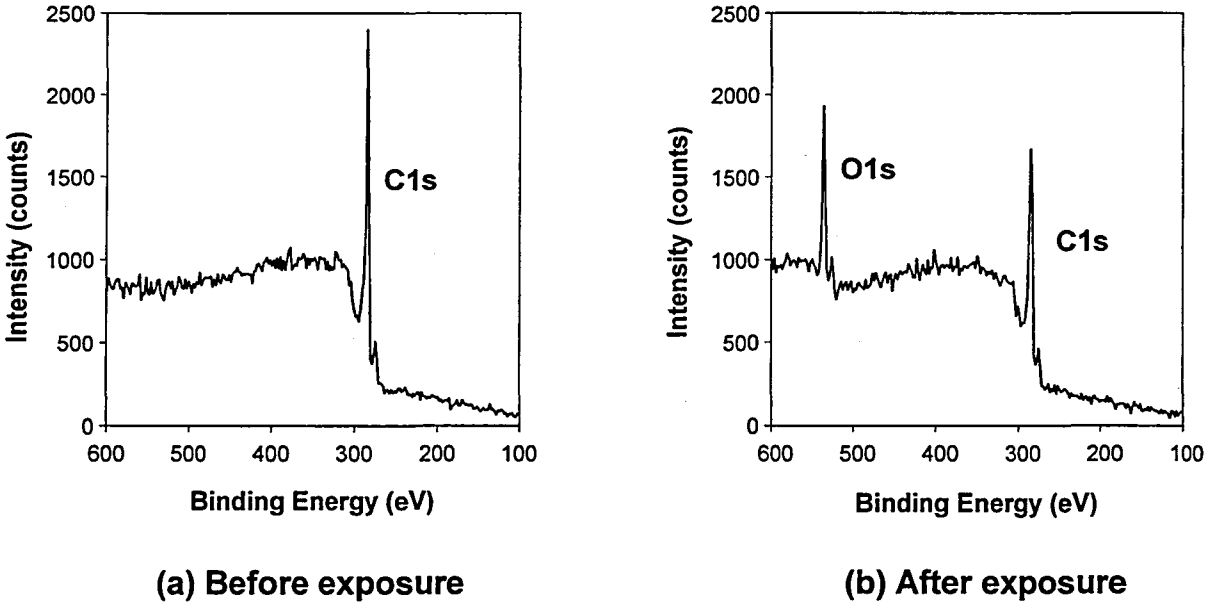

Figure 3.1 The XPS spectra of the HOPG surface before (a) and after exposure to energetic AO beam with the AO fluence of 8.3×10^{17} atoms/cm^2 at 300 K(b).

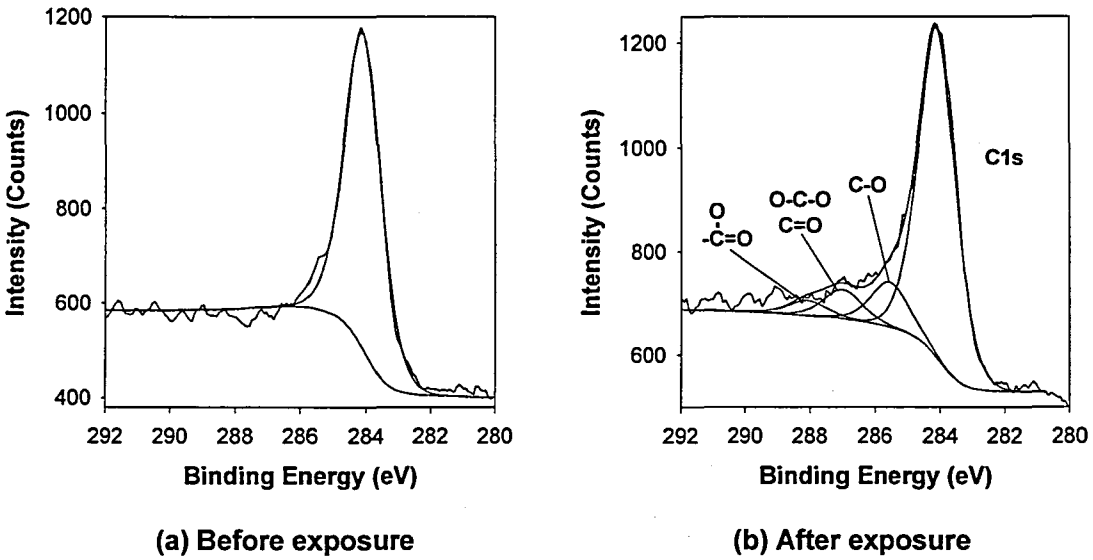

Figure 3.2 The XPS C1s core level spectra of the HOPG (0001) surfaces before (a) and after hyperthermal AO exposure with the fluence of 8.3×10^{17} atoms/cm^2 (b).

only C1s peak (284eV). However, O1s peak (530eV) is also obvious in the spectrum after hyperthermal AO exposure. Figures 3.2 (a) and (b) represent the high resolution C1s core-level spectra taken from the same samples of Figures 3.1 (a) and (b), respectively. The C1s peak with the binding energy of 284.1 eV reveals C-C bond of the graphite structure. However, high-energy tail of the C1s peak is clearly obvious in Figure 3.2 (b). Such a high-energy tail (chemical shift) indicates the oxidation of carbon atoms. The chemical shifts of C1s peak in the XPS spectra can be predicted by the group theory[4]. The chemical shift of C1s XPS peak is reported to be +1.5 eV per an oxygen-carbon bond. Many possible surface functional groups at the oxidized HOPG surface are expected to have carbon/oxygen structures of C-O, C=O, O-C-O, and/or O-C=O. These carbon/oxygen structures show the chemical shifts of approximately 1.5, 3.0, 3.0, and 4.5 eV, respectively. This fact suggests that the chemical shifts of C1s XPS peak at the oxidized HOPG surface are consisted of three components. More directly, the oxidation states of carbon atoms at the HOPG (0001) during the exposure to oxygen ion beam and oxygen plasma were reported by Nowakowski et al.[5]. They showed a spectroscopic evidence for the presence of semi-quinone (equivalent to carbonyl group) on the HOPG surface after the exposure. The presence of semi-quinone and

Table 3.1 The deconvolution result of the C1s core level spectrum of the AO-exposed HOPG with fluence of 8.3×10^{17} atoms/cm^2.

Peak position (eV)	284.10	285.55	287.00	288.09
Peak shift relative to graphite (eV)	0	1.45	2.90	3.99
Relative peak area (%)	78	11	7	4
Assignments	C-C in graphite	C-O	O-C-O C=O	O -C=O

lactone (equivalent to carboxyl group) on the oxygen adsorbed graphite surface have also been reported by Marchon et al.[6]. The chemical shifts of C1s core level due to the formation of such surface functional groups were also referred to the literature[7] and we have used the chemical shifts listed herein. These published values are close to those calculated from the group theory. Therefore, the peak deconvolution of C1s XPS spectra in this study was carried out with these three types oxidation states at the HOPG surface. The result of peak deconvolution is represented in Table 3.1. An error in the fraction of each oxidation state of carbon was estimated to be in the order of a few percent. It is obvious in Table 3.1 that the relative area of the carbon peak showing the chemical shift of 1.45 eV (C-O) is three times larger than that of 3.99 eV (O-C=O). This deconvolution result suggests that a number of oxygen atoms on the AO-exposed HOPG surface are existed in the bridge site. The fraction of carbon atoms showing any chemical shift is 22 % of the total intensity of C1s signal. Considering the escape depth of the C1s photoelectron, the high fraction of oxidized carbon atoms (22 %) indicated that the HOPG surface was almost completely covered by the chemically adsorbed oxygen at the AO fluence of 8.3×10^{17} atoms/cm^2.

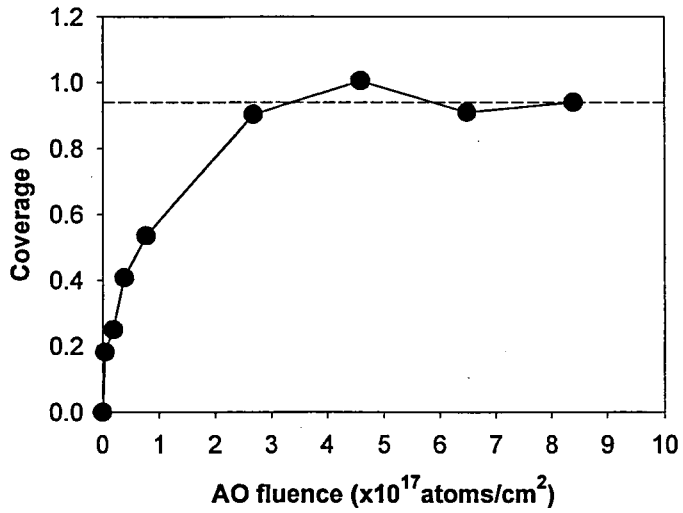

Figure 3.3 The relationship between the oxygen coverage and the AO fluence measured from the XPS spectra at $T_s = 300$ K.

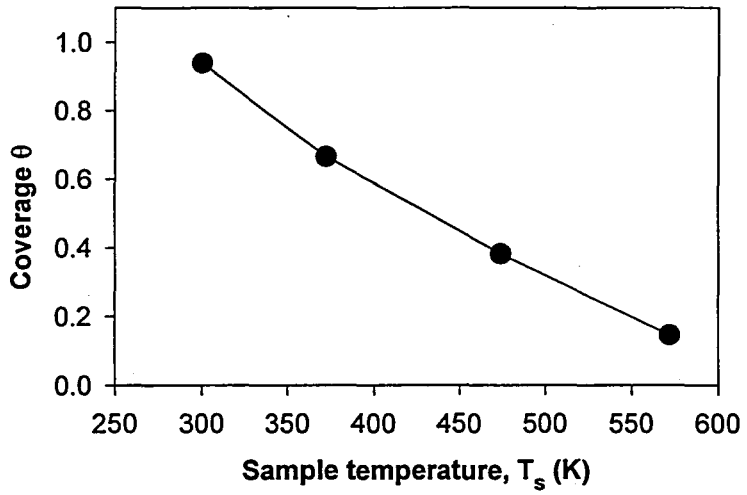

Figure 3.4 The temperature dependence of the oxygen coverage obtained from XPS spectra: E_i = 4.7eV, AO fluence of 2.8×10^{17} atoms/cm^2.

Total amount of oxygen adsorbed on the AO-exposed HOPG (0001) was calculated with the relative peak areas of the C1s and O1s peaks in the XPS spectra. As will be discussed later, since collision energies of molecules in the beam are lower than the penetration threshold of HOPG, oxygen atoms are considered to exist only at the topmost layer. In order to compensate the effect of C1s photoelectrons from the subsurface region, the escape depth of C1s photoelectrons were estimated. The escape depth of photoelectron is equivalent to the attenuation length and the inelastic mean free path. The attenuated length and the inelastic mean free path of the C1s photoelectrons activated by the Al Kα line (1486.6 eV) are calculated to be approximately 24-26 Å. Taking into account the average take-off angle of photoelectrons to the DP-CMA (45°), the escape depth of the C1s photoelectrons is expected to be 18 Å, i. e., 5.3 layers (d/2 = 3.35 Å, d: lattice constant of HOPG along with c-axis). Assuming that the density of adsorption site (bridge site) is the same as that of carbon atoms in HOPG (0001), the oxygen coverage θ was described by the following equation;

$$\theta = \left(\frac{S_O}{I_O}\right) / \left(\frac{S_C}{I_C \cdot \lambda_C}\right) \tag{10}$$

where S_O and S_C are the relative peak areas of O1s and C1s XPS peak, respectively, I_O and I_C are relative photoionization cross sections of C1s and O1s (I_O : I_C = 1 : 2.93), and λ_C is the number of graphite layers within the escape depth of C1s photoelectrons (5.3 layers). Figure 3.3 displays the relationship between the AO fluence and the oxygen coverage thus calculated. It is observed that the oxygen coverage increases with the AO fluence and it reaches the saturated value of θ = 0.94 at the AO fluence of approximately 2.5 × 10^{17} atoms/cm^2. The saturated oxygen coverage were also measured at the HOPG surface exposed to hyperthermal AO beam with E_i = 4.7 eV, and AO fluence of 2.8 × 10^{17} atoms/cm^2 at the three different sample temperature of 369 K, 472 K, and 569 K. Figure 3.4 indicates the relationship between oxygen coverage and the surface temperature. It is indicated that the hyperthermal AO-exposed HOPG (0001) surface is almost fully covered by the adsorbed oxygen at T_s = 300 K (θ= 0.94), however, the oxygen coverage decreases with sample temperature and it reaches θ= 0.16 at 569 K. This result suggests that the incoming AO collides with the adsorbed oxygen atoms (or oxide) at 300 K, but with the carbon atoms at higher temperatures.

3.4.2 Scattered molecules and volatile reaction products

When the hyperthermal AO beam encountered the clean HOPG (0001) surface, not only the scattering of AO and MO signals, but also CO and CO_2 signals were detected as reactive products. No other signal was detected even though every mass charge ratio (m/e) from 1 to 200 was scan-surveyed.

Figure 3.5 shows the TOF distributions of scattered AO collected at T_s = 300 K with E_i = 5.7 eV, and T_s = 583 K with E_i = 5.1 eV. The incident and final angles are at θ_i = 60° and θ_f = 60°. Both TOF distributions are bimodal, i. e., a fast component (early arrived) and a slow component (late arrived) are obvious. The solid curves show the fitting results of the fast and slow components using equations (5)-(9). The relative fluxes and translational energies of these components were estimated from the fitting results. The composition of the fast AO component was larger than 80 % in many cases. The mean translational energies of these fast components are far greater than kT_s. In contrast, the slow components

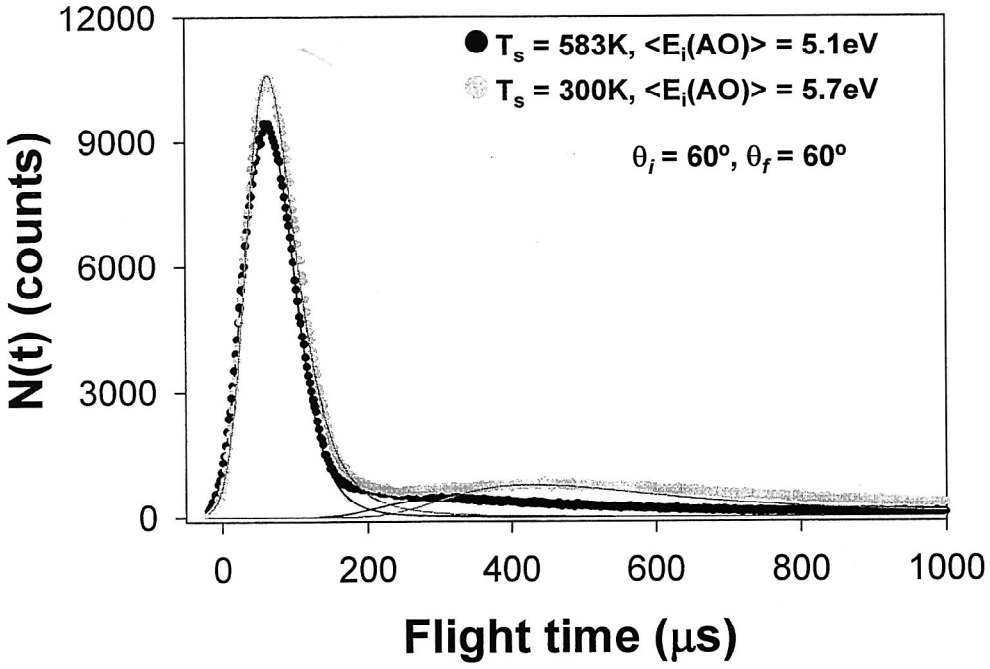

Figure 3.5 The temperature dependence of the oxygen coverage obtained from XPS spectra: E_i = 4.7eV, AO fluence of 2.8×10^{17} atoms/cm^2.

approximately corresponds to the M-B distribution with the energy of kT_s. The polar plots of the relative fluxes of the fast and slow components of the scattered AO collected at various incident angles are shown in Figure 3.6. The relative fluxes of the fast components for θ_f = 60° were fitted by the function $f(\theta_f) = \cos^n(\theta_f - \theta_{peak})$, where θ_{peak} is the angle which showed the maximum intensity. The best-fit result is shown in Figure 3.6 (a), with n = 1.2 and θ_{peak} = 78°. The angular distribution of the fast component is narrower than a cosine distribution and asymmetric with respect to the surface normal. The relative flux of the fast component becomes high when the incident angle or the final angle is large with respect to surface normal. In the case of slow component, the angular distribution approximately follows a $\cos(\theta_f)$ distribution. The behaviors that the slow component obeys the M-B distribution and the cosine law imply that the slow component trapped on the surface long enough to reach the thermal equilibrium, i. e., trapping desorption[8]. Figure 3.7 represents the mean translational

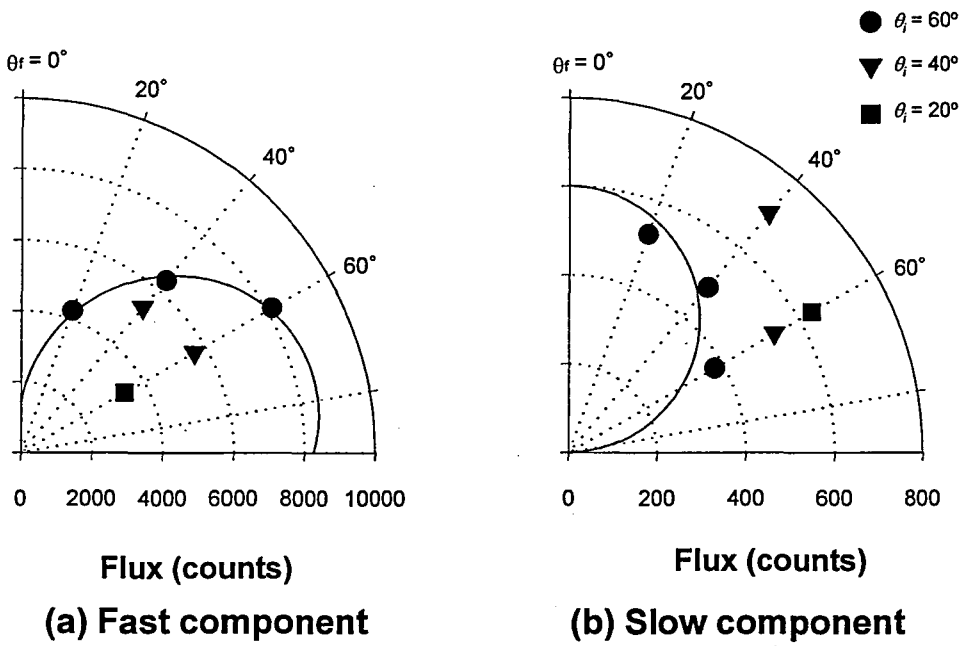

Figure 3.6 The polar plots of the relative fluxes of the fast (a) and slow (a) components of the scattered AO collected at various incident angle at T_s = 300 K. The solid curve in (a) corresponds to $f(\theta_f) = \cos^{1.2}(\theta_f - 78°)$, whereas that in (b) does $f(\theta_f) = \cos\theta_f$.

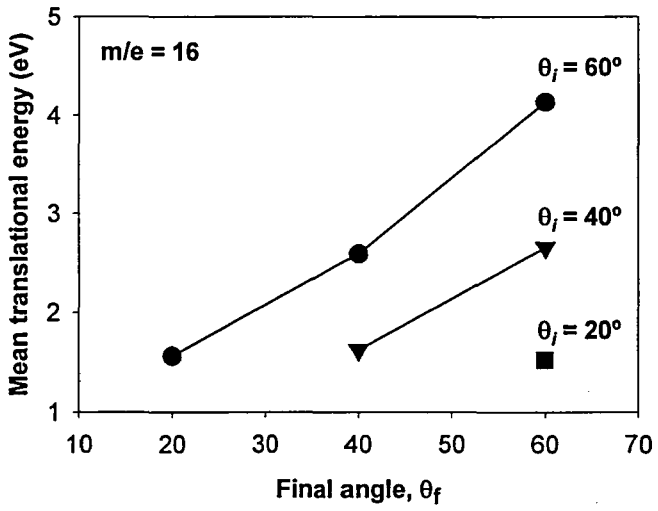

Figure 3.7 The mean translational energies of the fast component of the scattered AO collected at various incident and final angles at T_s = 300 K.

energies of the fast component at the various incident angles at T_s = 300 K as a function of final angle. The translational energy of the fast component increases with increasing the incident angle and the final angle. It is also observed that the translational energy of the fast component is proportional to the reflection angle ($\theta_i + \theta_f$). It has been reported that these behaviors of the fast AO component clearly are evidence that the fast AO component arise from inelastic scattering[8].

The TOF distributions of CO and CO_2 with the incident energy of E_i = 6.3 eV, at T_s = 332 K and T_s = 598 K, are shown in Figure 3.8. Both CO and CO_2 distributions show two peaks. The fast and slow components were fitted by the equations (5)-(9), and the solid curves in Figure 3.8 show the fitting results. The relative fluxes and translational energies of CO and CO_2 components were estimated by the fitting results. The slow components of CO and CO_2 approximately follow the M-B distribution at both of the sample temperatures. Figure 3.9 and Figure 3.10 represent the polar plot of the relative fluxes of the fast and slow components of CO and CO_2 at T_s = 300 K, respectively. The slow components of CO and CO_2 are close to a cosine distribution, however, the fast components are a symmetric with

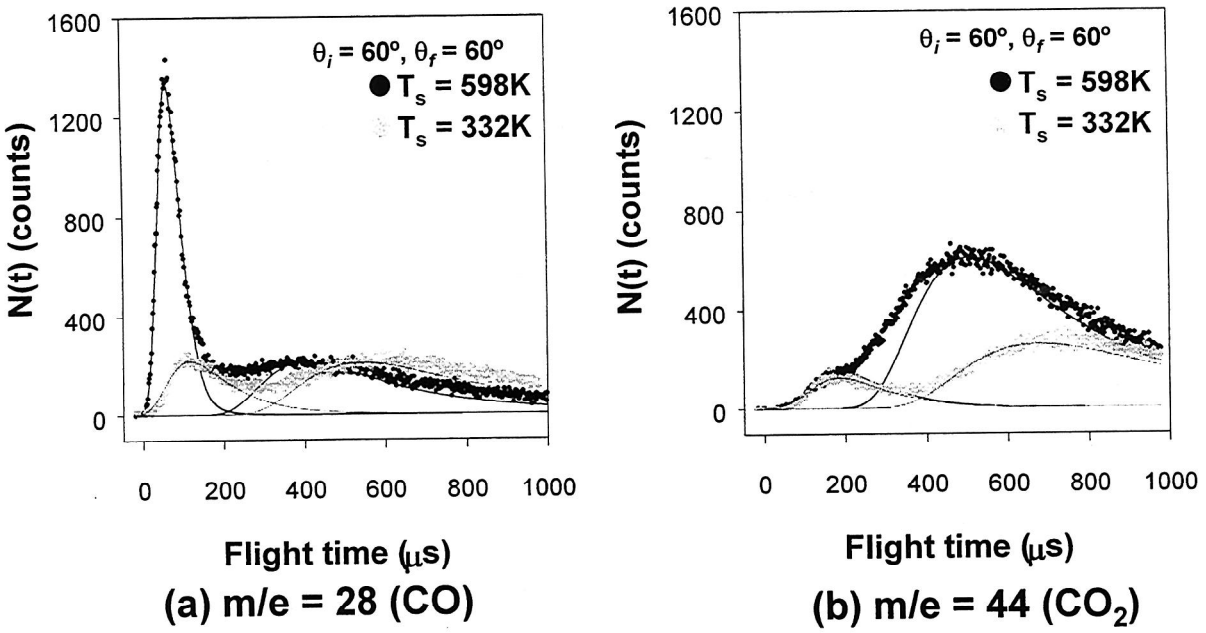

Figure 3.8 The TOF distributions of CO (a) and CO_2 (b): E_i = 6.3 eV, T_s = 332 K and T_s = 598 K. The time zero corresponds to the laser firing. The solid curves indicate the deconvolution results.

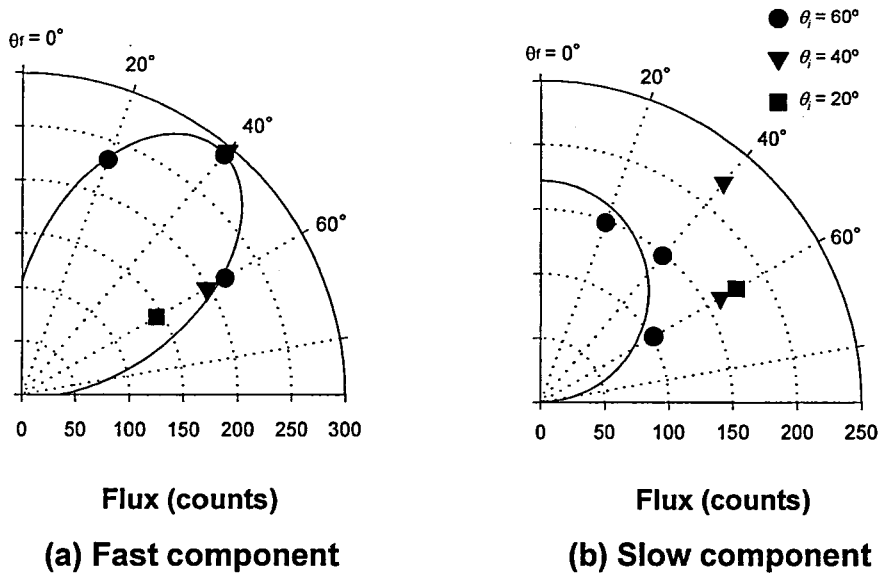

Figure 3.9 The relative CO fluxes of the fast (a) and slow (b) components at T_s = 300 K. The solid curve in the fast component corresponds to $f(\theta_f) = \cos^{4.3}(\theta_f - 39°)$, whereas that in (b) does $f(\theta_f) = \cos\theta_f$.

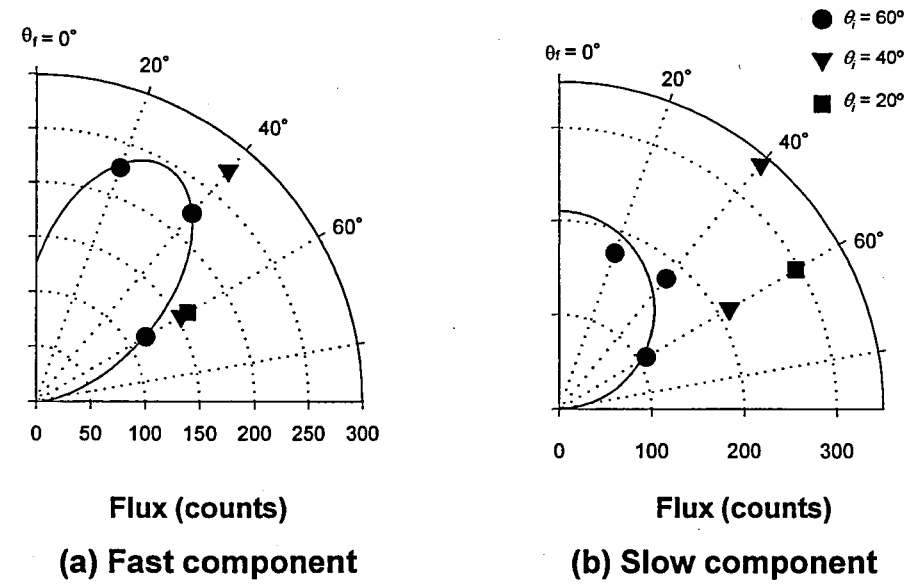

Figure 3.10 The relative CO_2 fluxes of the fast (a) and slow (b) components, at T_s = 300 K. The solid curve in the fast component corresponds to $f(\theta_f) = \cos^{5.0}(\theta_f - 30°)$, whereas that in (b) does $f(\theta_f) = \cos\theta_f$.

respect to the surface normal. The plots of the fast components of CO and CO_2 for $\theta_f = 60°$ were fitted by the form: $f(\theta_f) = \cos^n(\theta_f - \theta_{peak})$. The solid curves in Figure 3.9 (a) and Figure 3.10 (a) show the fitting results with $n = 4.3$, $\theta_{peak} = 39°$ for CO, and $n = 5.0$, $\theta_{peak} = 30°$ for CO_2, respectively. Figure 3.11 represents the mean translational energy of the fast component of CO and CO_2 at $T_s = 300$ K as a function of the exit angle. The increases of these energies with increasing reflection angle ($\theta_i + \theta_f$) are obvious.

The TOF distributions of CO and CO_2 were also measured with four sample temperatures at $T_s = 332$, 419, 517, and 598 K, with $\theta_i = 60°$ and $\theta_f = 60°$ (not shown). The energy distribution of the slow components in the TOF distributions of CO and CO_2 approximately corresponded to the M-B distribution at the sample temperatures. The fluxes of the fast and slow component of CO and CO_2 calculated from the deconvolution results of the TOF distributions are summarized in Figure 3.12. The flux of the slow component of CO is independent of the sample temperature, however, that of the fast CO component increases with the sample temperature (Figure 3.12 (a)). In contrast, the increase of sample

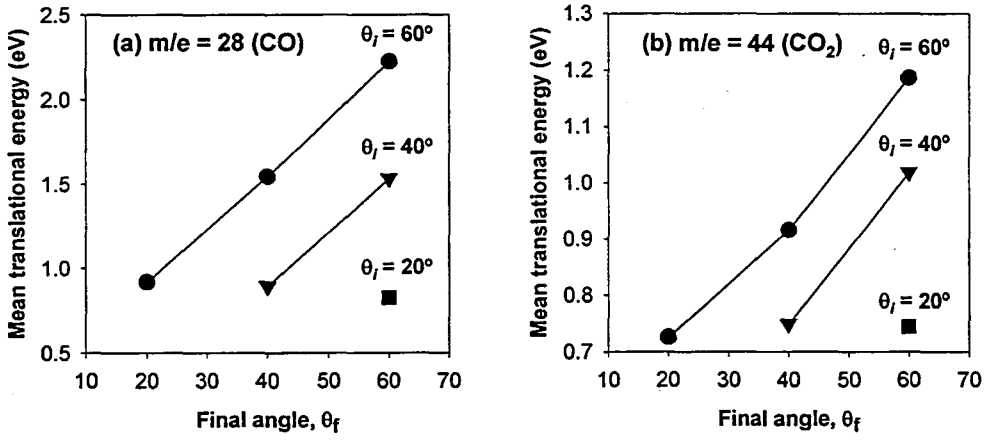

Figure 3.11 The mean translational energies of the fast components of the CO (a) and CO_2 (b) at $T_s = 300$ K.

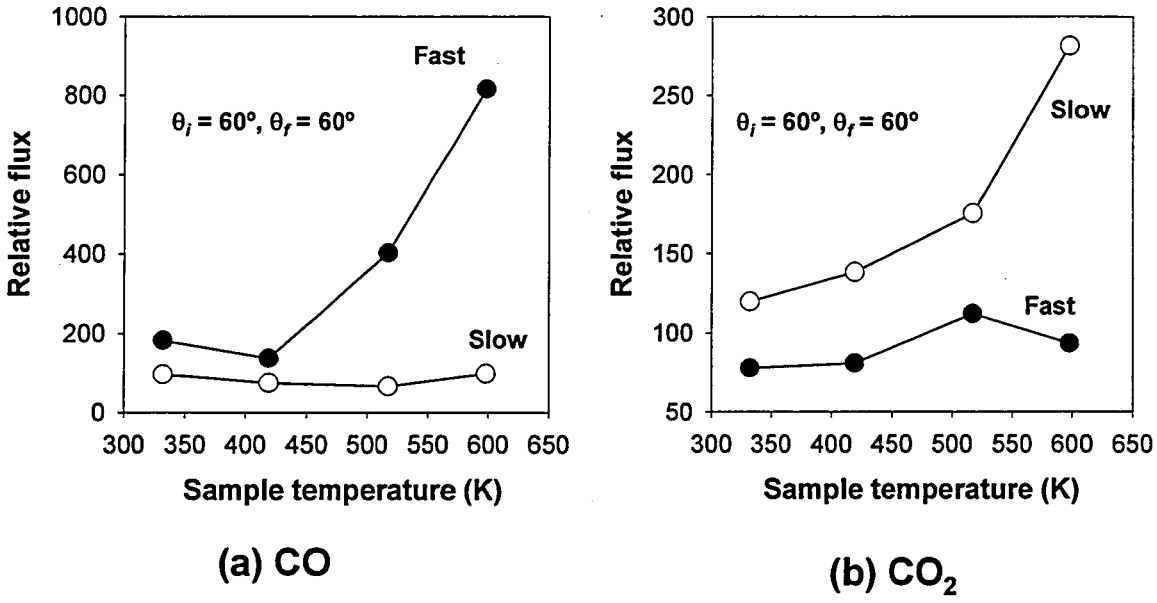

Figure 3.12 The fluxes of CO (a) and CO_2 (b) from the HOPG surface exposed to energetic beam AO at various sample temperatures.

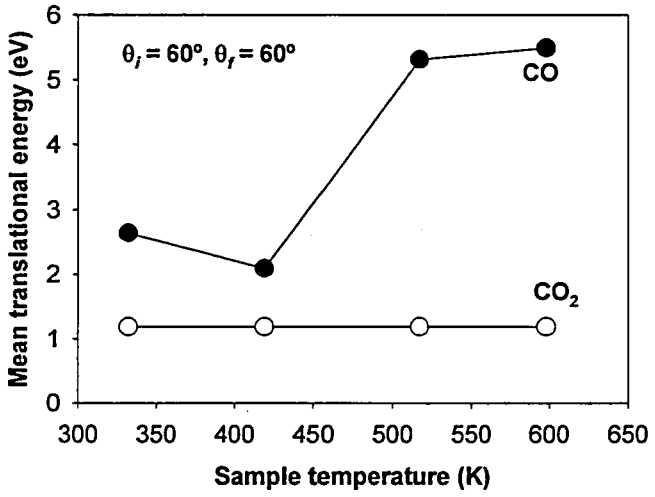

Figure 3.13 The mean translational energies of the fast components of CO and CO_2 at various sample temperatures.

temperature leads to larger flux of the slow component of CO_2, but that of the fast CO_2 component were not greatly affected by the sample temperature (Figure 3.12 (b)). The mean translational energies of the fast components of CO and CO_2 are shown in Figure 3.13 with function of the sample temperature. The mean translational energy of the fast CO_2 component keeps constant at the temperature range between 300 and 600 K, in contrast, that of the fast CO component increases with the sample temperature. From the experimental results, possible formation mechanisms of CO and CO_2 are discussed in the following section (in Section 3.4.3).

3.4.3 Removal of carbon atoms from HOPG surface

The TOF distributions of CO and CO_2 from the hyperthermal AO beam-exposed HOPG surface showed fast and slow components as shown in Figure 3.8. This fact clearly indicates the presence of at least two reaction channels with different final translational energies in the formations of CO and CO_2. It has been recognized that there are two idealized mechanisms in gas-surface reactions. One is called Langmuir-Hinschelwood (LH) mechanism[3] and the other is Eley-Rideal (ER) mechanism[3]. In the LH mechanism, incoming gas molecules are trapped at the surface with thermal equilibrium and then react with the surface atoms. In the ER mechanism, incoming reagents directly react with the surface atoms. Rettner and Auerbach have shown that these indirect and direct mechanisms can be distinguished by measuring the dynamical properties of the volatile product[3]. The direct (ER) reaction products are likely to leave from the surface with a memory of the momentum of the incident molecule. In contrast, the indirect (LH) reaction products lose such a memory because of the trapping with thermally equilibrium with the surface. In addition to the two reaction mechanisms, it is recently considered that the bombardment of high energy impinging species can play an important role in gas-surface reactions. The bombardment is likely to give sufficient energy to the reaction products adsorbed at surfaces to leave. Such process is called collision-induced desorption[9]. In the collision-induced desorption, the desorbed products might also have the memory of the momentum of the

incident molecule.

The slow components of CO and CO_2 approximately corresponded to the M-B distribution in all sample temperatures, and to cosine law. This fact implies that the slow (thermal) components do not have a memory of the incident molecule momentum. Rettner and Auerbach have pointed out that such a slow component arises from LH mechanism[3]. However, the slow components can also arise from other reaction mechanisms. For example, there is a possibility that reaction products formed by means of direct atom-surface reaction are trapped on the surface and then become thermally accommodated. From the TOF distributions, it is difficult to distinguish the slow components arise from LH mechanism and the other mechanism.

The fast components of CO and CO_2 had hyperthermal translational energies. The angular distributions of the fast (hyperthermal) components were asymmetric with respect to the surface normal and have narrow range of the angle (see Figures 3.9(a) and 3.10(a)). In addition, the final translational energy of the fast components increased at grazing collisions as shown in Figure 3.11. These results indicate that the hyperthermal CO and CO_2 components retained a memory of the incident AO. Therefore, the possible mechanisms for the formation of the fast components of CO and CO_2 might be ER mechanism and/or collision-induced desorption.

It has been reported that molecular dynamics calculation using accurate semi-empirical potential energy functions in Ar/Xe-Pt(111) system indicated that the desorption probability by means of collision-induced desorption increased with increasing surface temperature[10]. In this study, the flux of the hyperthermal CO component increased with increasing T_s and that of the hyperthermal CO_2 component unchanged. In addition to the volatile products, the formation of the surface oxide was observed on the HOPG surface during the hyperthermal AO exposure (Section 3.4.1). Therefore, the formation mechanisms of CO and CO_2 should be considered under the presence of the surface oxide in the HOPG/AO system. In particular, the surface oxide is necessary when the fast components of CO and CO_2 arise by means of collision-induced desorption. The oxygen coverage at T_s = 300 K was 0.96, and at T_s = 569 K it decreased to 0.16. This means that almost all of the incoming species were directed to the surface oxide at 300 K, in contrast they were directed to bare HOPG surface at 569 K. It can be considered that the flux of hyperthermal components decreases when the amount of the adsorbed products on surface if the volatile product desorbs

by means of the collision-induced desorption mechanism. Taking into account these considerations, collision-induced desorption might be neglect in the HOPG/AO system. It is, therefore, considered that the fast components of CO and CO_2 arisen basically from ER mechanism.

The translational energy of the hyperthermal CO component increased with increasing T_s as shown in Figure 3.13. Considering simple ER mechanisms, the large increase of translational energy with increasing T_s cannot be explained. The incoming AO directed to the graphite surface at 569 K, whereas almost all the incoming AO directed to the surface oxide at 300 K. This fact suggests that the hyperthermal CO component at 569 K came basically from the bare graphite surface, whereas at 300 K did from the surface oxide. Namely, possible reaction channels of formation of the hyperthermal CO component in this system are divided mainly into (1) O+C(bare graphite surface)→CO (mainly at higher T_s) and (2) O+C(in the oxide)→CO (mainly at lower T_s). Therefore, it is thought that the translational energy of hyperthermal CO component formed by means of the channel (1) is higher than that of the channel (2). In these two channels, the supplied energies are the translational energy of incoming AO (E_i) and the heat of reaction of each channel (E_h). The supplied energies are divided into translational (E_f), vibrational (E_v), and rotational energy (E_r) of CO, added to energy transfer to the surface (E_s). Namely, $E_i + E_h = E_f + E_v + E_r + E_s$. Therefore, the reason of the higher translational energy of hyperthermal CO component from the channel (1) than (2) may be the increase of E_h or/and the decreases of E_v, E_r, E_s. However, only E_i and E_f are known. In order to confirm this phenomenon, the knowledge of E_h, E_v, E_r, and E_s is necessary.

3.4.4 STM images at low AO fluences

The high resolution STM images of the initial HOPG (0001) surface before AO exposure showed a triangular pattern which is characteristic to graphite structure as shown in Figure 2.8 of chapter 2. The initial HOPG surface was atomically flat, and no defect was observed over several thousands of angstroms. Figures 3.14 (a) and (b) show the STM images of HOPG (0001) surfaces after exposure to the 4.7eV AO beam at T_s = 300 K with

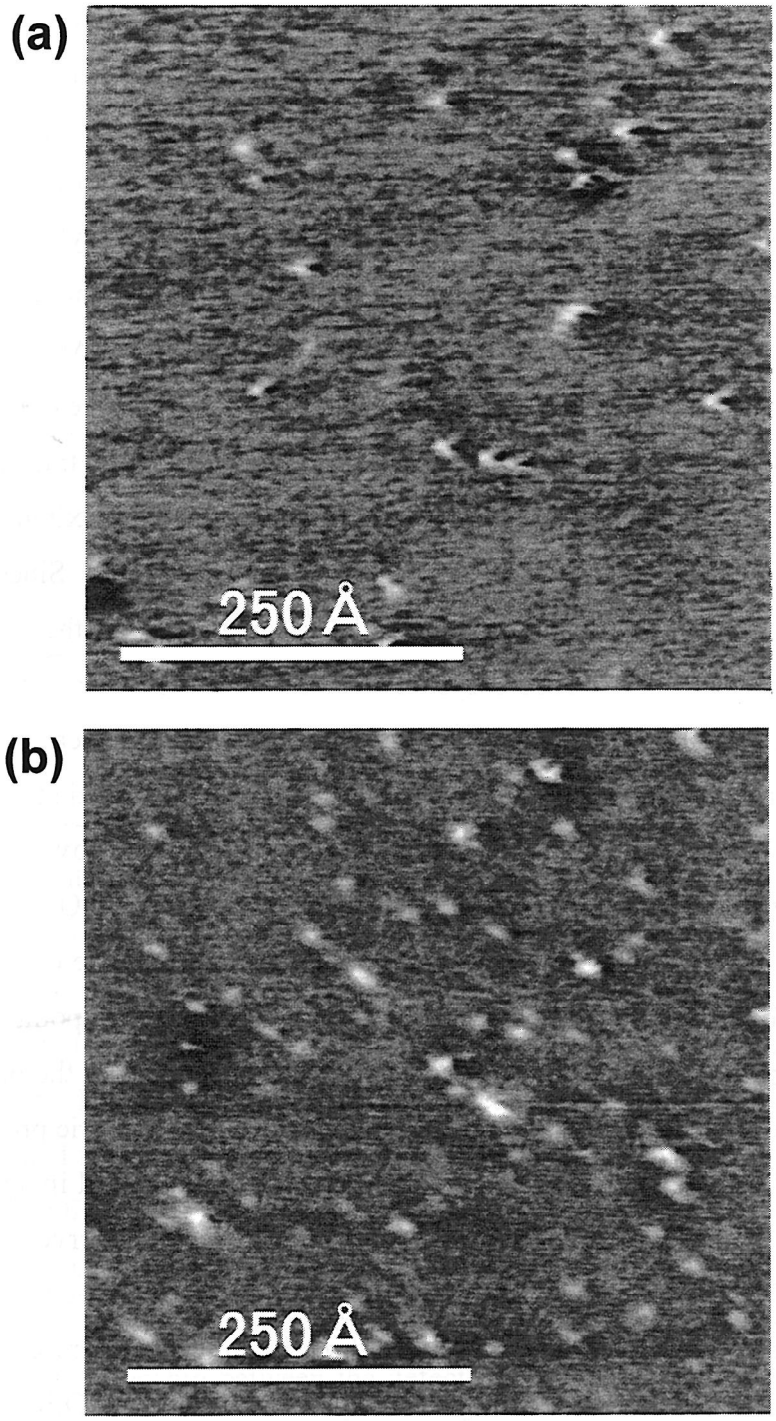

Figure 3.14 The STM images of the HOPG (0001) surfaces exposed to energetic AO beam at T_s = 300K. Scan range is 500 Å × 500 Å. (a) AO fluence of 2.1 × 10^{15} atoms/cm^2, R_{max}, R_a and R_{rms} are 7.1 Å, 0.34 Å and 0.44 Å. (b) AO fluence of 4.1 × 10^{15} atoms/cm^2, R_{max}, R_a and R_{rms} are 15.8 Å, 0.63 Å and 0.88 Å, respectively.

fluences of 2.1×10^{15} atoms/cm^2 and of 4.1×10^{15} atoms/cm^2, respectively. It is obvious from these STM images that small protrusions were formed on the surface. The typical height and diameter of the protrusions are approximately 5 and 10-15 Å, respectively. It has been reported that the STM images of the HOPG surfaces exposed to low energy ion beam show similar protrusions and they are caused by ion penetration or vacancy[11,12,13]. Moreover, it has also been reported by the AES line-shape analysis that the threshold energies of ion penetration into HOPG were 32.5±2.5 eV for Ne^+, 43.5±1.5 eV for Ar^+. The threshold energies of ion displacement of HOPG have also been reported to be 37.0 eV for Ne^+ and 47.3 eV for Ar^+, respectively[14]. These threshold energies are higher than the translational energy tails of the AO and O_2 components in the beam used in this study; the maximum translational energies of AO and O_2 in the beam were 20 eV and 23 eV, respectively. Since atomic mass of AO and O_2 are similar to those of Ne and Ar, it is concluded that the simply physical processes are neglected in the AO/HOPG system. A nature of chemistry of AO combined with a translational energy of a few eV may play significant role to this phenomenon.

One of the important points is whether or not oxygen is adsorbed at the protrusions. Since XPS is not very useful for low coverage of the surfaces (as low as 0.01), direct spectroscopic evidence of the presence of oxygen was not made at the HOPG surface where the protrusions are observed in STM image. However, the presence of oxygen can be estimated from the following reasons: (1) The STM image of the isolated point defect with an adsorbate was computer-simulated by Mizes et al.[15]. They found that the perturbation of wave function at the single defect was calculated as a three-hold symmetric protrusion with a diameter of 10-20 Å. The lateral size of the computer-simulated STM image agrees with that observed in this study, even though three-hold symmetry is not observed due to the low resolution of the STM images shown in Figure 3.14; (2) Even though the highlighted STM image reflects the high electron density, it may not directly indicate the presence of dangling bond. In the previous STM study showing similar protrusions at the HOPG surface, it was concluded that the protrusion was due to a point defect without the effect of adsorbates[13]. However, this experiment was done in air. In contrast, another STM study has reported a point defect at the HOPG (0001) as a dark spot[16]. Moreover, a computational study reported that O_2 exothermally dissociates and chemically adsorbs to a point defect at the graphite surface without any activation barrier[17]. In our experiment, the HOPG surface was

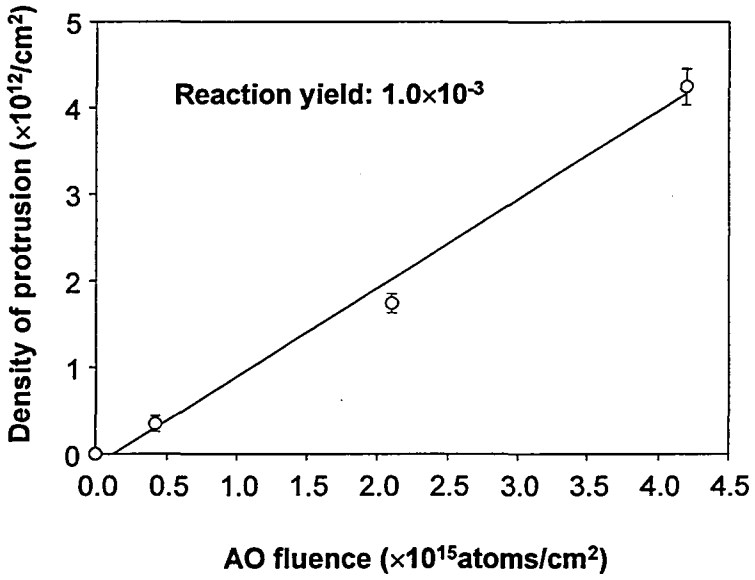

Figure 3.15 The relationship between the density of protrusion and the AO fluence. Solid line is the result of the least square method.

continuously bombarded by the energetic AO and molecular oxygen, thus, it is natural to consider that a point defect created by the direct gasification reaction were suffered by the further oxidation; (3) At the higher AO fluences, one can see the protrusions in the STM image (for example in Figure 3.16) and oxygen signal in the XPS spectrum simultaneously. From the reasons listed above, we have concluded that the protrusion appeared in the STM images originated the effect of perturbation of the charge density due to the oxygen-adsorbed defects on the HOPG (0001) surface.

It was observed that the density of protrusion was proportional to the AO fluence. Figure 3.15 shows the density of the protrusion at T_s = 300 K as a function of the AO fluence. From the linear relationship between the defect density and AO fluence indicated in Figure 3.15, the reaction yield of the hyperthermal AO with the defect-free HOPG (0001) surface was calculated by the equation below:

[reaction yield] = [density of protrusion] / [AO fluence]

The plot was fitted by the least square method, and was indicated by the solid line in Figure 3.15. From the slope of the line, the reaction yield was calculated to be 1.0×10^{-3}.

3.4.5 STM images at high AO fluences

The STM image of the HOPG (0001) surface exposed to the energetic AO beam at T_s = 300 K with the fluence of 6.0×10^{16} atoms/cm^2 is shown in Figure 3.16 (a), and its line profile of the section A-A' is indicated in Figure 3.16 (b). Different from the STM images at low AO fluences (Figures 3.15 (a) and (b)), it is obvious that whole surface was covered with protrusions. The height difference between the position labeled "B" and "C" in Figure 3.16 (b) is approximately 16 Å which is 3-4 times larger than that observed at low AO fluence.

Figures 3.17 (a) to (c) show the STM images of the HOPG (0001) surfaces exposed to the AO beam at T_s = 300 K with fluences of 3.0×10^{17}, 1.5×10^{18}, and 6.0×10^{18} atoms/cm^2, respectively. The round-shape hillock-like structure is obvious in these STM images. Figures 3.18 (a) to (c) reveal the line profiles of the A-A', B-B' and C-C' in Figures 3.17 (a) to (c), respectively. The line profiles show that the hillock-like structure consisted in flat tops and sharp valleys. It is also obvious that the diameter and the height of the hillock-like structure became large with increasing AO fluence. The XPS results indicate that the oxygen concentration at the HOPG surfaces shown in Figures 3.17 (a) to (c) are already saturated, even though the hillock-like structure is still growing. This fact suggests that the hillock-like structure was formed not by deposition of oxide, but by the hyperthermal AO induced etching reaction at the oxygen-covered surface.

Typical grain size of HOPG is reported to be a few micrometers, and the point defect density inside a grain is as low as 3 ~ 4 /μm^2 [18]. Since the diameter of the hillock-like structure is several tens of nanometer, it is not likely that the hillock-like structure is originated by the surface defects already existed before the AO exposure. In order to investigate the effect of translational energy of the AO beam on the hillock-like structure, we exposed HOPG (0001) surface to the microwave-generated oxygen plasma. A conventional microwave oxygen plasma (2.45 GHz, 250 W) was used in order to expose HOPG surface to the non-energetic AO environment. In the microwave oxygen plasma experiment, the specimen was placed 40 cm away from the plasma region, and charged species were eliminated with the grid electrode. The dominant reactive specie is considered to be AO produced by dissociation of oxygen gas. The AO generated from the microwave plasma flows to the HOPG surface through a quartz tube with 1 cm in diameter. Thus, the

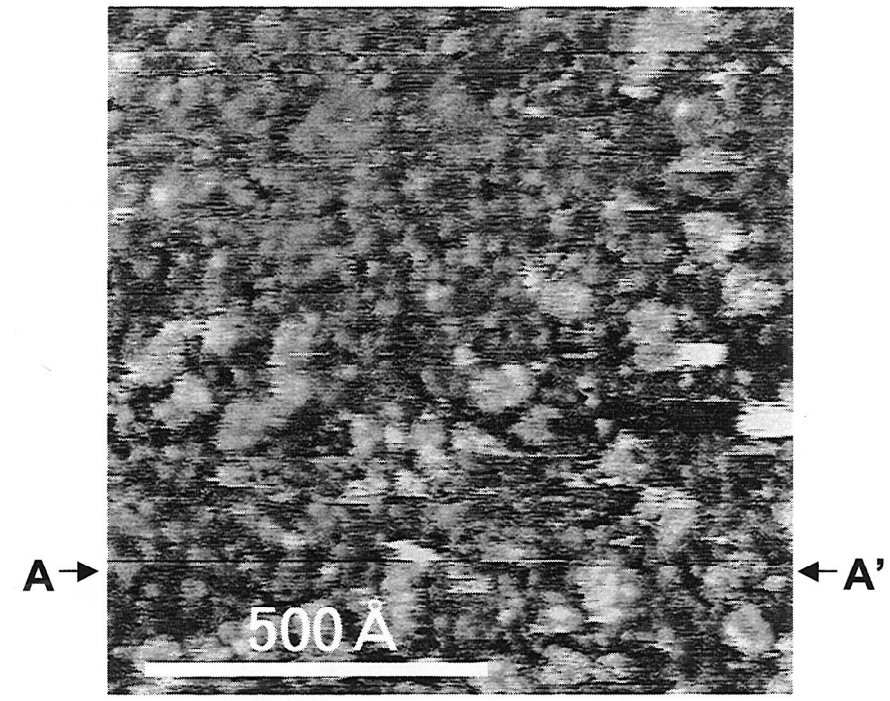

(a) STM image

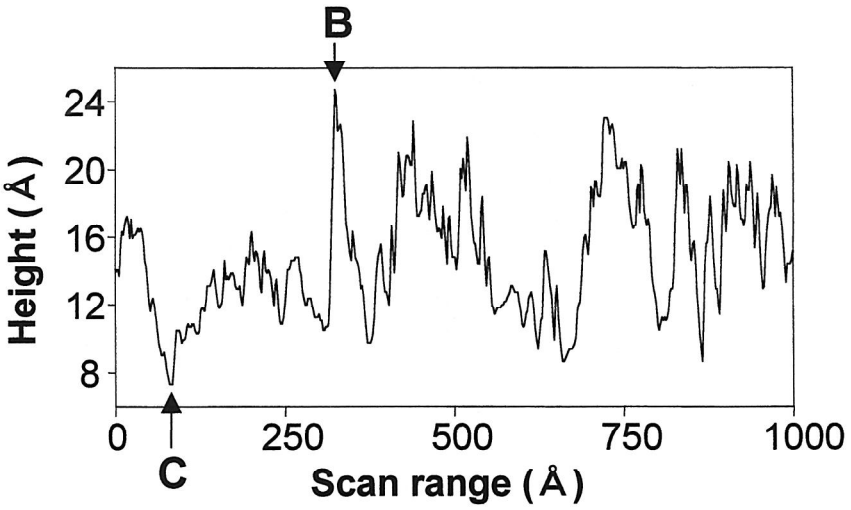

(b) Line profile

Figure 3.16 (a) The STM image of the HOPG (0001) surfaces exposed to energetic AO beam with the AO fluence of 6.0×10^{16} atoms/cm^2. The scan range is 1000 Å × 1000 Å. R_{max}, R_a and R_{rms} are 32.2 Å, 2.5 Å and 3.3 Å, respectively. (b) The line profile of the section A-A'.

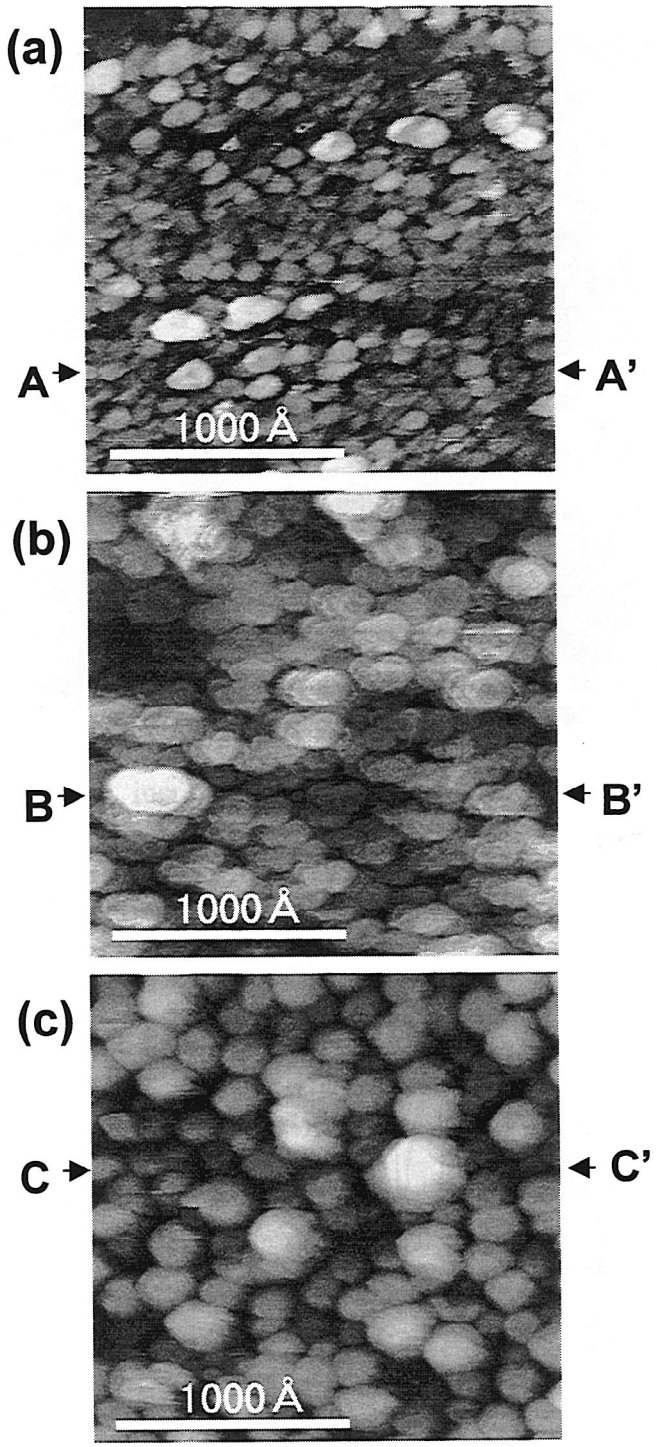

Figure 3.17 The STM images at the HOPG (0001) surfaces exposed to energetic AO beam. The scan range is 2000 Å × 2000 Å. (a) AO fluence of 3.0×10^{17} atoms/cm^2, R_{max}, R_a and R_{rms} are 37 Å, 3.5 Å and 5.0 Å. (b) AO fluence of 1.5×10^{18} atoms/cm^2, R_{max}, R_a and R_{rms} are 81 Å, 9.5 Å and 12.0 Å. (c) AO fluence of 6.0×10^{18} atoms/cm^2, R_{max}, R_a and R_{rms} are 321 Å, 30.0 Å and 37.8 Å.

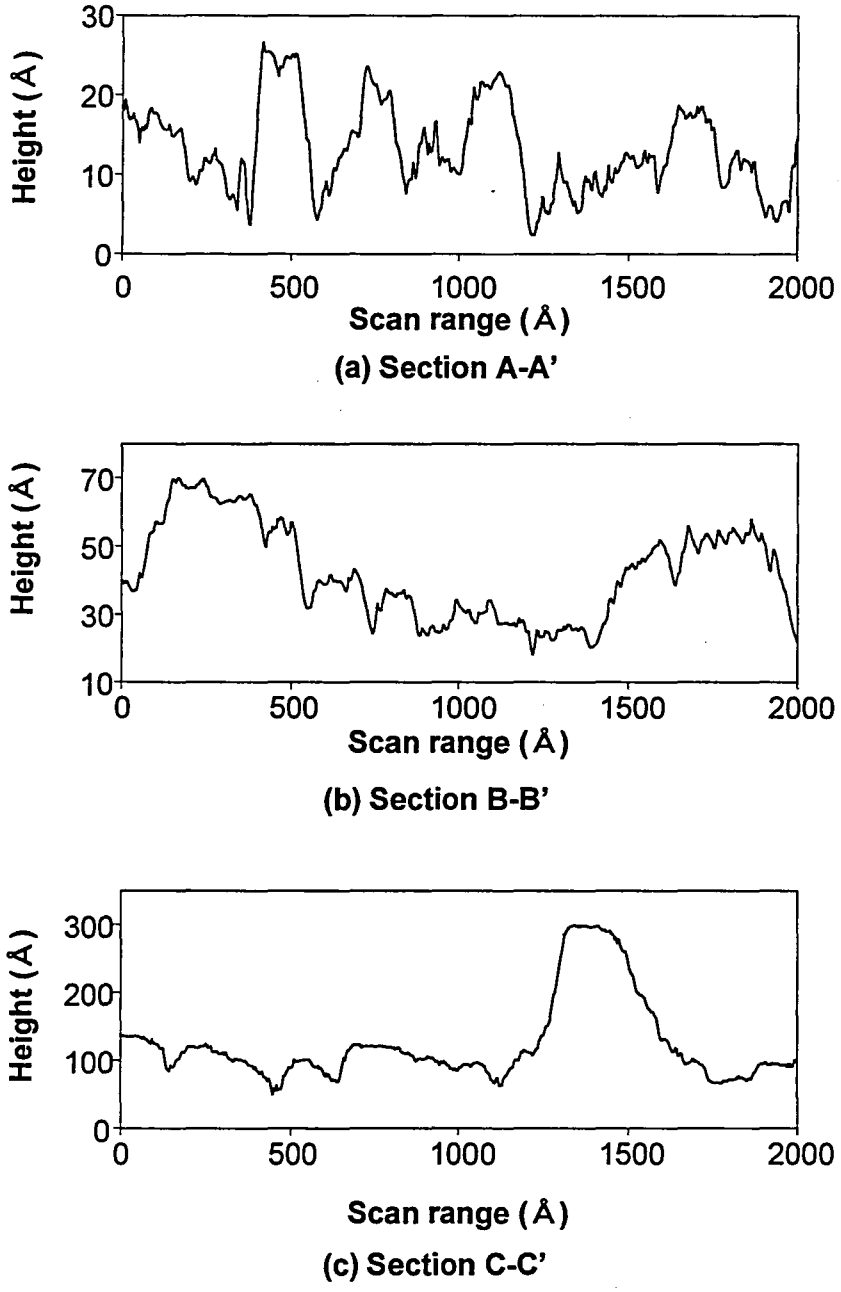

Figure 3.18 The line profiles of the sections A-A', B-B' and C-C' in Figures 3.17 (a)-(c), respectively.

AO existed in the downstream of the oxygen plasma has the M-B-type thermal velocity distribution (average energy of 0.04 eV). The AO fluence was estimated to be over 10^{20} atoms/cm^2. Figure 3.19 represents the STM image of the plasma-exposed HOPG surface at T_s = 300 K. The surface was randomly eroded and the hillock-like structure was not observed. Moreover, the surface roughnesses of the HOPG in Figure 3.19 (R_{max}, R_a and R_{rms} are 22.2 Å, 1.6 Å and 2.4 Å, respectively) were much smaller than those of the AO beam-exposed surfaces (R_{max}, R_a and R_{rms} are 321 Å, 30.0 Å and 37.8 Å, respectively, as shown in Figure 3.17 (c)). These results clearly indicate that the formation of the hillock-like structure is manly due to the high translational energy of the incident AO. In addition to the high translational energy, the hyperthermal AO beam is directional, while AO in the O_2 plasma moves randomly. As can be seen in Figures 3.6 and 3.7, the flux and the translational energy of the scattered AO become high when the incident angle is large (glazing angle of incidence). For such a grazing angle of incidence, high probability of the forward scattering is expected. When the surface was once roughed by the AO attack, the incident angle of the AO to the surface became large, and multiple bounce of AO at the surface was expected due to the high forward scattering probability. This process may be repeated until the incoming AO reacts to HOPG. The second collision will have a high angle of incidence and will show higher probability of reaction compared with the grazing angle reaction. Thus, the reaction probability at the bottom of the valley is expected to be higher than that at the top the hill. This effect cannot be expected for the non-energetic AO generated from the plasma, and it would be a part of the mechanism of the formation of the hillock-like structure observed at the energetic AO beam-exposed HOPG surface.

3.4.6 Correlation with flight experiment

The reaction yield of HOPG in LEO space environment, where bombardment of 5 eV AO took place, was reported by Ngo et al.[19]. The HOPG surface was exposed to AO environment in LEO at the altitude of 230 km for 42.25 hours on the space shuttle Atlantis (STS-46). In the flight experiment, the AO fluence was estimated to be 2.2 ~ 2.5 × 10^{20} atoms/cm^2. The surface recession due to AO-induced etching was measured from atomic force microscope (AFM). The AFM images show the hillock-like structure at the AO-

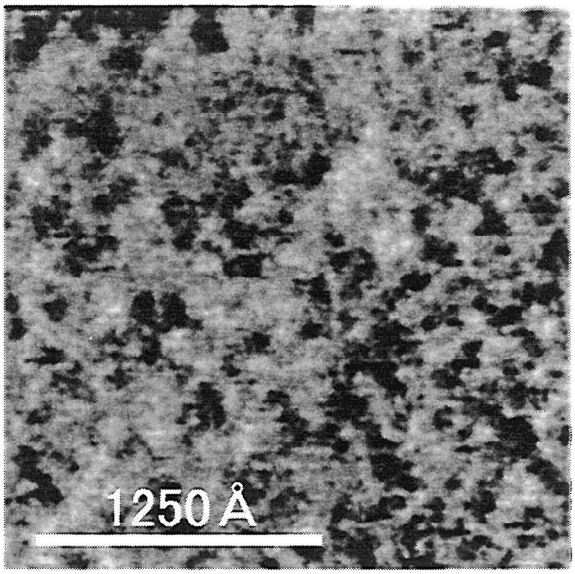

Figure 3.19 The STM image of the HOPG (0001) surface exposed to a microwave O_2 plasma. O_2 partial pressure: 270 Pa, microwave power: 250 W, exposed time 5 min. at room temperature. The scan range is 2500 Å × 2500 Å. R_{max}, R_a and R_{rms} are 22.2 Å, 1.6 Å and 2.4 Å, respectively.

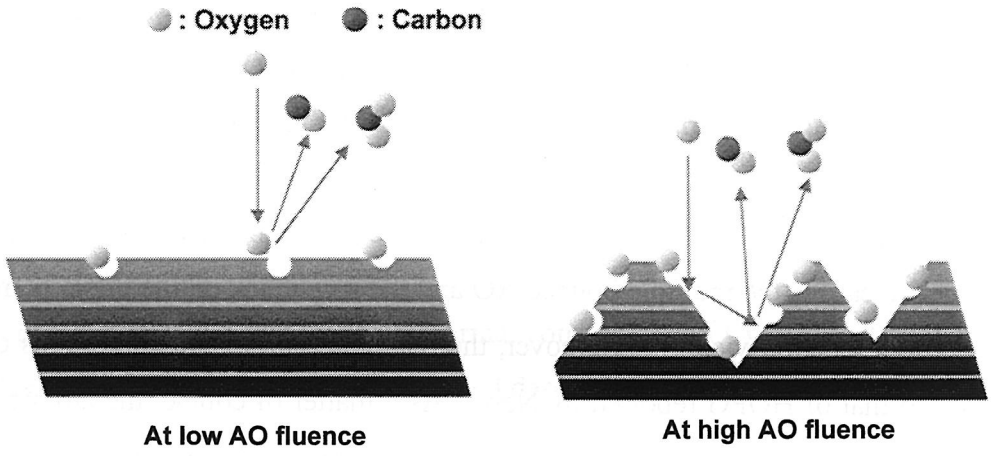

Figure 3.20 Models of AO collision with HOPG surface. At low AO fluence, hyperthermal AO is directed to the flat basal plane and only single collisions is expected. At high AO fluence, the hyperthermal AO collides with the prism planes and the multiple bounce is expected.

exposed surface which is close to those observed in this study. The recession height was approximately 2.25 μm, which corresponded to the reaction yield of 0.13. This reaction yield is two orders larger than that calculated in this study (1.0×10^{-3}). The discrepancy of these reaction yields would be explained by the following reasons (see Figure 3.20). First, the multiple bounce effect at the surface covered by hillocks increase the reaction yield of the incoming AO as mentioned above. Second, on the slope of hillocks, a number of steps of the graphite layers appeared at the surface. Therefore, a large fraction of the incoming AO collide with prism planes of HOPG when once hillock-like structure is formed at the surface. In contrast, at the initial AO exposure on the defect-free surface (where we have measured the reaction yield of AO in this study) all incoming AO encounter the basal plane. In the case of the gasification reaction of graphite with molecular oxygen, it is estimated that the activation energy along with a-axis (in the basal plane) is much lower than that with c-axis (perpendicular to the basal plane)[20]. This is the reason of forming the corrals on the basal planes in the thermal oxidation of HOPG[21]. The reaction yield of hyperthermal AO at the kink or ledge site of the graphite has not been reported, however, it will be rather close to that of amorphous carbon. In the STS-46 passive sample tray experiment, the AO-induced erosion of the carbon/carbon (C/C) composite with no graphitization treatment was evaluated[22]. It was reported that the mass loss of the specimen was 2.32 mg. Since no graphitization treatment was performed on this sample, the surface was considered to be covered by the amorphous carbon. Using the materials density (1.4 g/cm^3) and the estimated AO fluence on the flight experiment, one can calculate the reaction yield of the amorphous carbon to be 0.12. This reaction yield is two order larger than that of the basal plane of HOPG calculated in this study. It is concluded that the formation of hillock-like structure at high AO fluence causes the multiple bounce AO and the AO attack on the prism plane, which result in the high reaction yield. Moreover, the reaction yield of the amorphous carbon of 0.12 is close to that of HOPG reported by Ngo. As a matter of course, the atomic structure of amorphous carbon is quite different from that of HOPG. This shows that the reaction yield estimated in LEO is independent of its atomic structures due to the multiple bounce effect and the AO attack at the prism plane by forming the hillock-like structure.

3.5 Summary

In order to study the fundamental reaction of hyperthermal AO with carbon based materials, the chemical structure, the behaviors of the scattered molecule and reaction products, and the morphological features on the hyperthermal AO-exposed HOPG surfaces were investigated. The experimental results are summarized as follows;

1) After AO exposure, the surface oxide was obvious in the XPS spectra. The carbon atoms on the surface were bonded to an oxygen atom with single bond (bridge site) or double bond, or to two carbon atoms by single and double bonds. The oxygen coverage reached the saturated value of 0.94 at T_s = 300 K, however, decreased with increasing T_s and it reached 0.16 at T_s = 570 K.

2) The TOF distribution of the scattered AO showed the fast and the slow components that might came from direct inelastic scattering and trapping desorption, respectively. The fraction of the fast AO component in the scattered AO exceeded 80 % in many cases and its flux and the translational energy increased at grazing collisions.

3) The volatile reaction products were CO and CO_2 in which both TOF spectra include bimodal peaks. The slow components showed the Maxwell-Boltzmann distributions of velocity at all sample temperature T_s. In contrast, the mean translational energies of the fast components were far greater than kT_s. These results indicated that the desorption of CO and CO_2 has at least two reaction channels, one thermal and the other non-thermal. From the temperature dependences of the amount of oxygen accommodated on the HOPG surface, it is concluded that the hyperthermal components of CO and CO_2 may be governed by ER mechanism, not by collision-induced desorption.

4) The formation of protrusion was observed in the STM images of the AO-exposed HOPG surface at low AO fluence. This protrusion was resulted from the formation of the oxygen-adsorbed defect due to the AO exposure. The density of protrusion increased in proportion to the AO fluence. The reaction yield of hyperthermal AO with the defect-free HOPG (0001) surface was estimated to be 1.0×10^{-3}.

5) The hillock-like structure was formed on the etched surfaces at high AO fluences and the growth of the structure was observed. The formation of the hillock-like structure is due to the hyperthermal AO beam interaction with HOPG, which are high translational energy and directional. The high reaction yield observed in space was considered due to the appearance of the oxygen-covered prism planes of HOPG at the slope of hillocks, and the multi bounce effect of AO.

References

1) G. E. Caledonia, R. H. Krech, B. D. Green, "A High Flux Source of Energetic Oxygen Atoms for Material Degradation Studies," AIAA Journal, vol. 25, (1987), pp.59-63.

2) J. E. Hurst, L. Wharton, K. C. Janda, and D. J. Auerbach, "Direct inelastic scattering Ar from Pt(111)", Journal Chemcal Physic, vol. 78, (1983), pp. 1559-1581.

3) C. T. Rettner, "Reaction of an H-atom beam with Cl/Au(111): Dyamics of Concurrent Eley-Rideal and Langmuir-Hinshelwood Mechanisms," Journal Chemical. Physics, vol. 101, (1994), pp. 1529-1546.

4) B. J. Lindberg, and J. Hedman, Chemica Scripta, 7 (1975) 155.

5) M. J. Nowakowski, J. M. Vohs, and D. A. Bonnell, "Effect of sputtering and plasma etching on the surface reactivity of graphite", Journal of American Ceramic Society, vol. 76, (1993), pp. 279-278.

6) B. Marchon, W. T. Tysoe, J. Carrazza, H. Heinemann, and G. A. Somorjai, "CO and CO_2 on a graphite surface", Journal of Physical Chemistry, vol. 92, (1988), pp. 5744-5749.

7) G. Beamson and D. Breiggs, High resolution XPS of organic polymers, (John Wiley and Sons, Chichester, 1992) p. 277.

8) A. Amirav, M. J. Cardillo, P. L. Trevor, Carmay Lim, and J. C. Tully, "Atom-surface scattering dynamics at hyperthermal energies", Journal of chemical physics, vol. 87, (1987), pp. 1796-1807.

9) J. D. Beckerle, A D. Johnson, S. T. Ceyer, " Observation and mechanism of collision-induced desorption: CH_4 on Ni(111)", Physical Review Letters, vol. 62, (1989). pp. 685-688.

10) D. Kulginov, M. Persson, C. T. Rettner, "Dynamics of collision-induced desorption: Ar-Xe/Pt(111)", Journal of chemical physics, vol. 106, (1997), pp. 3370-3386.

11) G. M. Shedd, and P. E. Russell, "The effects of low-energy ion impacts on graphite observed by scanning tunneling microscopy", Journal of Vacuum Science Technology, A9, (1991), pp. 1261-1264.

12) D. Marton, H. Bu, K. J. Boyd, S. S. Todorov, A. H. Al-Bayati, and J. W. Rabalais, "On the deffect structure due to low energy ion bombardment of graphite", Surface Science, vol. 326, (1995), pp L489-L493.

13) J. R. Hahn, H. King, S. Song, and I. C. Jeon, "Observation of change enhancement induced by graphite atomic vacancy: A comparative STM and AFM study", Physical Review B, vol. 53, (1996), R1725-R1728.

14) D. Marton, K. J. Boyd, T. Lytle, and J. W. Rabalais, "Near-threshold ion-induced defect production in graphite", Physical Review B, vol.48, (1993), pp. 6757-6766.

15) H. A. Mizes and J. S. Foster, "Long-Range Electronic Perturbations Caused by Defects Using Scanning Tunneling Microscopy", Science, vol. 244, (1989), pp. 559-562.

16) S. Kondo, M. Lutwyche and Y. Wada, "Observation of threefold symmetry image due to a point defect on a graphite surface using scanning tunneling microscopy (STM)", Japanese Journal of Applied Physics part 2, vol. 33, (1994), L1342-L1344.

17) S. M. Lee, Y. H. Lee, Y. G. Hwang, J. R. Hahn, and H. Kang, "Defect-induced oxidation of graphite", Physical Review Letter, vol. 82, (1999), pp. 217-220.

18) X. Chu and L.D. Schmidt, "Reaction of NO, O_2, H_2O, and CO_2 with the basal plane of graphite, "Surface Science, vol. 268, (1992), pp. 325-332.

19) T. Ngo, E. J. Snyder, W. M. Tong, R. S. Williams, M. S. Anderson, "O atom etching of graphite in low earth orbit", Surface Science, vol. 314, (1994), L817-L822.

20) This was experimentally observed when HOPG is oxidized in a oxygen gas at high temperature. A circular pit with monolayer depth is observed on HOPG [18].

21) D. L. Patrick, V. J Cee., T. P.Beebe Jr., ""Molecular Corrals" for studies of Monolayer Organic Films", Science, vol. 265, (1994). 231-234.

22) E. Brinza, S.Y. Chung, T.K. Mintion, R.H. Liang, Final Report on the NASA/JPL Evaluation of Oxygen Interactions with Materials-3 (EOIM-3) (JPL Publication 94-31, Pasadena, 1994).

Chapter 4

Reaction of hyperthermal atomic oxygen with polyimide films

Abstract

The translational energy dependence and the fluence dependence of hyperthermal AO reactivity with pyromellitic-dianhydride (PMDA) oxydianiline (ODA) polyimide films were investigated. Mass change of the PMDA-ODA polyimide film was measured by QCM during AO beam exposures. *In-situ* XPS measurement was carried out in order to obtain chemical information of the AO-exposed PMDA-ODA polyimide surface. The experimental results showed that the mass loss and the change in chemical structure of the PMDA-ODA polyimide film were caused by a low flux AO beam exposure with the translational energies higher than 30 eV. This effect was considered to be resulted from the physical process such as sputtering. The PMDA-ODA polyimide film which was exposed to 4.7 eV AO beam showed the mass gain due to oxygen adsorption in the beginning of the reaction and then the steady-state mass loss followed. The experimental results of the mass change was fitted by the computational model, in which the carbon abstraction rate at the oxygen-adsorbed sites was higher than that at the unoxidized polyimide surface without being oxidized. The computational result indicated that a large fraction of carbon abstraction reaction occurred in the oxygen-adsorbed site. Moreover, the effect of ambient air exposure to the AO-exposed polyimide surface was also investigated. It was clearly demonstrated that the ambient air exposure affected surface chemistry of the AO-exposed polyimide surface.

4.1 Introduction

Kapton-H (DuPont) is one of the most widely used polyimide in aerospace application because of its thermal stability, heat capacity, thermal conductivity, and heat

resistance. Metallized Kapton-H films, in which Kapton-H film is transparent in the solar wavelength region and the back surface of the film is coated with reflecting opaque metal such as sliver and aluminum, are used as passive thermal control material in many spacecraft. It has been widely known that Kapton-H film is eroded by the hyperthermal AO bombardment in LEO environment, and Kapton-H is one of the reference materials to evaluate the other material's erosion rate[1], and its erosion in space environment has been studied intensively. However, due primary to the complicated chemical structure of Kapton-H, the reaction mechanism of Kapton-H with hyperthermal AO has not been established yet.

The survivability of materials in space environment is rated by the reaction efficiency (*Re*)[2]. *Re* is usually calculated by the following equation;

$$Re = [\text{mass loss}]/[\text{material density}]/[\text{AO fluence}] \quad (1).$$

It has been reported that *Re* of Kapton-H film with hyperthermal AO is over two orders greater than that with thermal AO[3]. Moreover, a "needle-like" surface structure is observed only on the energetic AO-exposed Kapton-H surface[4]. Such a surface structure resembles under the physical sputtering processes[3]. However, the AO translational energy of 5 eV is considered to be much lower than the common threshold energy required for a physical sputtering process. In order to clarify this point, many researchers have investigated of the translational energy dependence of AO interaction with Katpon-H[3]. However, it was not very successful because of the difficulty of adjusting AO beam energy in the wide range, i. e., powerlike, steplike and squarelike relations of *Re* with translational energy were reported. These results were obtained using high AO flux sources such as supersonic nozzle beam-type sources or laser-induced breakdown-type source. However, capability for adjusting translational energy of the AO beam is relatively low, thus *Re* measurement in the wide range of translational energy cannot be achieved with these AO sources. In contrast, even though AO flux generated by an ion beam-type AO source is lower than the other two methods, translational energy can be tunable by changing applied voltage of the anode in the ionizer. Thus, ion beam-type AO source has an advantage for adjusting translational energy of the beam over a wide range.

Recent study in the reactive scattering of hyperthermal AO with saturated hydrocarbon polymers showed that only OH and H_2O are the reactive products from a

continuously refreshed liquid squalane, whereas CO and CO_2 are produced from solid polypropylene[5]. These experimental results clearly showed that CO and CO_2 formation occurs only when oxygen atoms adsorb on the surface, i. e., the formation of the volatile carbon-containing species resulting in mass loss is the secondly reaction. For the ion beam-type AO source, it is difficult to generate AO with a fluence of 10^{15} atoms/cm^2 that corresponds to approximately 1 monolayer. Therefore, using the ion beam-type AO source provides the initial AO reaction without the influence of adsorbed oxygen. In contrast, laser detonation-type AO source forms a high flux AO beam and it is expected to see the difference in reaction with AO fluence by using these two AO sources.

Another point of interest on AO reaction with polyimide is the effect of air exposure before the analyses. The surface analysis of Kapton-H film had always been carried out only after AO exposure in the previous studies, i. e., the sample surface was exposed to ambient air before the analyses. Surface analyses of the AO-exposed materials may be affected by contamination from ambient air. The polyimide surfaces before AO exposure may be chemically inactive, however, such inactive surfaces may be oxidized and/or excited by AO attacks. If such excited surfaces are exposed to ambient air, it is natural to consider that adsorption and/or relaxation would occur, and the original properties of the AO-exposed surface may be lost. It has actually been reported by Sengupta et al. that the surface composition and chemical structure of the physical sputtered polyimide film is changed due to moisture adsorption after ambient air exposure[6]. Therefore, in order to obtain precise data, the *in-situ* experiment is mandatory.

In this chapter, the translational energy dependence of *Re* of PMDA-ODA polyimide film is measured using the ion beam-type AO source, and analysis of its AO fluence dependence was carried out using the laser detonation-type AO source. Mass change of the PMDA-ODA polyimide film exposed to AO beam was recorded during the AO exposure using QCM. The carbon abstraction mechanism of polyimide film caused by hyperthermal AO exposure will be discussed. Later in this chapter, the effect of ambient air exposure on the polyimide was investigated. The change in oxygen content and the chemical states of the carbon atoms at the AO-exposed polyimide surface due to ambient air exposure was analyzed by XPS.

4.2 Experiments

Two types of AO sources were used in this study. One was the ion beam-type AO source for analyzing translational energy dependence. The other was the laser detonation-type AO source used mainly for the experiment on AO fluence dependence. The details of these AO sources were described in chapter 2. The translational energy of AO beam generated by the ion beam-type AO source was tunable from 1 eV to 50 eV, and that from the laser detonation-type AO source was typically 4.7 eV (see Figure 2.12 (a) in chapter 2). The incident angle of the beam was 0° (direction of the surface normal) for both facilities.

Many researchers have studied mass change of polyimide film, however the measurement of mass has been carried out by the post process[7,8]. Generally, the detection of mass change faces the difficulty due to the absorption of moisture from atmosphere. A highly sensitive *in-situ* mass measurement is required to satisfy the purpose of the present work. QCM is one of the methods which satisfies the requirements. However, conventional Kapton-H film is too thick to apply to QCM because of the narrow dynamic range of the mass measurement. Therefore, spin-coated polyimide film was used for the mass measurement with QCM. A polyimide amide acid (Toray, Semicofine SP-510) was spin-coated on a quartz crystal at 12,000 rpm for 30 s, and the curing treatments at 150 °C for 1 hr. and 300 °C for 1 hr. were carried out in order to form the spin-coated polyimide structure with a thickness of approximately 0.1 μm. The spin-coated polyimide film formed and Kapton-H film have the same repeating unit of polymer. The temperature of the QCM sensor was maintained at 38 °C ±0.1 °C by the temperature-controlled recirculator during the experiments. *Re* of the spin-coated polyimide film was calculated, assuming that the material density is 1.42 g/cm^3, which corresponds to that of Kapton-H. Conventional Kapton-H was also used for the experiment on the effect of air exposure. Kapton-H films were cleaned by dipping into deionized water, ethanol, and ethylether. The cleaning process was repeated 3 times.

The XPS measurements of the polyimide film exposed to AO generated by the laser detonation-type AO source can be carried out without ambient air exposure. However, the measurements of the sample exposed to AO beam generated by ion beam-type AO were carried out after ambient air exposure.

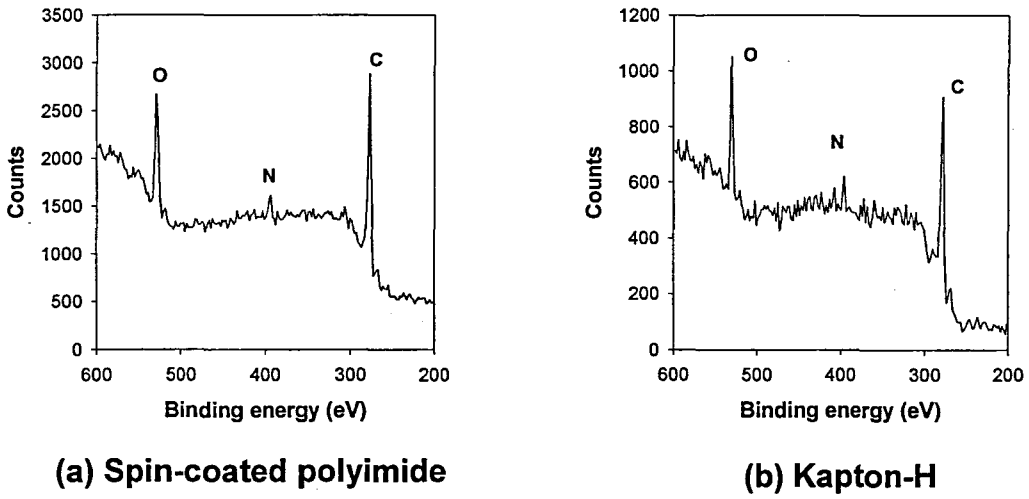

Figure 4.1 XPS survey spectra of the spin-coated polyimide film (a) and the Kapton-H (b). The atomic percent of carbon, oxygen, nitrogen of the polyimide film are 76 %, 19 % and 5 %, respectively, and these of Kapton-H film are 75 %, 17 % and 8 %, respectively.

4.3 Method of XPS analysis

Figure 4.1 shows the XPS survey spectra of a spin-coated polyimide film and a Kapton-H before AO exposure. The composition of the films were calculated with the relative peak areas of the C1s, O1s and N1s peaks in the XPS spectra of the films with relative photoionization cross sections for MgKα X-ray ($I_{O1s} : I_{C1s} : I_{N1s} = 1.00 : 2.85 : 1.77$). Table 4.1 displays the compositions of two films. The atomic percents of C, O, N at the spin-coated film surface were calculated to be 76 %, 19 % and 5 %, and those in Kapton-H film were 75 %, 17 % and 8 %, respectively. It was confirmed that the atomic concentration of the spin-coated polyimide is close to that of the Kapton-H film.

XPS measurements were also carried out in order to obtain chemical information of the AO-exposed polyimide surfaces. Some theoretical and experimental work has been carried out for analyzing polyimide films with XPS. Silverman et al. reported the results of molecular orbital calculation of polyimide structure[9,10,11]. According to their calculation,

Table 4.1 The composition of the films calculated from relative peak areas of the C1s, O1s and N1s peaks in XPS spectra.

		Atomic percent (%)		
		C	O	N
Spin-coated polyimide	pristine	76	19	5
	*after 5eV AO exposure	56	40	4
Kapton-H	pristine	75	17	8
	*after 5eV AO exposure	63	29	8
	*after 5eV AO exposure with 220 day air exposure	69	23	8

*The AO fluence of 8.5×10^{17} atoms/cm^2.

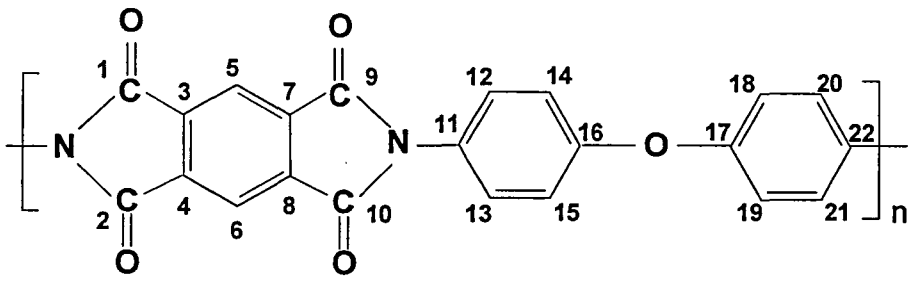

Figure 4.2 Atomic structure of PMDA-ODA polyimide film. The semicofine (SP-510) and Kapton-H have the same repeating unit of polymer. The assignment numbers of carbon atoms are used for decomvolution of XPS spectra.

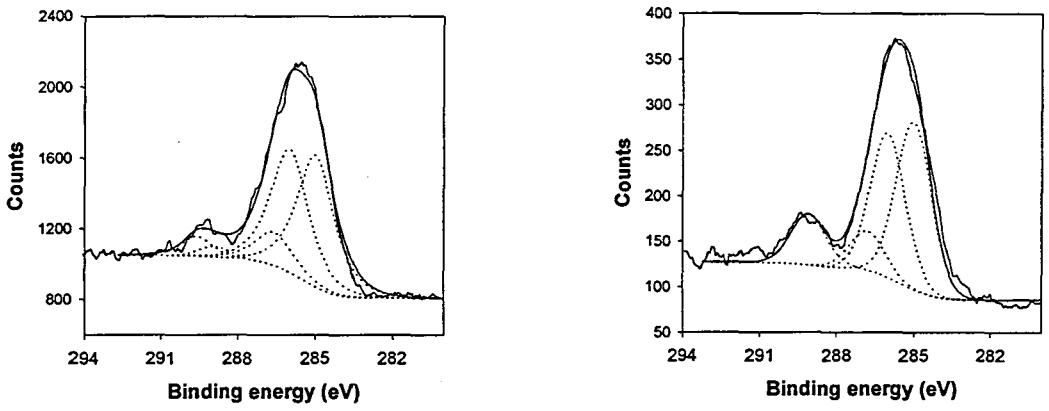

(a) Spin-coated polyimide **(b) Kapton-H**

Figure 4.3 High-resolution C1s XPS spectra of the spin-coated polyimide film (a) and the Kapton-H film (b).

maximum energy shift of C1s binding energy was calculated to be 4.2 eV and it agreed well with the experimental results. However, two carbon atoms which bond to nitrogen atoms have different energy shifts, i. e., 0.14 and 1.28 eV, even though these two carbon atoms have the same structure. Experimental work on the same carbon atoms measured the energy shift of 0.9 eV[12]. The energy shifts of 1.1 to 1.3 eV of the same carbon atom also were reported in the other reference[13]. Bachman et al. used 1.3 eV for the energy shift on these carbon atoms[14]. Considering the facts mentions above, the energy shift of 1.28 eV for the carbon atoms bonded with nitrogen in polyimide structure seems to be reasonable. In this study we used our own protocol for peak synthesis of XPS. This is based on the experimental data reported by Briggs[12] and on the theoretical results by Silverman[9]. Figure 4.2 shows atomic structure of PMDA-ODA polyimide film. The semicofine (SP-510) and Kapton-H have the same repeating unit of polymer. The signals from eight carbon atoms consisting of ODA (C12, C13, C14, C15, C18, C19, C20, C21) appear at 285.0 eV; six carbon atoms consisting of PMDA (C3, C4, C5, C6, C7, C8) and two carbon atoms bonded to nitrogen (C11, C22)

Table 4.2 XPS peak synthesis results of the C1s XPS spectra.

	Peak position (eV)	285.0	286.0	286.6	287.7	288.9	289.6
	Assignments	ODA	PMDA	C-O-C	-C(=O)-H	-C(=O)-N	-C(=O)-OH
		Atomic percent (%)					
Spin-coated polyimide	pristine	46	39	8	0	5	2
	after 5eV AO exposure	46	22	12	5	12	2
	after 50eV AO exposure	37	29	16	11	5	1
Kapton-H	pristine	42	36	10	0	13	0
	after 5eV AO exposure	46	22	5	13	16	0
	after 50eV AO exposure with 220 day air exposure	46	28	5	4	16	0

at 286.0 eV; carbons in the C-O-C structure (C16, C17) at 286.6 eV; and carbon atoms with carbonyl group bonded with benzene ring and nitrogen (C1, C2, C9, C10) at 288.9 eV. In the case of the AO-exposed polyimide, additional peaks at around 287.5 eV and 290 eV often are found. Therefore, we synthesized two additional peaks at 287.7 eV (carbonyl group bonded to benzene ring and hydrogen) and at 289.6 eV (carbonyl group bonded to benzene ring and OH, namely carboxyl group). All of these peaks were synthesized by 20% Gaussian - 80 % Lorentzian distributions with FWHM of 1.7 eV and no asymmetric parameter was used. The background was subtracted with the Shirley's method. Figure 4.3 shows the deconvoluted XPS spectra of the spin-coated polyimide film (a) and Kapton-H film (b). The result of peak deconvolution is represented in Table 4.2. An error in the fraction of each oxidation state of carbon was estimated to be in the order of a few percent. It was estimated that the spin-coated polyimide film contains a small amount of carboxyl group (2%).

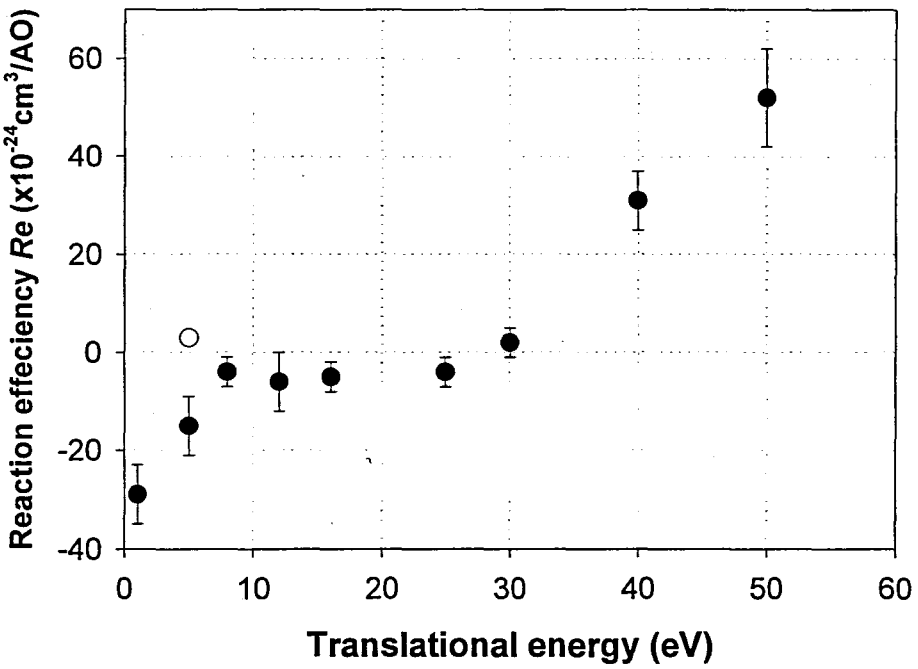

Figure 4.4 Translational energy dependence of the reaction effiiciencies (*Re*) of AO with spin-coated polyimide films. The filled circles indicate the experimental results and the open circle shows the *Re* of 3.0×10^{-24} cm^3/atom, which is widely recognized as *Re* of Kapton-H film in the LEO environment.

4.4 Results and discussion

4.4.1 Translational energy dependence

Figure 4.4 shows the relationship between *Re* and translational energy of AO beam. *Re* was measured from the frequency shift of QCM during the AO exposure using the ion beam-type AO source. Translational energy and *Re* were calculated from the anode voltage in the ionizer and the frequency shift of the spin-coated QCM, respectively. The AO

fluences in the range of 10^{15} atoms/cm^2, which is the maximum AO fluence can be generated by the ion beam-type AO source, corresponds to 1 monolayer, therefore, the data reflect the initial stage of AO reaction with the PMDA-ODA polyimide. The filled circles indicate the experimental results and the open circle shows the *Re* of 3.0×10^{-24} cm^3/atom, which is widely recognized as *Re* of Kapton-H film in the LEO environment. As shown in Figure 4.4, *Re* shows negative values (mass gain) at the translational energies of lower than 30 eV, whereas mass loss was observed in the higher translational energies. The *Re* at the translational energy lower than 5 eV shows significant mass increase. The AO-exposed polyimide usually shows mass loss except for the JPL Scatterometer experiment flown on EOIM-3[15]. The mass loss data were obtained by the flight tests[1] and by ground tests using laser induced breakdown systems[16], molecular beam systems[17] or plasma ashers[18]. All these experiments were done in high flux AO beam (or plasma), that is at least 2 ~ 3 orders of magnitude greater than the present work. Thus, it was identified that the initial stage of reaction is different from the steady-state reaction which oxygen atoms already adsorb on the polyimide surfaces. This mass increase observed here is considered due to the higher stacking (adsorption) probability of hyperthermal AO on the polyimide surface at low translational energies. As for the significant mass loss at higher translational energies, Chernik reported similar behavior of *Re* with the magnetoplasmadynamic accelerator for AO testing[19]. He reported *Re* of 38×10^{-24} cm^3/atom at AO exposure with translational energy of 35 eV. This result seems to agree with the data shown here.

Figure 4.5 shows the XPS survey spectrum of the spin-coated polyimide film after exposure to 4.7 eV AO beam with AO fluence of 8.5×10^{17} atoms/cm^2 using the laser detonation-type AO source without ambient air exposure. After the hyperthermal AO exposure the atomic percentages of C, O, and N are 56 %, 40 %, and 4 %, respectively (see Table 4.1). Figure 4.6 indicates C1s core level XPS spectrum of the same sample of Figure 4.5. The peak synthesis results of the XPS spectrum shown in Figure 4.6 are summarized in Table 4.2. One can find in Table 4.2 that the peak at 286.6, 287.7, and 288.9 eV increases due to the exposure of 4.7 eV AO beam, whereas, the peak at 285.0 eV is stable and the peak at 286.0 eV decreases. The peak at 285.0 eV comes from the benzene ring in ODA, and the peaks at 286.0 eV from that in PMDA. The results of XPS analysis can be interpreted that

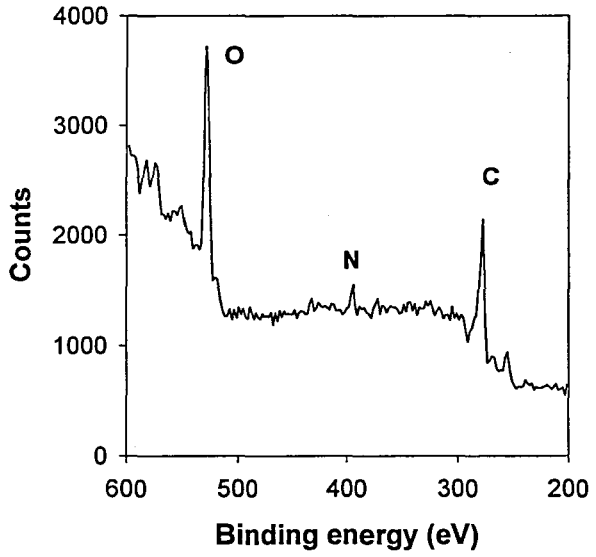

Figure 4.5 XPS survey spectrum of the spin-coated polyimide film after exposure to 4.7 eV AO beam with the AO fluence of 8.5×10^{17} atoms/cm^2. The atomic percent of carbon, oxygen, nitrogen were 56 %, 40 % and 4 %, respectively

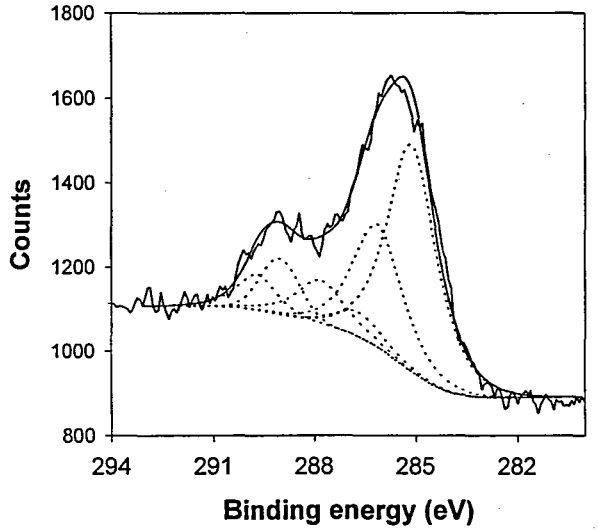

Figure 4.6 High-resolution C1s XPS spectrum of the spin-coated polyimide film after exposure to 4.7 eV AO beam with the AO fluence of 8.5×10^{17} atoms/cm^2.

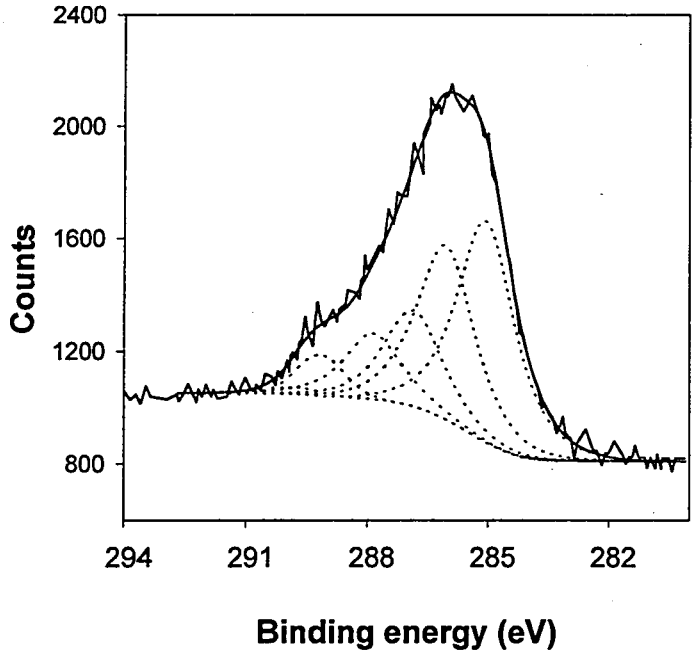

Figure 4.7 C1s XPS spectrum of the spin-coated polyimide film exposed to AO beam with translational energy of 50 eV.

5 eV AO chemically adsorbs to the carbon atoms in PMDA and that these carbon atoms show the chemical shift of C1s peak from 286.0 eV to 288.9eV. Analytical results of the polyimide sample (Ube, Upilex) exposed to AO by the EOIM-3 mission indicated that breaking of the chain of polyimide structure at C-N bond in PMDA[20]. Reactive scattering data from was the ^{13}C-enriched polyimide, in which ODA was composed of ^{13}C and PMDA was composed of ^{12}C, exposed to hyperthermal AO beam showed that ^{12}CO and $^{12}CO_2$ were larger than those in ^{13}CO and $^{13}CO_2$, i. e., volatile products were formed mainly at PMDA[21]. The XPS spectral analysis shown here agrees with these experimental results.

The C1s XPS spectrum obtained from the spin-coated polyimide exposed to 50 eV AO beam is shown in Figure 4.7 and its peak synthesis results are summarized in Table 4.2. The sample was exposed to ambient air before the analysis. As shown in Table 4.2, both ODA and PMDA decreased in the XPS spectrum, whereas the signal from C-O-C and carbonyl increased. These results clearly showed that the degradation of polyimide occurs with less structural dependence in the case of 50 eV AO beam exposure. The XPS spectra

obtained from PMDA-ODA polyimide surfaces sputtered by 0.5 - 2 keV Ar^+ ion have also shown the decreases both PMDA and ODA and the increase of the peak at 287.9 eV that corresponds to amide group[6]. This XPS result is similar to our result shown above. Moreover, the change in the XPS spectrum of the Ar^+-sputtered PMDA-ODA polyimide maintained even after 72 hours of air exposure. Therefore, the XPS measurements of the 50 eV AO-exposed sample also might not be affected from the air exposure. The threshold energy of physical sputtering depends on the mass of the incident ions (atoms) and of the substrate. The threshold energy of the physical sputtering of AO/polyimide system is not clear; the threshold energy of physical sputtering of C^+ against graphite, which seems to be close to AO/polyimide system, is reported to be 44 eV[3]. Therefore, AO attack with translational energy of 50 eV is considered to exceed the threshold energy of physical sputtering. It is, therefore, concluded that the chemical reaction with AO at PMDA is the major reaction path for the materials degradation at the translational energies lower than 30 eV, however, the physical sputtering becomes dominant at the translational energies higher than 50 eV.

4.4.2 Fluence dependence

The AO fluence dependence on mass loss phenomenon was investigated using the laser detonation-type AO source. Figure 4.8 displays the surface composition of the spin-coated polyimide film as a function of the AO fluence. Note that those XPS measurements were carried out without ambient air exposure. It is clear from Figure 4.8 that the amount of N is not affected by AO exposure. However, the O increases and the C decreases with increasing the AO fluence, and then they reached the saturated value of approximately 55% and 40 %, respectively, at the AO fluence of over 2×10^{17} atoms/cm^2. This result indicates that the surface oxide increases with AO fluence and reaches the saturate value at the AO fluence of 2×10^{17} atoms/cm^2.

Any mass change was not detected when the film was exposed to thermal O_2 beam. In contrast, significant mass change was observed during the AO beam exposure. Figure 4.9 indicates the result on *in-situ* measurement of the mass change of the spin-coated polyimide

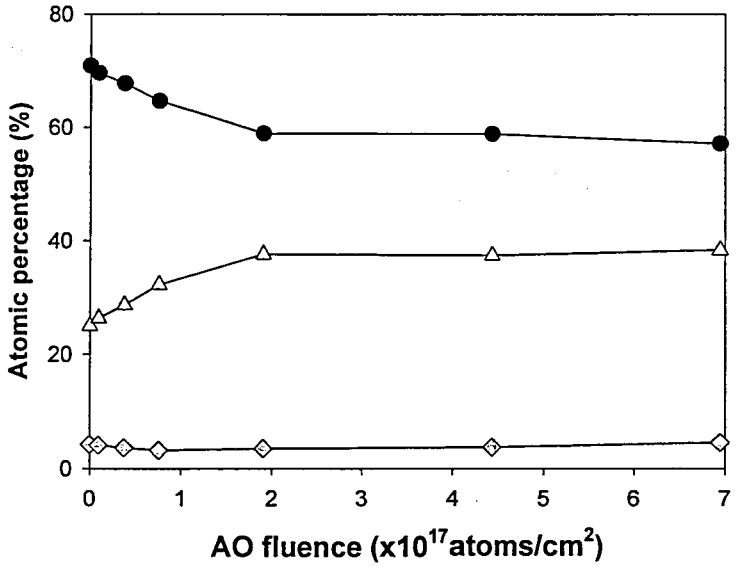

Figure 4.8 The composition of the polyimide film exposed to AO beam as a function of AO fluence.

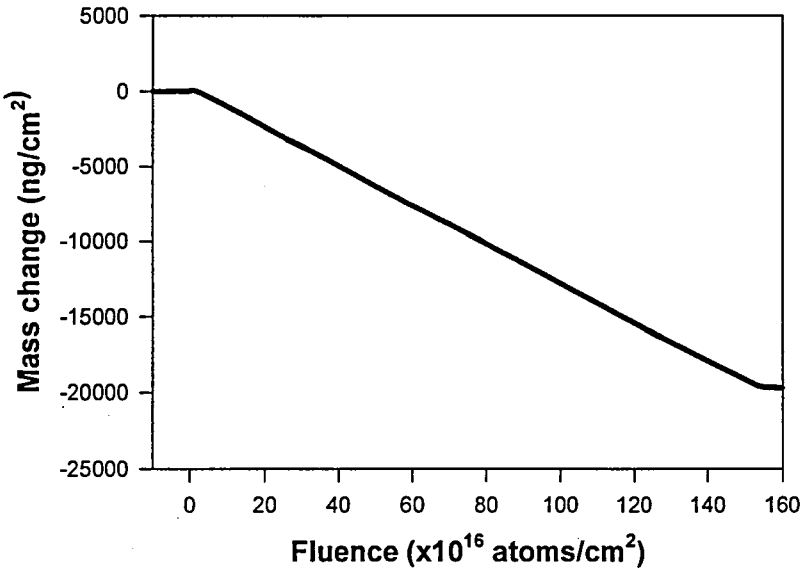

Figure 4.9 The mass change of the polyimde film exposed to AO with the translational energy of 4.7 eV and the flux of 3.1×10^{14} atoms/cm^2/s.

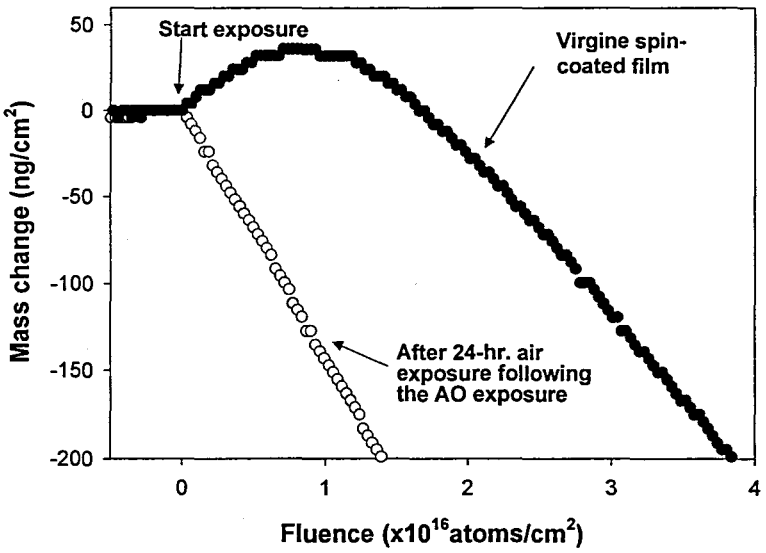

Figure 4.10 The mass change of the polyimde films exposed to hyperthermal AO beam at the beginning of AO exposure. Close-up view of the beginning of AO exposure shown in Figure 4.9

film during the 4.7 eV AO beam exposure. The AO fluence in Figure 4.9 is approximately three orders larger than those in Figure 4.4. As can be seen in Figure 4.9, the mass of the film decreases with proportional to the AO fluence. The *Re* of AO with the spin-coated polyimide film was calculated to be 7.0 - 8.8 × 10^{24} cm^3/atom from the slope of the graph. Not only the steady-state mass loss, but also the mass gain at the beginning of the reaction was observed in Figure 4.9. Figure 4.10 shows the mass gain of the spin-coated polyimide as a function the AO fluence at the beginning of the exposure. The filled circles show the mass change of the virgin spin-coated polyimide film. The mass of the virgin spin-coated polyimide film increased first and then started decreasing. The steady-state decrease was observed at the AO fluences higher than 2 × 10^{16} atoms/cm^2. The mass increase is considered to be due to the oxygen adsorption. Based on this assumption, a reference experiment was carried out. Namely, the AO exposure to spin-coated polyimide was stopped at the AO fluence of 3. 2 × 10^{18} atoms/cm^2, and the surface was exposed to ambient

air for 24 hours. The surface, thus prepared, was already oxidized with this AO fluence (see Figure 4.8), and AO beam exposure was conducted on this surface. The open circles in Figure 4.10 indicate the mass change of the oxidized spin-coated polyimide often restarting the AO exposure. As is clearly seen in Figure 4.10, the mass gain was not observed in the oxidized spin-coated polyimide film and the rate of mass loss immediately became steady-state. From the result of this reference experiment, the role of adsorbed oxygen in the mass loss phenomenon was clear. The adsorption probability (Ra)[22] of AO on the spin-coated polyimide surface was estimated to be 0.31 from the initial slope of the mass increase. Even when the steady-state mass loss was established with AO fluences over 2×10^{16} atoms/cm^2, the surface composition had not yet reached the reach steady-state; surface oxygen content reached its steady-state value with AO fluence of 2×10^{17} atoms/cm^2. Considering the attenuation length and inelastic mean free path of photoelectrons in the XPS measurement, the outmost surface was considered to be oxidized at the AO fluence of 2×10^{16} atoms/cm^2, and the AO diffusion into the polyimide resulted in further increase of oxygen composition in XPS data.

The Re of 7.0 - 8.8 $\times 10^{24}$ cm^3/AO was calculated from the steady-state mass loss in Figure 4.9. This is more than two times larger than that observed in LEO (3.0×10^{-24} cm^3/atom). The reason of the discrepancy of these Re is undoubtedly complex because many factors should be considered. The possible explanations of the discrepancy are described by the following;

1) Oxygen concentration

XPS measurement of the spin-coated film and Kapton-H revealed the similarity of their structures, however, difference in composition was especially for the AO-exposed surface. The atomic percentage of C, O, and N of the spin-coated polyimide film before exposure were, 76 %, 19 % and 5 %, whereas those at Kapton-H film were 75 %, 17 % and 8 %, respectively. The compositions of C, O, and N of the spin-coated polyimide film and Kapton-H film in the AO exposure with the fluences greater than 2×10^{17} atoms/cm^2 were approximately 55%, 40 %, 5%, and 63 %, 30 %, and 7 %, respectively. The oxygen concentration of the spin-coated polyimide film in the steady-state oxidized surface is 10 % larger than that of the Kapton film. The experimental results show the importance of

adsorbed oxygen at the major gasification reaction of polyimide. The difference in the fraction of surface oxygen adsorable may cause high *Re* of the spin-coated films.

2) Measurement of AO flux

In the space environmental effect community, the erosion rate of polyimide film is a standard for measuring AO flux[1]. However, in this study, the flux of AO beam was measured using QCM with silver electrodes (Section 2.1.3). The reaction and accommodation probabilities of AO at the silver surface were assumed to be 1.0 in this calculation. Thus, the flux calculated by QCM is a lower bound of the AO flux. Even though the reaction and accommodation coefficient of AO with silver surface was reported to be almost 1.0[23], if the reaction and accommodation probabilities are lower than 1.0 in practice, *Re* in this study may be overestimated.

3) Collision-induced desorption

It was reported that CO and CO_2 were formed on Kapton-H surface only using the thermal AO beam alone, while hyperthermal argon beam (translational energy covering the range 2.5 - 17eV) with thermal AO beam leads to larger CO_2 signal than that by thermal AO beam alone[24]. This experimental result clearly shows the presence of a collision-induced production in the material (carbon) removal process, and it enhances the mass loss rate. This suggests that the carbon removal rate may be induced by collision-induced desorption. In our experiment, there are the presence of high translational energy component O_2 as well as AO is confirmed. In the LEO environment, there is high energy N_2 (9 eV) component and the fraction of N_2/AO is less than 0.1 (depending on the altitude). The fraction of the hyperthermal components of O_2/AO in our beam is approximately 0.7. Therefore, the high reactivity in our experiment may be contributed by the collision-induced desorption caused by the hyperthermal O_2 component in the beam.

The mass change observed in the spin-coated QCM was computer-simulated. A number of reaction paths can be considered in the real system, however, it is too complicate to take into account every reaction. Thus, we divided all reactions into two groups; one occurs at clean polyimide surface, the other dose at oxidized surface. Direct reaction of AO with polyimide to form CO and that of O_2 to form CO_2 is in the former reaction group. In

contrast, many of reactions including trapping desorption of CO and CO_2, collision-induced desorption of CO and CO_2 are categorized in the later group. Here, we define the nomenclature. θ is the oxygen coverage, $P_{CL}(C)$ and $P_{CL}(O)$ are the probabilities that O and C atoms in the polyimide structure remove from the clean polyimide surface due to AO attack, $P_{OX}(C)$ and $P_{OX}(O)$ are the probabilities that O and C atoms in the polyimide structure remove from the oxidized surface due to AO attack, $P_{DE}(O)$ is the probability that the adsorbed O atoms desorb from the oxidized surface due to AO attack, $P_{AD}(O)$ is the probability that the impinging AO adsorbs to the clean polyimide surface, F the AO flux, S the number of adsorption site at the polyimide surface, and M_O and M_C the mass of oxygen and carbon. The contributions of nitrogen and hydrogen to the mass change was neglected due to its low density and low mass. Macroscopically, the fraction of carbon and oxygen contributes to the mass loss is the same of atomic content in the polyimide structure, when surface oxidation reached steady-state in the AO attack. Thus, the ratio of $P_{CL}(C) / P_{CL}(O)$ *and* $P_{OX}(C) / P_{OX}(O)$ are considered to be 4.4 (=22/5, i.e., ratio in number of carbon and of oxygen in the repeating unit of polyimide).

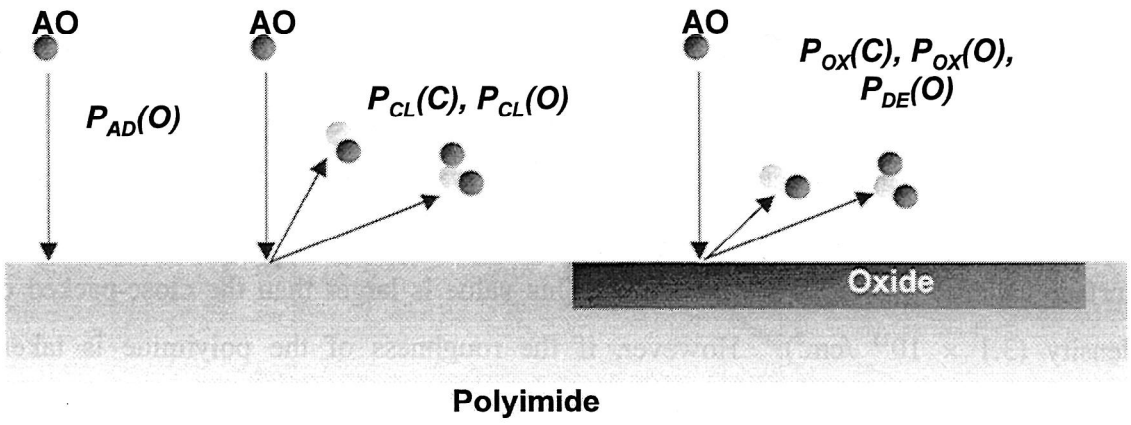

Figure 4.11 The model of the carbon abstraction at the AO-exposed polyimde surface, in which the carbon abstraction rate at the oxygen-adsorbed sites is different from that at the oxidized polyimde surface without being oxidized.

Using the variables and assumption described above, mass change between each AO shot (ΔM) was expressed in the following equation:

$$\Delta M = P_{AD}(O)\, F(1-\theta)SM_O - P_{CL}(O)\, F(1-\theta)S(4.4M_C + M_O) - P_{OX}(O)\, F\theta S(4.4M_C + M_O) - P_{DE}(O)\, F\theta SM_O \quad (1)$$

The equation (1) shows the balance of attaching and detaching carbon and oxygen atoms during the AO beam bombardment.

The calculation was carried out under the known F (3.1×10^{14} AO/cm^2/shot), M_O (16 AMU) and M_C (12 AMU), and the unknown S, $P_{AD}(O)$, $P_{CL}(O)$, $P_{OX}(O)$, and $P_{DE}(O)$ parameters. The θ was computed repeatedly in every shot. The best fit curve to the experimental data shown in Figure 4.10 was obtained with the following parameters.

$S = 8.5 \times 10^{15}$ /cm^2,
$P_{AD}(O) = 5.0 \times 10^{-17}$ cm^2,
$P_{CL}(O) = 2.8 \times 10^{-19}$ cm^2,
$P_{OX}(O) = 2.3 \times 10^{-17}$ cm^2,
$P_{DE}(O) = 6.9 \times 10^{-17}$ cm^2.

The fitting results were demonstrated in Figure 4.12. It is clearly indicated that the model described the carbon abstraction phenomenon very well. The validity of this calculation was confirmed from the calculated parameters. (1) Number of adsorption site at polyimide surface calculated was 8.5 x 10^{15} /cm^2. This value is larger than the close-packed carbon density (3.1×10^{15} /cm^2). However, if the roughness of the polyimide is taken into consideration, this value would be acceptable. (2) Initial adsorption yield (fraction of adsorbed AO in the AO flux) was expressed as to be $FP_{AD}(O)$ in this model, and is calculated to be 0.42. On the other hand, the adsorption yield calculated from the slope of the very initial mass increase is 0.31. Both values were close each other. In the computational result, it was shown that $P_{OX}(O)$ was two orders magnitude greater than $P_{CL}(O)$. This result suggests that the major reaction path of carrying the mass away from the surface occurs at the

oxidized polyimide surface. When $P_{OX}(O)$ was assumed to be equal to $P_{CL}(O)$ in the computer simulation, the computer simulated result was far from the experimental result. This computational result implied the importance of adsorbed oxygen in the major gasification reaction of polyimide.

Minton and co-workers recently reported the experimental results using TOF mass spectrometer[24,25]. They found that no CO and CO_2 were detected when continuously refreshed hydrocarbon surfaces were exposed to hyperthermal AO beam. In contrast, they detected CO and CO_2 signals from the AO-exposed polymer surfaces such as Kapton-H. They also reported that large CO and CO_2 signals were detected when high energy (>9 eV) argon or oxygen beam attacked at Kapton-H surface under continuous bombardment with thermal AO generated by the diffusive radio frequency AO source. Since the addition of the thermal AO leads to the increase oxygen concentration on the surface, the large CO and CO_2 signals is considered due to the increase of adsorbed oxygen on the surface. In conjunction with the experimental data reported by Minton and co-workers, the computer-simulated QCM data strongly suggests the role of adsorbed oxygen in the major reaction path of the CO/CO_2 removal from the surface.

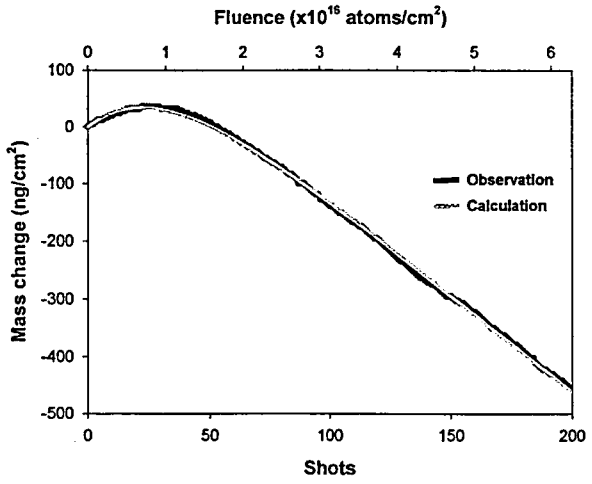

Figure 4.12 Comparison of the computational result with the experimental result. The solid line indicates the experimental results shown in Figure 4.10 and the gray line shows the fitting results using the computational model shown in Figure 4.11.

4.4.3 Effect of air exposure

The surface analysis of Kapton-H film exposed to AO in previous studies has always been carried out only after ambient air exposure. In order to investigate the effect of ambient air exposure on the AO-exposed Kapton-H film, change in the chemical structure and surface composition at the AO-exposed Kapton-H due to ambient air exposure was analyzed by XPS.

Figure 4.13 displays the composition of the Kapton-H film as a function of the AO fluence. All XPS measurements were carried out without ambient air exposure. The atomic percent of C, O, and N at Kapton-H film before exposure (pristine surface) was 75 %, 17 % and 8 %, respectively. The amount of N is relatively independence of the AO exposure. However, the oxygen increases and the carbon decreases with increasing the AO fluence, and then they reached the saturated value of approximately 63 % and 30 %, respectively, at the AO fluence of over 2×10^{17} atoms/cm^2. This result indicates that the surface oxide of the Kapton-H film increases and reaches the saturated value. These

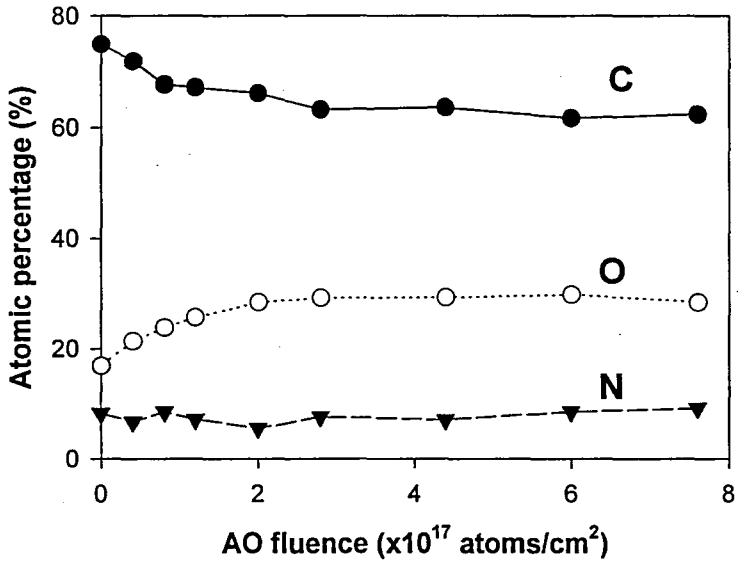

Figure 4.13 The composition of the Kapton-H film exposed to AO beam as a function of the AO fluence. The measurements were carried out without air exposure.

experimental results obtained by Kapton-H were consistent with those of the spin-coated films shown in Figure 4.8. The AO-exposed Kapton-H film with the AO fluence of 8.5 × 10^{17} atoms/cm^2 was stored in the Teflon container under the environment of clean air of the class 10,000. The time history of the composition of the AO-exposed Kapton-H film under the air exposure is shown in Figure 4.14. It is obvious that N is relatively stable, whereas the atomic percents of C increases and that of O decreases. The composition after 220 days of air exposure are summarized in Table 4.1. Figure 4.15 indicates the C1s XPS spectra of the AO-exposed Kapton-H film with the AO fluence of 8.5 × 10^{17} atoms/cm^2 without air exposure (a) and with air exposure of 220 days (b). The peak synthesis results are summarized in Table 4.2. The decrease in carbonyl peak (287.7 eV) due to air exposure is remarkable. This result suggests that the recoveries of C and O were due to the decrease of carbonyl group in the polyamide film. Sengupta et al. have reported that the surface composition and chemical structure of the physical sputtered polyimide film is changed due to moisture adsorption after ambient air exposure[6]. The experimental results showed that the O/C ratio in the PMDA-ODA polyimide film decreased by the physical sputtering, however, it recovers by the air exposure of 72 hours. Furthermore, long-term compositional changes due to ambient air exposure for a number of polymer surfaces after the argon plasma treatments have been reported[26]. These compositional changes arise from the reaction between O_2 and/or water in air and the radical sites formed by the argon plasma treatments, i. e., oxidative degradation reaction. The reaction continues over many months and the O/C ratio of the polymers increased gradually and reached saturated values. These results are opposite from our result. It is considered that the high oxygen (O/C = 0.5) concentration in the AO-exposed Katpon-H film with the AO fluence of 8.5 × 10^{17} atoms/cm^2 may be unstable. Therefore, after air exposure, in order to become to be stable, the saturated oxygen may diffuse into the film and/or desorb by forming volatile products. In contrast, the plasma treatment reported previously did not include the oxidant in the plasma and only the oxidation reaction with oxidants in air have been studied.

In addition, the compositions of the AO-exposed Kapton-H films with various AO fluence were analyzed after ambient air exposure. The result was shown in the filled symbols with the solid lines in Figure 4.16. The open symbols with the dotted lines in Figure 4.16 indicate the results of the AO-exposed Kapton film without air expose (same as

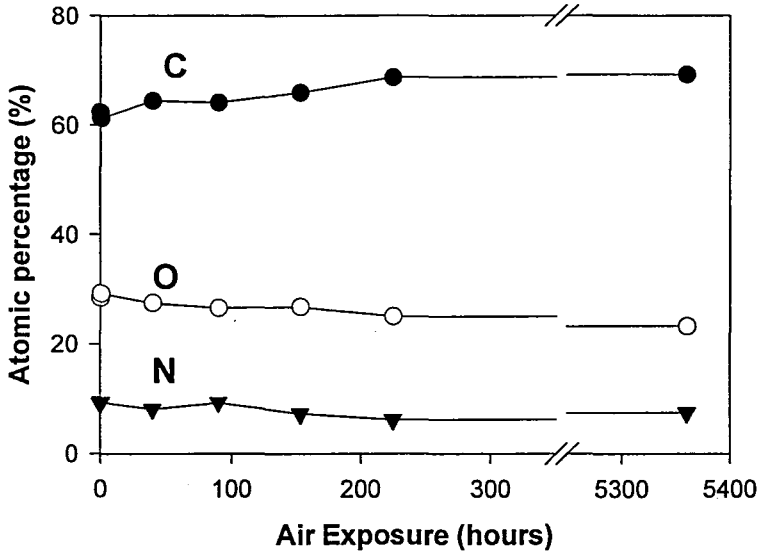

Figure 4.14 Time history of the composition of the AO-exposed Kapton-H film under air exposure. The sample was stored in the Teflon container under the environment of clean air of the class 10,000.

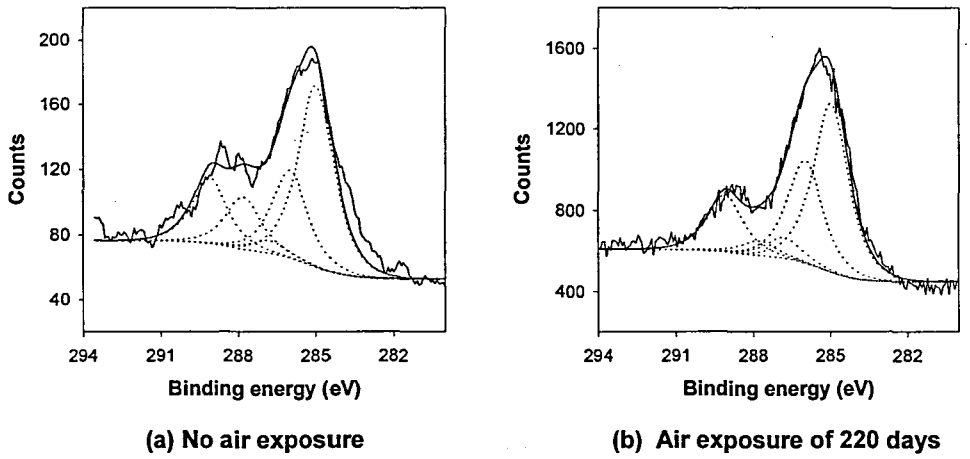

Figure 4.15 High-resolution C1s XPS spectra of the AO-exposed Kapton-H film with the AO fluence of 8.5×10^{17} atoms/cm^2 before air exposure (a) and after air exposure of 220 days (b).

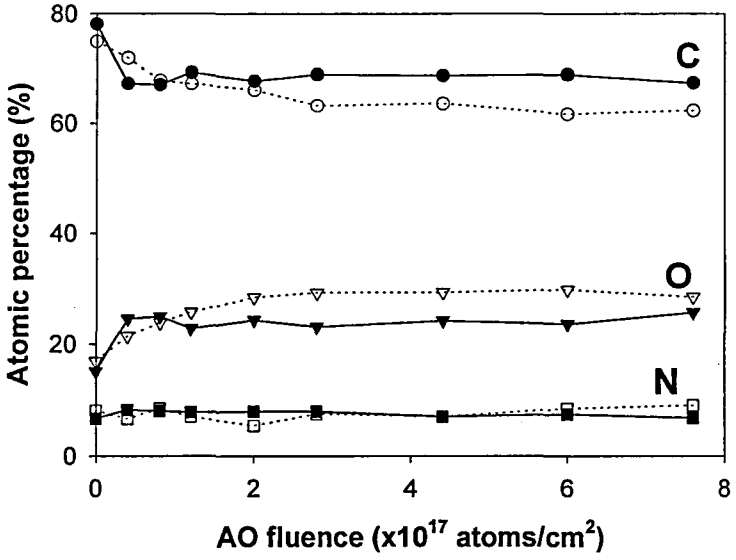

Figure 4.16 The composition of the AO-exposed Kapton-H film as a function of the AO fluence. The filled symbols with the solid lines show the compositions of the AO-exposed Kapton-H films which were analyzed after ambient air exposure. The open symbols with the dotted lines indicate the results without air expose (same as that in Figure 4.13).

that in Figure 4.13). It is obvious that the atomic percent of C and O with ambient air exposure rapidly reached the saturated values of 66 % and 25 %, respectively. This result clearly shows that the experimental data of XPS are affected by air exposure. The oxygen concentration measured with air exposure is larger than that without air exposure at the AO fluence smaller than 1×10^{17} atoms/cm^2. But it is smaller than the AO concentraion at the AO fluence of 1×10^{17} atoms/cm^2. The saturated values of C and O in the AO-exposed Kapton-H film with air exposure are close to those of the sample stored in 220 days in ambient air (69%, 23%). Thus, these atomic percentages (69% for C, 23% for O) are considered to be the steady-state value of AO-exposed Kapton-H films in ambient air. It is, therefore, considered thatthe radical sites formed by the AO-exposure may react with in-air species (O_2 and/or water) when the oxygen concentration is smaller than the steady-state

value, whereas, the saturated oxygen may diffuse into the film and/or desorb when the oxygen concentration is larger than the steady-state value. These experimental results clearly show to investigate the surface chemical states of the materials in LEO environment. The necessity of carrying out the *in-situ* analysis of the AO-exposed sample.

4.5 Summary

In this chapter, AO translational energy dependence and AO fluence dependence of the AO reaction with the PMDA-ODA polyimide films were investigated. The results of this chapter are summarized as follows;

1) The mass loss and dominant structural change of the spin-coated polyimide film was observed at the translational energies above 30 eV. This is due to the physical sputtering under the low flux AO beam exposure. In contrast with the transnational energies below 30 eV, the XPS spectra showed that ODA structure is relatively insensitive to the AO exposure and oxygen adsorption was observed (mainly on PMDA structure).

2) The spin-coated polyimide film exposed to 4.7 eV AO showed mass gain due to the oxygen adsorption at the beginning of the reaction, and follows the mass loss with proportional to AO fluence. This result suggested that the mass loss (carbon abstraction) at high AO fluence is subsequently reaction after oxygen is being adsorbed on the surface.

3) The computer-simulated QCM data strongly suggested that the great fraction of carbon abstraction (mass loss) occurs in the oxygen-adsorbed surface (desorption rate is two orders of larger than that at the clean polyimide surface). In conjunction with the experimental data reported by Minton et al., the computer-simulated QCM data strongly suggested the role of adsorbed oxygen in the reaction path.

4) The *Re* of 7.0 - 8.8 $\times$ 10^{24} cm^3/AO calculated from our experiment is more than two times

larger than that in LEO (*Re* of 3.0 × 10^{24} cm^3/AO). The possible explanations of the discrepancy are the difference in oxygen concentration, the measurement method of AO flux, and the presence of collision-induced desorption.

5) The experimental results on the effect of ambient air exposure clearly showed that the atomic percentage of the AO-exposed polyimide film after ambient air exposure reached steady-state value (about 65 % for C, 25 % for O, and 10 % for N). These values were influenced by air exposure. This may be because the radical sites formed by the AO-exposure may react with in-air species (O_2 and/or water) when the oxygen concentration is smaller than the steady-state value, whereas, the saturated oxygen may diffuse into the film and/or desorb when the oxygen concentration is larger than the steady-state value. These results clearly show that *in-situ* analysis for the AO-exposed sample is necessary to study the surface chemical state of the material in LEO.

References

1) M. R. Reddy, "Review Effect of Low Earth Orbit Atomic Oxygen on Spacecraft Materials", Journal of Materials Science, vol. 30, (1995), pp. 281-307.

2) Reaction efficiency (Re) is defined by the average volume that is removed by a single O-atom attack. Unit is [cm^3/atom].

3) Z. A. Iskanderova, J. I.Kleiman, Y. I. Gudimienko, R. C. Tennyson, "Influence of content and structure of hydrocarbon polymers on erosion by atomic oxygen", Journal of Spacecraft and Rockets, vol. 32, (1995), pp. 878-884.

4) J. L. Whitton, "Experimental studies of morphology development", Erosion and Growth of Solids Stimulated by Atom and Ion beams, edited by G. Kiriakidiz,G. Carter, and J. L. Whitton, Martinez Nijhoff, (1986).

5) D. J. Garton, T. K. Minton, M. Alagia, N. Balucani, P. Casavecchia, G. G. Volpi, "Reactive scattering of ground-state and electronically excited oxygen atoms on a liquid hydrocarbon surface", AIAA Paper No.97-3947, (1997).

6) K. S. Sengupta and H. K. Birnbaum, "Structural and chemical effects of low energy ion bombardment of PMDA-ODA surfaces", Journal of Vacuum Science Technology, A9, vol. 6, (1991), pp. 2928-2935.

7) L. J. Leger, "Oxygen atom reaction with shuttle materials at orbital altitudes --Data and experiment status", AIAA paper 83-0073, (1983).

8) D. G. Zimcik and C. R. Maag, "Results of apparent atomic oxygen reactions with space materials during shuttle flight STS-41G", Journal of Spacecrafts and Rockets, vol. 25, (1988), pp. 162-168

9) B. D. Silverman, P. N. Sanda, P. S. Ho, A. R. Rossi, "Origin of the carbon 1s-core level shifts in polyimide model compounds", Journal Polymer Science, vol. 23, (1985), pp. 2857-2863.

10) B. D. Silverman, J. W. Bartha, J. G. Clabes, P. S. Ho, A. R. Rossi," Molecular orbital analysis of the XPS spectra of PMDA-ODA polyimide and its polyamic acid precursor", Journal Polymer Science, A24, (1986), pp. 3325-3333.

11) L. P. Buchwalter, B. D. Silverman, L. Witt, A. R. Rossi," X-ray photoelectron spectroscopy analysis of hexafluorodianhydride-oxydianiline polyimide: substantiation for substituent effects on aromatic carbon 1s binding energies", Journal of Vacuum Science Technology, A5, vol. 2, (1987), pp. 226-230.

12) G. Beamson D. Briggs,: High resolution XPS of organic polymers, The Scienta ESCA300 database, John Wiley & Sons, Chichster, UK, (1992).

13) J. F. Moulder, W. F. Stickle, P. E. Sobol, K. D. Bomben, J. Chastain, (Ed): Handbook of x-ray photoelectron spectroscopy, Perkin-Elmer Corpration, Eden Prairie, CA, (1992).

14) B. J. Bachman, M. J.Vasile," Ion bombardment of polyimide Films", Journal of Vacuum Science Technolgy, A7, vol. 4, (1989), pp. 2709-2716.

15) Chung, S. Y., Brinza, D. E., Stiegman, A. E., Liang, R. H.: Evaluation and mitigation of energetic atomic oxygen effects on neutral particle beam neutralizer, final report, Jet Propulsion Laboratory, September 30, (1993).

16) G. E. Caledonia, R. H. Krech, B. D. Green, "A High Flux Source of Energetic Oxygen Atoms for Material Degradation Studies," AIAA Journal, vol. 25, (1987), pp.59-63.

17) J. I..Kleiman, Z. A. Iskanderova, Y. I. Gudimienko, R. C. Tennyson, "Potential Applications of Hyperthermal Atomic Oxygen for Treatment of Materials and Structures", Surface and Interface Analysis, vol. 23, (1995) pp. 289-298.

18) M. A. Golub, T.Wyderen, "Reaction of atomic oxygen (O(3P)) with various polymer films", Polymer Degradation and Stability, vol. 22, (1988), pp. 325-338.

19) V. N. Chernik, "Atomic oxygen simulation by plasma dynamic accelerator with charge exchange", Proceedings of 7th Int. Symposium Materials in Space Environment, Toulouse, France, June 1997, ESA-399, pp. 237-241.

20) H. Hashimoto, K.Ohta, "Materials exposure experiment on space shuttle", Proceedings of 10th Space Station Symposium, Tokyo, May (1994), pp. 83-84.

21) T. K.Minton, T. A. Moore, "Molecular beam scattering from ^{13}C-enriched Kapton and correlation with the EOIM-3 carosel experiment, LDEF-69 months in space", Third post-retrieval symposium, Williamsburg, VA, Nov. (1993), pp. 1095-1114.

22) The adsorption probability (Ra) is defined by

Ra = [number of adsorbed oxygen]/[number of incoming AO].

23) D. B. Oakes, R. H. Krech, B. L. Upschulte, G. E. Caledonia, "Oxidation of polycrystalline silver films by

hyperthermal oxygen atoms", Journal of Applied Physics, vol. 77, (1995), pp. 2166-2172.
24) T. K. Minton, J. W. Seale, D. J. Garton, A. K. Frandsen, "Dynamics of Atomic-Oxygen-Induced Degradation of Materials", Proceeding of Protection of Materials and Structures from the LEO Space Environment, Toronto, Canada, April (1998), Paper no. A2.
25) D. J. Garton, T. K.Minton, M. Alagia, N. Balucani, P. Casavecchia, G. G.Volpi, "Atomic oxygen interactions with saturated hydrocarbon surfaces", AIAA Paper No.97-3947, (1997).
26) T. R. Gengenbach, H. I. Griesser, "Aging of 1,3-diaminopropane plasma-deposited polymer films: Mechanisms and reaction pathways", Journal of Polymer Science, Part A, vol. 37, (1999), p 2191-2206.

Chapter 5

Low-temperature oxidation of Si(001) due to the hyperthermal AO beam exposure

Abstract

Oxidation of Si(001) surface exposed to hyperthermal AO beam, which was generated by the laser detonation-type AO source, was studied in order to apply hyperthermal atom beam technique to the low-temperature oxidation process of silicon wafer. The sample temperature, beam translational energy, and AO flux dependence of the oxide growth were investigated using X-ray photoelectron spectroscopy. The Si(001) surfaces were oxidized even at room temperature by the hyperthermal AO beam exposure and the oxide thickness reached a terminal thickness of a few nanometers. The oxide thickness was found to increase with increasing sample temperature. All oxidation curves at 297 K showed the fast and slow diffusion stages in all AO fluxes and translational energies tested. The high AO flux caused the decrease of the O concentration in the oxide film, and caused the increase of the oxidation rate. The terminal oxide thickness increased with increasing the translational energy and was proportional to the normal energy $E_{\perp}$. These experimental results clearly indicated that the dominant driving force of the hyperthermal beam oxidation of Si(001) was the energy transfer process from the scattered beam species to the SiO_2 layer.

5.1 Introduction

Silicon dioxide (SiO_2) has been widely used as an insulating layer for metal-oxide-semiconductor (MOS) devices. SiO_2 layers are typically formed by a high-temperature thermal oxidation process that has the capability to grow uniform and relatively thick (tens of nanometers) oxide layers with good electrical properties[1]. However, the high-temperature process cannot be applied once the device structure is

formed. Therefore, establishment of a reliable low-temperature oxidation process is necessary in order to develop three-dimensional integration of electronic circuits. In addition, dopant re-distribution by oxidation-enhanced diffusion (OED), oxygen-induced stacking fault (OSF), and dislocation generation could be minimized or eliminated by a low-temperature oxidation process. Furthermore, the trend toward smaller feature dimensions for ultra large-scale integrated circuits (ULSIs) has intensified the need for SiO_2 layers as thin as a few nanometers. Thus, the desirable oxidation technology of the future will be capable of producing very thin SiO_2 layers at ambient temperatures.

Recent approaches to such a low-temperature oxidation have involved the direct oxidation of silicon with highly reactive oxidants, such as atomic oxygen[2,3,4] or ozone[5]. Oxygen atoms are usually generated in oxygen plasma, and the substrates are often exposed outside the plasma in order to avoid the bombardment by energetic ions. The kinetic energy distribution of the AO downstream of the plasma is Maxwellian, with an average translational energy of ~0.04 eV. At these low translational energies, temperatures of hundreds of degrees Celsius are required for oxide growth at practical rates. Beam techniques have been used to produce atomic or ionic species with enough kinetic energy (a few eV) to overcome the potential barrier of oxidation at a silicon surface, and thin oxide films have been produced even at room temperature[6,7,8]. However, the beam diameters used have been too small to make these techniques practical for ULSI manufacturing with large-diameter wafers (>30 cm in diameter).

The laser detonation-type AO source can deliver pulses of AO with kinetic energies in the range 2-15 eV and fluxes of about 10^{14} atoms/cm^2/s over areas as large as 1000 cm^2. This high AO flux in the source is advantageous for low-temperature oxidation of silicon, because the rate-limiting process is the diffusion rate in the oxide layer, which is much higher for AO than molecular oxygen[1]. The characteristics of this source make it attractive as a possible technology to create thin oxide layers on silicon at room temperature.

In this chapter, Si(001) surfaces were exposed to the hyperthermal AO beam generated by the laser detonation-type AO source. The sample temperature, beam translational energy, and AO flux dependence of the oxide growth were investigated using XPS. From the experimental results, the dominant driving force of the

hyperthermal beam oxidation, as well as the advantageous of this technique for the low-temperature oxidation process will be discussed.

5.2 Experiment

The AO source used for the formation of silicon oxide was the laser detonation-type AO source and its detail has already been shown in chapter 3. In order to investigate translational energy dependence of the reaction, the hyperthermal AO beams with three different translational energies were directed to the sample surfaces. The conditions of the hyperthermal AO beams used in this chapter are summarized in table 1. The mean energies of the hyperthermal AO component were 4.6 eV (beam A), 3.6 eV (beam B), and 1.6 eV (beam C). Moreover, for tuning the AO flux on the sample surface, the distance between the nozzle and the sample was adjusted by considering that the AO flux is inversely proportional to the square of the distance from the nozzle throat. The incident angle of the beam was 0°, except for the experiment on incident angle dependence (0° ~ 70°).

Table 5.1 The beam conditions in this chapter.

	Translational energy of hyperthermal component (eV)		Composition of hyperthermal component (%)		*AO flux ($x10^{14}$atoms/cm^2/s)
	AO	O_2	AO	O_2	
Beam A (4.6eV)	4.6	4.3	27	73	3.1
Beam B (3.6eV)	3.6	2.9	8	92	5.1
Beam C (1.6eV)	1.6	1.6	6	94	10.6

*AO fluxes were measured at the sample position of 47 cm away from the nozzle.

Samples used in this study were p-Si(001) wafers. A native oxide was removed by the RCA cleaning and the H-terminated Si(001) surface was prepared by HF (2%) treatment. The RCA cleaning used in this study was carried out by the following procedures:

(1) Ultrasonic cleaning with ethanol for 5 min.
(2) Ultrasonic cleaning with deionized water for 5 min.
(3) Dipping in a 2% HF solution at room temperature for10 s.
(4) Boiling in a $NH_3OH : H_2O_2 = 1 : 1$ solution at 80°C for 10 min.
(5) Dipping in a deionized water for 1 min.
(6) Dipping in a 2% HF solution for 10 s.
(7) Dipping in a deionized water for 5 s.
(8) Repeating the sequences form (4) to (7) twice (total 3 times).
(9) Dried in air.

A H-terminated Si wafer, thus prepared, was immediately installed in the vacuum chamber and the surface was examined by XPS. After no oxygen peak was confirmed in the XPS spectrum, the sample was transferred to the exposure position and exposed to hyperthermal AO beams. Some of the XPS measurements of the AO-exposed Si(001) carried out after ambient air exposure. However, the stability of oxide thickness during the sample transfer in air has been identified before the experiment, and no additional oxide growth due to the air exposure at room temperature was confirmed.

5.3 Method of XPS analysis

The oxide thickness formed on a Si(001) wafer was measured with XPS spectra. The XPS Si2p spectrum obtained from the oxide-covered Si (001) shows a peak at 99 eV, which comes from Si substrate, and that at 103 eV coming from the SiO_2 film over the Si (001) substrate. The peak area of each signal reveals the atomic concentration of Si atom in the Si crystal and in the SiO_2 film within the escape depth of

photoelectrons[9].

Signal intensities of photoelectron from the Si substrate and the SiO_2 film are written in the following formulae;

$$I_{Si} = [\, exp\, \{ -d/(\lambda \cos \varphi) \} \,] I_{Si}^* \qquad (1)$$

$$I_{SiO2} = [\, 1 - exp\, \{ -d/(\lambda \cos \varphi) \} \,] I_{SiO2}^* \qquad (2)$$

where, d is the SiO_2 film thickness, λ is the mean free path of the photoelectrons in the SiO_2 film, φ is the take off angle of the photoelectrons, and I_{Si}^* and I_{SiO2}^* are the photoelectron intensities obtained from the bulk Si and bulk SiO_2 materials. Here, mean free path of the photoelectrons of Si with kinetic energies of 1154.6 eV (binding energy of 99eV) and of 1150.6 eV (binding energy of 103 eV) are close enough to be

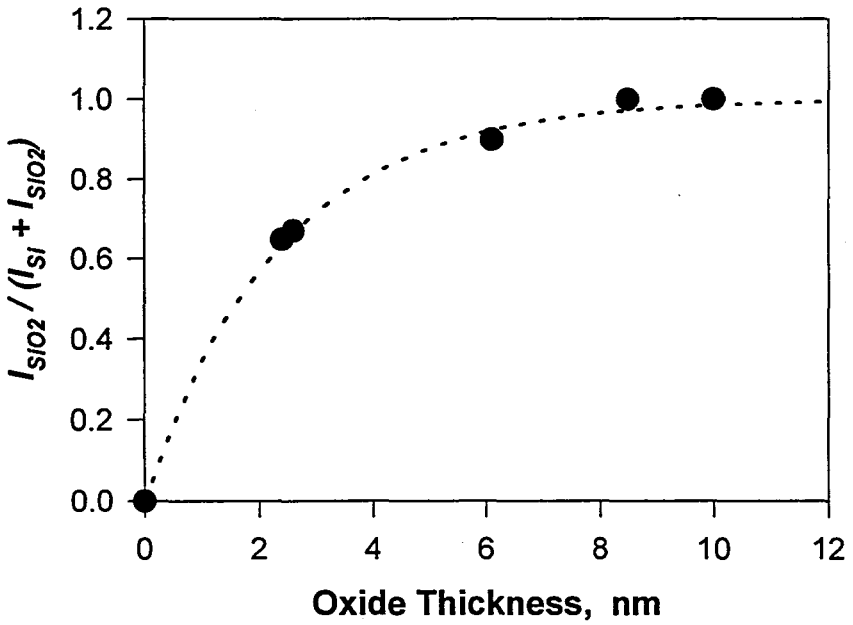

Figure 5.1 The theoretical calculation (dotted line) and the experimental data (filled circles) of the relative area of Si^{4+} peak in the Si 2p XPS spectrum in function with the oxide thickness.

considered as of the same value (Mg Kα line, 1253.6 eV, was used for XPS measurement). When atomic densities and photoionization yields of the Si atoms consisting of the Si substrate and the SiO_2 film, are considered to be uniform, i. e., $I_{Si}^* = I_{SiO2}^*$, sum of the equations (1) and (2) gives 1. Therefore, the fraction of I_{SiO2} signal at 103 eV in the whole Si 2p photoelectron signals (99 eV plus 103 eV) is written in the next equation:

$$I_{SiO2} / (I_{SiO2} + I_{Si}) = 1 - \exp \{ -d / (\lambda \cos \varphi) \} \qquad (3)$$

Since $\lambda \cos \varphi$ is a constant, one can determine this value from the data.

The samples with known oxide thicknesses[10] were measured with XPS and the results were curve-fitted with the use of the equation (3). The relationship between the oxide thickness and $I_{SiO2} / (I_{SiO2} + I_{Si})$ ratio is shown in Figure 5.1. As is shown in Figure 5.1, XPS data points (solid circles) are well described by the equation (3), and the best fit curve was obtained with $\lambda \cos \varphi = 2.386$ nm (take off angle, φ, was fixed at 45°). This value agrees well with the mean free path of Si 2p photoelectrons in the SiO_2 film measured by the angle resolved-XPS study (3.2 nm)[11]. All of the oxide thicknesses of the beam oxidized samples reported here were calculated with the equation (3) with $\lambda \cos \varphi = 2.386$ nm.

5.4 The linear-parabolic model for oxidation of Si

In the thermal oxidation process of the Si single crystal, it is widely known that the oxidants, such as AO or O_2, diffuse into SiO_2 film and the Si atom is oxidized when oxidants reach the Si/SiO_2 interface. Based upon this reaction scheme, Deal and Grove proposed the model for thermal oxidation in silicon/oxygen system[12]. The model was based on three stages:

(a) Oxidants are transported from the oxidizing gas to the SiO_2 surface.

(b) Oxidants diffuse across the oxide film towards the silicon structure.

(c) Oxidants react with silicon atoms at the oxide/silicon interface, and form a new layer of SiO_2.

These three stages of reaction was illustrated in Figure 5.2. At the stage (a), the oxidant flux F_1 from the oxidizing gas to the SiO_2 surface is described by

$$F_1 = h_g(C_g - C_s) \tag{4}$$

where h_g is a gas-phase transport coefficient, C_g and C_s are the concentrations of the oxidant in the gas region and the SiO_2 surface, respectively. From Henry's law, the equilibrium concentration of the oxidants at the SiO_2 surface (C_0) and that of the oxidant in the oxide film (C^*) are given by

$$C_0 = HP_s \tag{5}$$

$$C^* = HP_g \tag{6},$$

where H is Henry's law constant, P_g and P_s are partial pressure of the oxidants in the gas region and at the SiO_2 surface, respectively. From Henry's law and the ideal gas law, C_g and C_s are given by

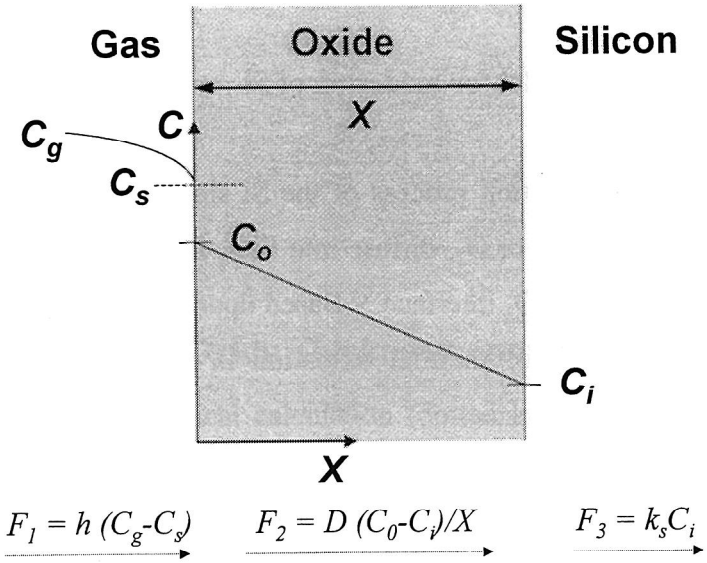

Figure 5.2 A model for the oxidation of silicon.

$$C_g = P_g/kT \quad (7)$$

$$C_s = P_s/kT \quad (8).$$

Using equations (5)-(8), equation (4) is converted to the follow equation;

$$F_1 = h\,(C^*-C_0) \quad (9)$$

where h is the rate constant at outer oxide surface, and given by the next equation.

$$h=h_g/HkT \quad (10).$$

In the stage (b), the oxidant flux F_2 which represent the flux from the SiO_2 surface of the oxide to the SiO_2/Si interface is assumed to obey the Fick's law,

$$F_2 = D\,(C_0-C_i)/X \quad (11).$$

where D is the effective diffusion coefficient, C_i is the concentration of the oxidant at the SiO_2/Si interface, and X is the thickness of the oxide.

In the stage (c), the flux F_3, which corresponds to the oxidation reaction rate at the SiO_2/Si interface, is expressed by the first-order relation;

$$F_3 = k_s C_i \quad (12).$$

Where k_s is the rate constant of the oxidation reaction at the SiO_2/Si interface.

In the steady-state oxidation reaction, one can consider the following relationship,

$$F_1 = F_2 = F_3 \quad (13).$$

Using the equations (9) - (13), one obtains

$$C_i = \frac{C^*}{1+\left(\frac{k_s}{h}\right)+\left(\frac{k_s X}{D}\right)} \tag{14}$$

$$C_0 = \frac{C^*\left(1+\frac{k_s X}{D}\right)}{1+\left(\frac{k_s}{h}\right)+\left(\frac{k_s X}{D}\right)} \tag{15}.$$

When the diffusion rate across the oxide is lower than the reaction rate at the SiO_2/Si interface (i. e., $D/k_sX \rightarrow 0$), equations (14) and (15) become

$$C_i \rightarrow 0 \text{ and } C_0 \rightarrow C^* \tag{16}.$$

This condition is commonly referred to as "diffusion controlled."

The rate of growth of the oxide layer is given by the differential equation

$$\frac{dX}{dt} = \frac{F_3}{N_{ox}} = \frac{k_s C^*}{1+\left(\frac{k_s}{h}\right)+\left(\frac{k_s X}{D}\right)} \tag{17}.$$

where N_{ox} is the number of oxidant incorporated into a unit volume of the oxide layer. From equation (17), one obtains the relationship of

$$X^2+AX = B(t+\tau) \tag{18}$$

where

$$A = 2D\left(\frac{1}{k_s}+\frac{1}{h}\right) \tag{19}$$

$$B = 2DC^*/N_{ox} \tag{20}$$

$$\tau = (X_0^2+A\,X_0)/B \tag{21}.$$

When the native oxide with a thickness of X_0 existed before the oxidation process, the initial condition is $X = X_0$ at $t = 0$. The τ corresponds to a shift in the time coordinate which corrects for the presence of the initial oxide layer X_0. Solving the quadratic equation (18) yields the form

$$X = \frac{A}{2}\left\{\sqrt{1 + \frac{t+\tau}{A^2/4B}} - 1\right\} \qquad (22).$$

At relatively large oxidation time, i. e., $t >> \tau$ and $t >> A^2/4B$, equation (22) was approximated as equation (23).

$$X^2 \cong Bt \qquad (23).$$

The equation (23) is referred as the "parabolic oxidation law", and B is the parabolic rate constant. In contrast, at the beginning of the reaction, i. e., $t << A^2/4B$, one can obtain the relationship

$$X = \frac{B}{A}(t + \tau) \qquad (24).$$

The equation (24) is referred to as the "linear oxidation law", and B/A is the linear rate constant. As described above, the Deal-Grove model explains the linear relationship between the oxide thickness and oxidation time at the beginning of the oxidation reaction process, and the parabolic relationship in the later oxidation stage.

5.5 Results and discussion

5.5.1 Temperature Dependence

Figure 5.3 indicates the XPS Si 2p spectra of the Si(001) surfaces before (a) and after hyperthermal AO exposure with a fluence of 1.1×10^{18} atoms/cm^2 and mean translational energy of 4.6 eV at the sample temperature of $T_s = 297$ K (b). Only the peak at 99 eV (Si^0) is observed in the XPS spectrum before exposure as shown in Figure 5.3 (a). However, high-energy peak at 103 eV is clearly obvious in Figure 5.3 (b). The Si 2p XPS spectra were deconvoluted with Si^{0+} and Si^{4+} peaks at 99 and 103 eV. A spin-orbital splitting of the Si 2p orbit was not subtracted from the XPS spectra because of the insufficient resolution of the spectrometer. The presence of Si^{4+} peak indicated that Si(001) surface was oxidized due to the hyperthermal beam exposure even at room temperature. It has been reported that the adsorption of thermal AO on H-terminated Si(001) surface is only observed at high temperature of 500 °C[13]. It is considered that the oxidation at room temperature is achieved by the high translational

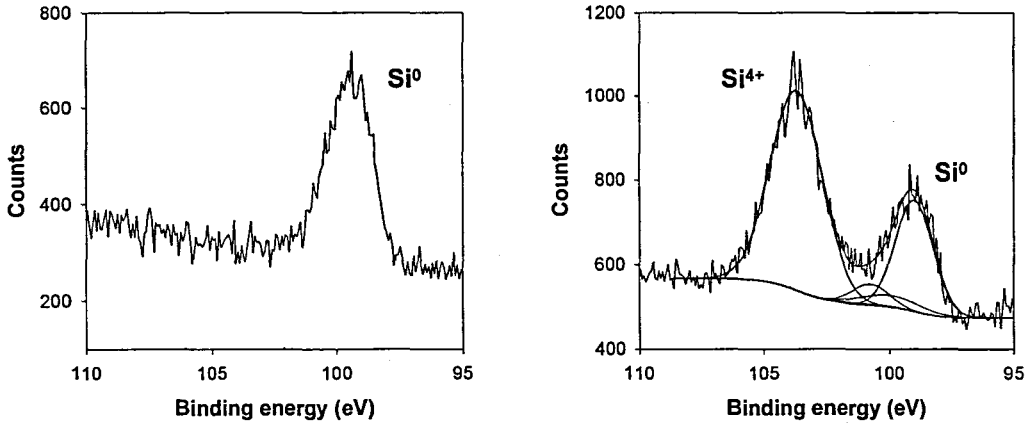

(a) before exposure **(b) after exposure**

Figure 5.3 The XPS Si 2p spectra of the Si(001) surfaces before (a) and after hyperthermal AO beam exposure with the fluence of 1.1×10^{18} atoms/cm^2 and the mean translational energy of 4.6 eV at $T_s = 297$K (b).

energy of the beam, i. e., the hyperthermal species (AO and/or O_2) easily adsorbs on the H-terminated Si(001) surface even at room temperature.

Figure 5.4 demonstrates the growths of the oxide on the Si (001) wafer as a function of AO fluence with an AO flux of 2.8×10^{13} atoms/cm^2/s and mean AO translational energy of 4.6 eV at sample temperature T_s = 297, 399, and 493 K. As is shown in this Figure, the oxide grows with the AO fluences. Also, the oxidation rate increases with increasing sample temperature. However, the oxidation curve at 297 K is close to that at 399 K with the AO fluences lower than 6×10^{17} atoms/cm^2. In Figure 5.4, the shapes of the three curves are close to being parabolic, one finds that the linear part is hardly obvious. The linear part is usually observed, in high temperature thermal oxidations. The absence of this linear part may be explained by the high reaction rate of the hyperthermal species. Figure 5.4 are replotted in Figures 5.5 (a)-(c) with the longitude in the squares of the oxide thickness in the ordinate. Since the AO beam was operated as a pulse beam (repetition 1 Hz), the beam exposure time per shots is

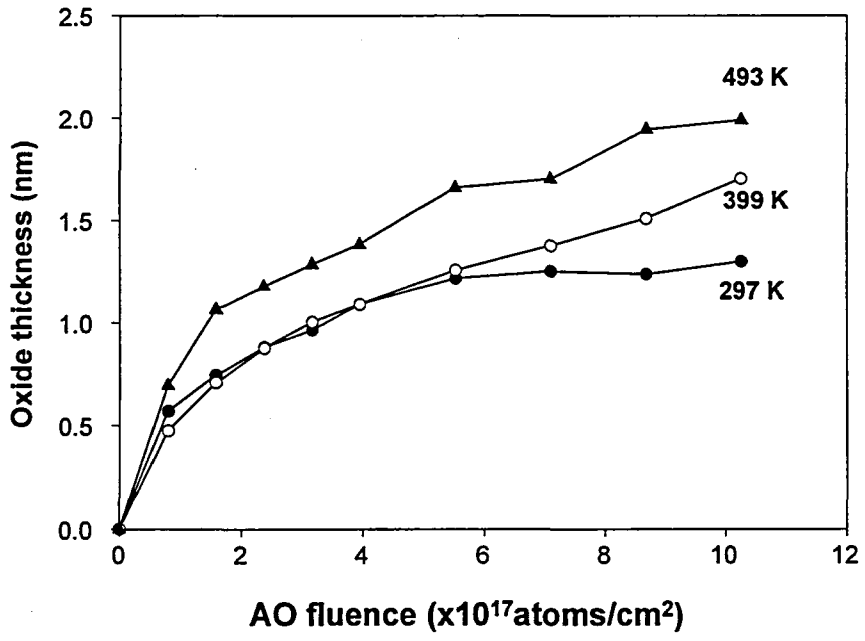

Figure 5.4 The oxide grow curves of the Si (001) surfaces with the AO flux of 2.8×10^{13} atoms/cm^2/s, AO translational energy of 4.6 eV, sample temperatures of 297, 399, and 493 K.

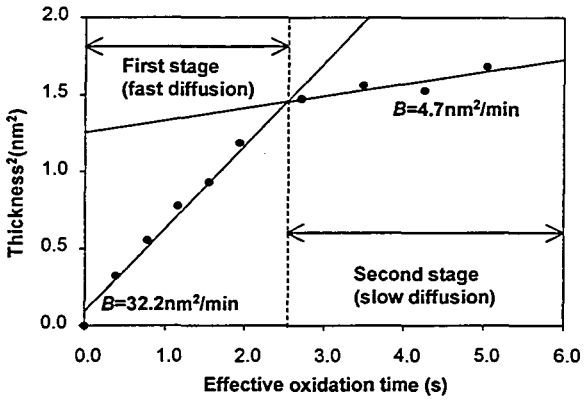

(a) 297 K

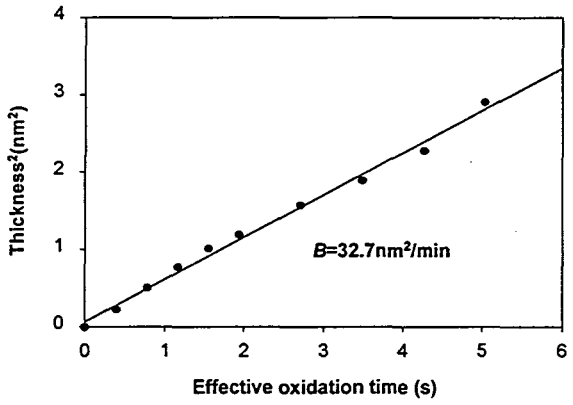

(b) 399 K

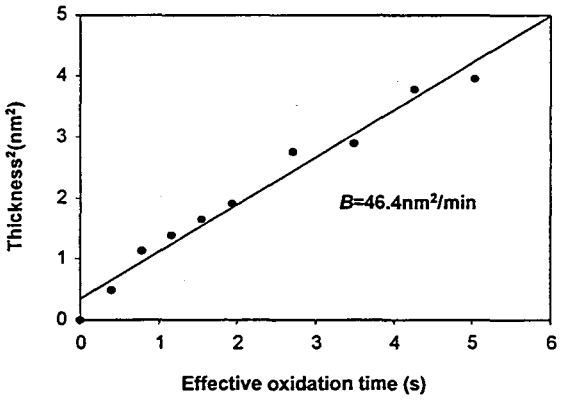

(c) 493 K

Figure 5.5 The square of the oxide thickness as a function of the estimated hyperthermal beam exposure time. AO flux is 2.8×10^{13} atoms/cm^2/s, and the AO translational energy is 4.6 eV. The sample temperatures are 297 (a), 399 (b), and 493 K (c).

estimated from the pulse width of the TOF distribution of the AO at the sample position. The pulse width of the TOF distribution of the AO at QMS position (181.5 cm) is 175 μs, therefore, the width of the TOF distribution of the AO at the sample position (134.0 cm) is estimated to be 129 μs. The abscissas in Figures 5.5 (a)-(c) were calculated by multiplying the pulse width and the number of pulse. This exposure time was represented as the effective oxidation time. The solid lines in Figures 5.5 were obtained by a least-square fit. It is obvious that the squares of the oxide thickness in Figures 5.5 (b) and (c) are proportional to AO exposure time; oxidation curves at 399 and 493 K obey the parabolic law (diffusion process). The parabolic rate constant B at 399 and 493 K are calculated to be 32.7 and 46.4 nm^2/min, respectively, from the slops in Figures 5.5 (b) and (c). However, one finds that Figure 5.5 (a) can be fitted by two straight lines with B of 32.2nm^2/min (first stage) and 4.7 nm^2/min (second stage). This means that the oxidation process at 297 K contains the fast and slow diffusion processes. Since each line agrees well with the experimental data, it is concluded that the rate-limiting processes of the hyperthermal AO beam oxidation in both stages at 297 K are the diffusion process.

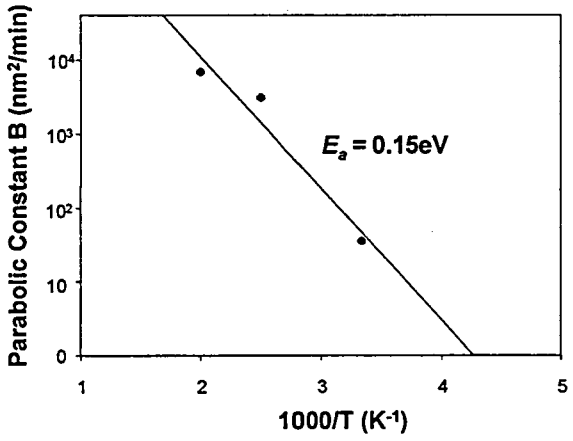

Figure 5.6 The Arrhenius plot of the parabolic constant. The parabolic constant is assigned by equation (23).

Figure 5.6 shows the results of Arrhenius plot of the diffusion constant B. In Figure 5.6, the B of 4.7 nm^2/min at 297 K is adopted[14]. The solid line in Figure 5.6 is obtained by the least-square fit by $B = B_0\exp(-E_a/kT_s)$, where B_0 is the pre-exponential factor, E_a is the activation energy of the diffusion of the oxidant. From this solid line, the activation energy is estimated to be 0.15 eV. It has been reported that the activation energy of the conventional thermal O_2 oxidation is 1.5 - 2.0 eV[15]. Moreover, the activation energy of 0.5 eV is reported in the plasma oxidation[16]. The hyperthermal AO beam oxidation showed very low activation energy, which would be influenced by the high translational energy of the hyperthermal species.

5.4.3 Flux Dependence

The surface oxygen concentration C_s is one of the driving forces of the volume diffusion. We measured oxidation curves on the Si(001) exposed to the hyperthermal AO beam with the translational energy of 4.6 eV at 297 K with different AO fluxes. These oxidation curves are shown in Figure 5.7. The AO fluxes are 2.8×10^{13},

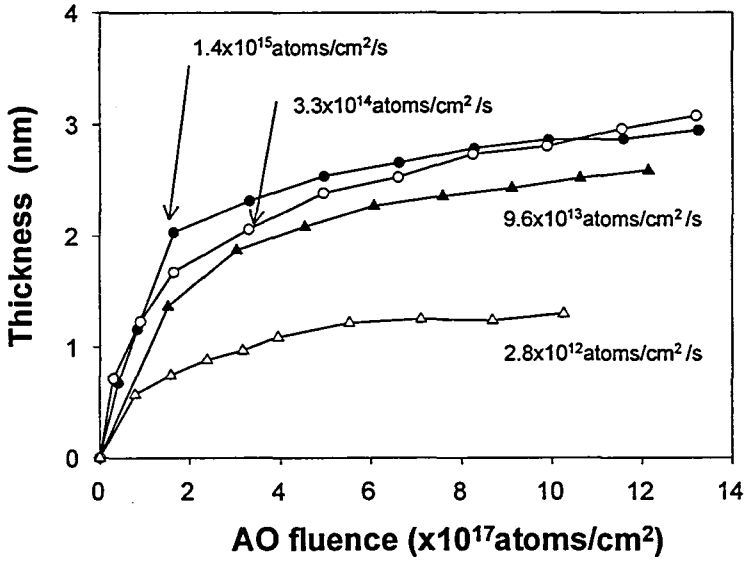

Figure 5.7 The oxide thickness as a function of AO fluence with the AO fluxes of 2.8×10^{13}, 9.6×10^{13}, 3.3×10^{14}, and 1.4×10^{15} atoms/cm^2/s at 297 K. The AO translational energy is 4.6 eV.

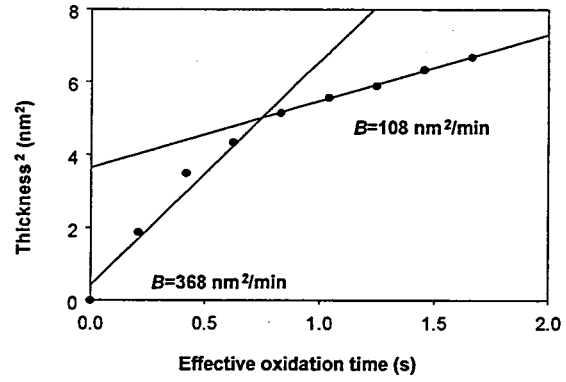

(a) 9.6×10^{13} atoms/cm²/s

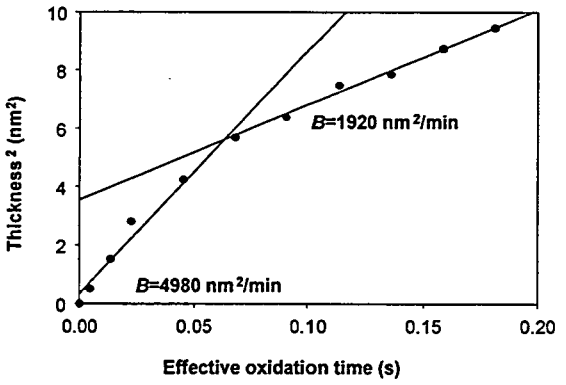

(b) 3.3×10^{14} atoms/cm²/s

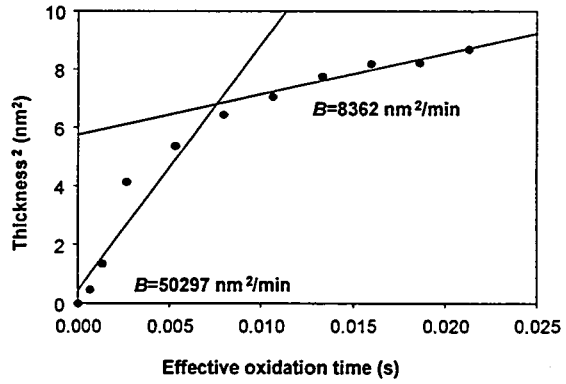

(c) 1.4×10^{15} atoms/cm²/s

Figure 5.8 The square of the oxide thickness as a function of the estimated hyperthermal beam exposure time with different AO fluxes at 297 K. The translational energy is 4.6 eV. The AO fluxes are 9.6×10^{13} (a), 3.3×10^{14} (b) 1.4×10^{15} atoms/cm²/s (c).

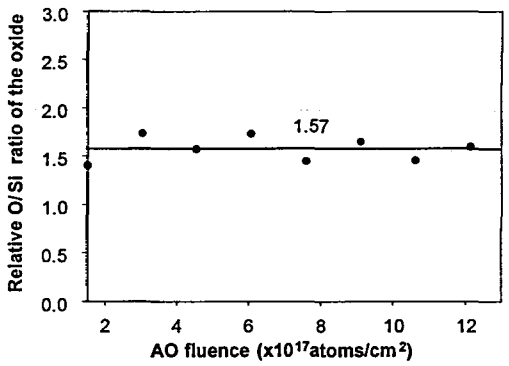

(a) 9.6×10^{13} atoms/cm^2/s

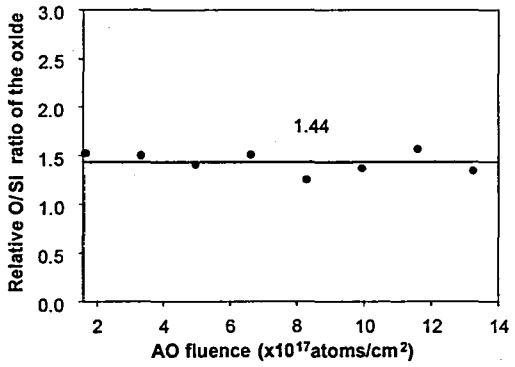

(b) 3.3×10^{14} atoms/cm^2/s

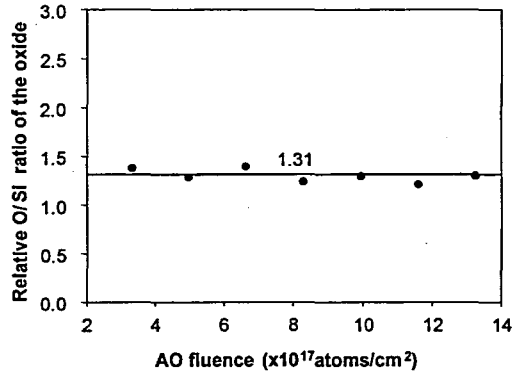

(c) 1.4×10^{15} atoms/cm^2/s

Figure 5.9 The O/Si ratio of the oxide on the Si (001) wafers exposed to the hyperthermal AO beam with the AO fluxes of 9.6×10^{13} (a), 3.3×10^{13} (b), 1.4×10^{15} atoms/cm^2/s (c) at 297 K.

9.6×10^{13}, 3.3×10^{14}, and 1.4×10^{15} atoms/cm^2/s. Obviously, even in the same AO fluence and sample temperature, the thickness of oxide film increases at high AO fluxes. Figure 5.8 indicates the relationships between the squares of the oxide thickness and the effective oxidation time with AO fluxes of 9.6×10^{13} (a), 3.3×10^{14} (b), and 1.4×10^{15} atoms/cm^2/s (c). The effective oxidation time per pulse is estimated to be 94.5 (a), 45.3 (b), and 22.2 μs (c). The graph for 2.8×10^{13} atoms/cm^2/s is already shown in Figure 5.5 (a). The diffusion rate constant *B* increases with increasing the AO flux. It is obvious that all squares of those oxide thicknesses are fitted by two straight lines with *B* for the fast and slow processes. In addition, relative O/Si ratio in the oxide film was measured from the relative peak areas of the O1s and Si^{4+}2p peaks in the XPS spectra[17]. Figure 5.9 represents the relative O/Si ratio of the oxide on the Si (001) wafers exposed to the hyperthermal AO beam with the AO fluxes of 9.6×10^{13} (a), 3.3×10^{14} (b), and 1.4×10^{15} atoms/cm^2 (c), respectively. It is obvious that the relative O/Si ratios of the oxide are independent of the AO fluence, however, it decreases with increasing the AO flux. Namely, remarkable increase of the oxygen density adsorbed on the SiO_2 surface was not observed.

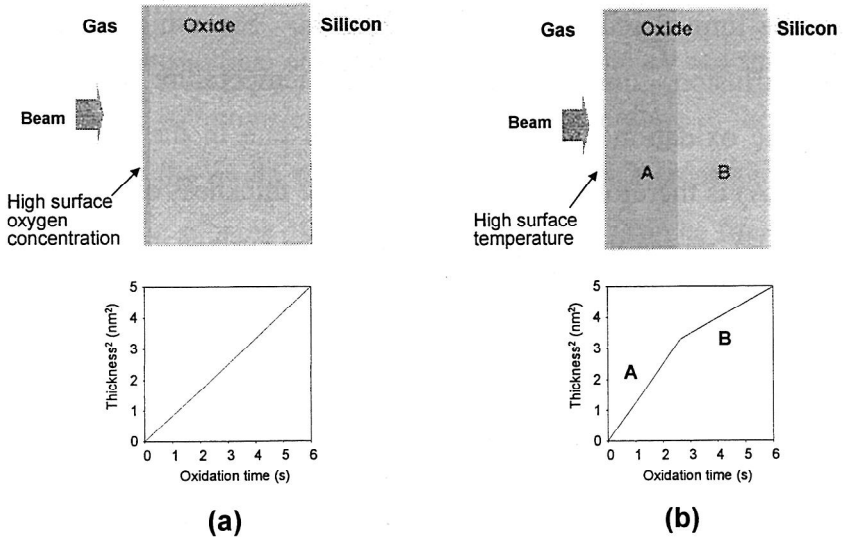

Figure 5.10 The induced-oxidation model for the high surface oxygen concentration (a) and the high local surface temperature (b).

High surface concentration causes high oxidation rate, i. e., the increase of the C_s leads to the increase of B. Considering the equation (23), the increase of the oxidation thickness due to the increase of B is observed at all diffusion stage, i. e., squares of oxidation curve is fitted by one straight line (see Figure 5.10 (a)). However, the square of the oxidation curves at 297 K cannot be fitted by one straight line. It is, therefore, considered that the high surface oxygen concentration does not result in the increase of the oxidation rate.

5.4.4 Translational energy and angular dependences

The high AO flux results in the amount of impinging beam species (AO and O_2) per time. In gas-surface collision process, translational energies of impinging hyperthermal species are usually transferred to the solid surface. The transferred energies are mainly used for increasing phonon vibration of the surface, i. e., heating the atoms. Thus, the high AO flux is considered to give rise to the increase of surface local temperature. Considering that the heat source located the topmost surface and the low thermal conductivity of SiO_2 (0.002 cal/cm/s/deg at 300K), the temperature increase may be limited only at the surface region. Since high temperature enhance the volume diffusion, that the high surface temperature causes the oxidation enhancement the oxidation process. The growth rate in the thin oxide region near surface (region A) is therefore faster than that in the thickness oxide region far from the surface (region B), where the temperature rise at the surface does not cover the oxide. This consideration may explain the experimental results of the fast oxidation rate in the first stage at 297 K and the high oxidation rate at high AO flux. In constract, if the major driving force of the AO diffusion in SiO_2 is considered to be the AO concentration at surface, it cannot explain the two-stage diffusion observed in Figures 5.5 (a), 5.8 (a), 5.8 (b), and 5.8 (c) (see Figure 10 (a)). Therefore it is considered that the dominant driving force of the hyperthermal AO beam oxidation of Si is the heat due to the translational energy transfer from the beam species to the surface.

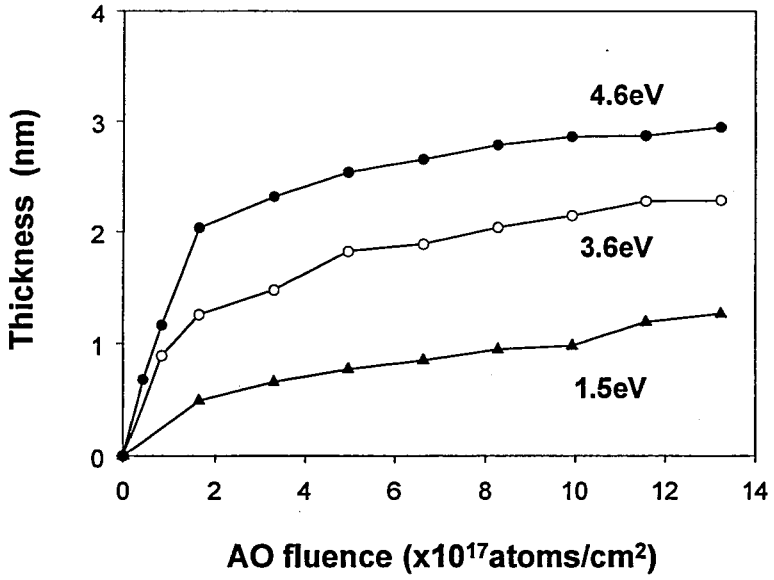

Figure 5.11 The oxide thickness of the Si (001) surface during the hyperthermal beam exposures with the AO translational energies of 1.5, 3.6 and 4.6 eV. The AO flux was 1.4×10^{15}atoms/cm^2/s and the sample temperature was 297 K.

In order to clarify this point, we investigated the translational energy dependence of the oxidation reaction. The oxide growth curves on Si (001) by AO beam exposure with translational energies of 1.5, 3.6 and 4.6 eV are shown Figure 5.11. The AO flux was 1.4×10^{15}atoms/cm^2/s and the bulk temperature of the sample was 297 K. It is obvious that the oxide thickness increases with increasing the translational energy. In addition, the squares of those oxide thicknesses can be fitted by two straight lines (not shown). It is clearly observed in Figure 5.11 that a break point is observed at the SiO_2 thickness of 1 ~ 2 nm depending on the AO flux. The oxide growth rates in the later stage seems to be independent of the beam energy. However, in the beginning of the oxidation the oxidation rate depends on the AO energy, which can be explained by the heating effect due to the energy transfer mechanism.

We also investigated the relationship between the oxide thickness and the incident angle. The filled circles shown in Figure 5.12 were obtained at the AO exposure condition with an AO translational energy of 4.6 eV and an AO flux of 2.4 ×

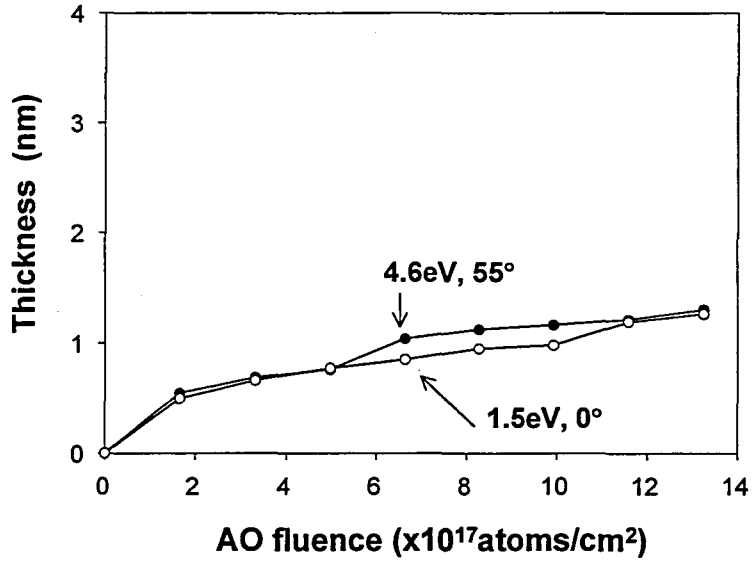

Figure 5.12 The oxide thickness of the Si (001) surface exposed to AO beam with different exposure conditions. The filled circle is obtained with the AO translational energy of 4.6 eV and the AO flux of 2.4 × 10^{15}atoms/cm^2/s with the incident angle of 55°. The open circle indicates the oxidation curve same as that in Figure 5.11 with 1.5 eV.

10^{15}atoms/cm^2/s at an incident angle of 55°. The open circles shown in Figure 5.12 indicate the oxidation curve which is the same of Figure 5.11 (the AO flux of 1.4 × 10^{15} atoms/cm^2/s and the AO translational energy of 1.5 eV at an incident angle of 0°). One can see two oxidation curves coincide. In the case of the incident angle of 55°, the incident normal flux $F_\perp$ and the incident normal energy $E_\perp$, which is the translational energy calculated from the normal component of AO velocity, are calculated to be 1.4 × 10^{15} atoms/cm^2/s and 1.5 eV by assuming the relationships of $F_\perp = F_i \cos\theta_i$ and $E_\perp = E_i \cos^2\theta_i$ (F_i the incident AO flux at the normal incidence condition, E_i the total AO translational energy). So, the exposure conditions of two beams regarding to the surface normal direction are identical. The experimental result in Figure 5.12 indicates that the oxide thickness depends on $F_\perp$ and $E_\perp$, not on F_i and E_i.

The angular dependence of oxide growth was studied in the same AO beam condition. Figure 5.13 indicates the terminal oxide thicknesses of the Si (001) surfaces

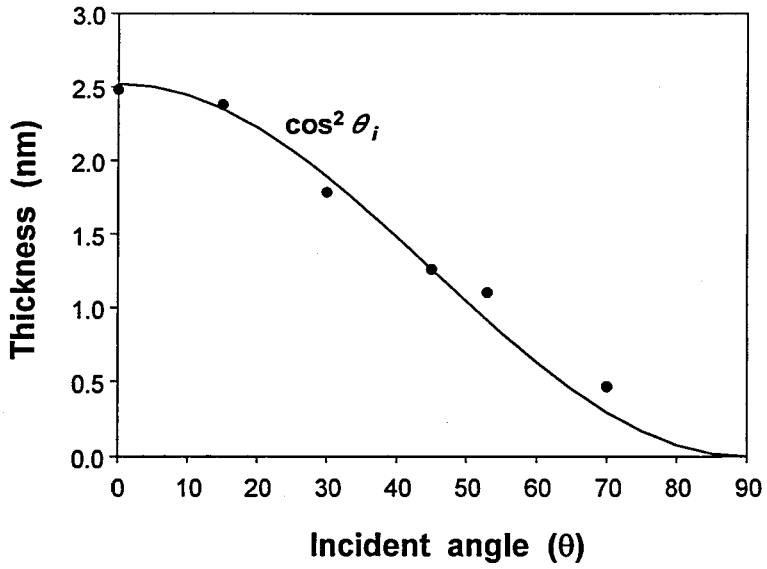

Figure 5.13 The relationship between the oxide thickness on the Si (001) surface and the incident angle of the beam. The AO beam exposure conditions of all data points are unified; AO flux was 3.0×10^{14}atoms/cm^2/s (normal condition), AO fluence was 9.0×10^{18}atoms/cm^2 (normal condition), and the sample temperature was 297 K.

as a function of incident angle of the AO beam with a translational energy of 4.6 eV, AO flux of 3.0×10^{14} atoms/cm^2/s (normal incidence), and total AO fluence of 9.0×10^{18} atoms/cm^2 (normal incidence) at 297 K. The solid curve is the least-square fit by using the relation of $\cos^2\theta_i$. This result clearly shows that the oxidation thickness is proportional to $\cos^2\theta_i$, i. e., $E_\perp$. It is widely known in gas-surface collision process that the adsorption process leads to the loss of all translational energy of the species (trapping), whereas only normal component at the translational energy will be lost in the scattering process (inelastic-scattering). In the former case, the amount of energies transferred to surface is proportional to E_i, but in the latter case, it is proportional to $E_\perp$. It has been reported that the translational energy transfer from the scattered species to the solid surface is proportional to the normal energy $E_\perp$ of incident species in many systems, for example Xe/Ge(001), Ar/Ag(001), Hg/MgO systems, and so on[18]. From

these facts described above, it is concluded that the dominant driving force of the hyperthermal beam oxidation of Si is the energy transfer of the inelastic-scattered species to the surface.

5.5 Conclusion

The laser detonation-type AO source was applied for the low-temperature oxidation process of Si(001) surface. The experimented results observed in this study are summarized as follows;

(1) Si(001) surfaces were oxidized in the hyperthermal beam even at room temperature, and the oxide thickness reached a terminal thickness of a few nanometers. The oxidation rate increased with increasing the sample temperature. The hyperthermal beam oxidation showed activation energy of diffusion (0.15 eV) which was lower than the other oxidation methods.

(2) Oxidation curves at 297 K with different AO fluxes and different translational energies indicated two diffusion processes, the fast and slow diffusion stages.

(3) The high AO flux caused the increases in the oxidation rate and the decrease in the O concentration in the oxide.

(4) The oxide thickness increased with increasing the beam translational energies of AO beam. It was also found that the oxide growth was governed by the normal component of the translational energy $E_{\perp}$.

The behaviors (2)-(4) can be explained by the increase of the lattice temperature at the surface region (~1.5 nm) due to the energy transfer form AO beam to the SiO_2 surface. This experimental evidence of the effect of energy transfer from AO to SiO_2 gives the possibility of promotion of oxidising reaction at the very surface region when the bulk

temperature is kept low. This new finding opens the door to the new low temperature semiconductor process technology with the use of hyperthermal neutral beam.

References

1) F. Shimura: *Semiconductor Silicon Crystal Technology*, (Academic Press, San Diego, 1989).

2) T. Tamura, N. Tanaka, M. Tagawa, N. Ohmae, M. Umeno, ""Effect of External Stresses on the Low Temperature Thermal Oxidation of Silicon", Japanese Journal of Applied Physics, vol. 32, (1993), pp. 12-16.

3) S. Kimura, E. Murakami, T. Warabisako, E. Mitani and H. Sunai,"An ^{18}O study of oxygen exchange phenomena during microwave-discharge plasma oxidation of silicon", Journal of Applied Physics, vol. 63, (1988), pp. 4655-4660.

4) J. Peeters, L. Li, "Oxidation of silicon in plasma afterglows: New model of oxide growth including recombination of diffusing O atoms", Journal of Applied Physics, vol. 73, (1993), pp. 2477-2485.

5) K. Eljabaly and A. Reisman: J. Electrochem. Soc. 138 (1991) 1064.

6) J. R. Engstrom and T. Engel, "Atomic versus molecular reactivity at the gas-solid interface: The adsorption and reaction of atomic oxygen on the Si(100) surface", Physical Review B, vol. 41, (1990), pp. 1038-1041.

7) T. Ono, S. Hiraoka and K. Suzuki, "Oxidation of silicon with a hot oxygen beam", Journal of Vacuum Science Tecnology A11, (1993), pp. 959-963.

8) M. H. Hecht, O. J. Orient, A. Chutijian and R. P. Vasquez: Appl. Phys. Lett. 54 (1989) 421.

9) D. Briggs, M. P. Seah, Practical Surface Analysis, John Wiley & Sons, Sussex, 1983.

10) The Si oxide samples were formed by conventional thermal oxidation. The oxide thicknesses were obtained by ellipsometry measurements.

11) T. Katayama, H. Yamamoto, M. Ikeno, Y. Mashiko, S. Kawazu, M. Umeno, "Accurate thickness determination of both thin SiO2 on Si and thin Si on SiO2 by angle-resolved X-ray photoelectron spectroscopy", Japanese Journal of Applied Physics, vol. 38, (1998), pp. 4172-4179.

12) B. E. Deal and A. S. Grove, "General relationship for the thermal oxidation of silicon", Journal of Applied Physics, vol. 36, (1965), pp. 3770-3778.

13) H. Ikeda, K. Hotta, T. Yamada, S. Zaima, H. Iwano, Y. Yasuda, "Oxidation of H-terminated Si(100) surfaces studied by high-resolution electron energy loss spectroscopy", Journal of Applied Physics, vol. 77, (1995), pp. 5125-5129.

14) As will be discussed later, the fast oxidation rate in the first stage is due to the energy transfer from the scattered species to the surface. So, we adopted the slow oxidation late to eliminate the effect of

energy transfer.

15) C. R. Helms, B. E. Deal, "The Physics and Chemistry of SiO_2 and the Si-SiO_2 Interface", Plenum Publishing Corporation, New York.

16) T. Fuyuki, S. Muranaka, H. Matsunami, "Initial Stage of Ultra-thin SiO_2 Formation at Low Temperature using Activated Oxygen", Applied Surface Science, vol. 117/118, (1997), pp. 123-126.

17) The attenuation lengths and the inelastic mean free paths of O1s and Si2p photoelectrons are larger than the oxide thickness in Figure 5.7. So, the escape depths of O1s and Si2p photoelectrons are not considered.

18) A. Amirav, M. J. Cardillo, P. L. Trevor, Carmay Lim, and J. C. Tully, "Atom-surface scattering dynamics at hyperthermal energies", Journal chemical physics, vol. 87, no. 3, 1987, pp. 1796-1807.

Summary

This thesis describes the investigation on the atomic oxygen problem that space materials are facing in the low Earth orbit. There are many environmental factors in LEO, however, atomic oxygen causes one of the most crucial problems to space materials. In order to achieve a low risk mission in LEO, the material degradation due to AO collision should be predicted before the mission. For this purpose, two facilities which can provide high-energy, intense AO beam with translational energy of approximately 5 eV (corresponding to an orbital velocity of spacecraft) have been developed. Combining with surface sensitive analytical methods of AES, XPS, and STM, this newly developed facility delivered scientific data, as well as engineering data, which allows us to investigate the surface interaction of AO and space materials. Some of the obtained results were correlated to the experiments flown by the space shuttle. The capability of forming high-energy (5eV) intense atom beam is so unique, the application of this method to surface processing (or modification) were also conducted. The results obtained in this thesis are summarized as listed below.

(1) Two AO beam facilities for *in-situ* surface analysis have been successfully developed. One of the AO facilities used a Q-switched YAG laser and a current-loop-type PSV and equipped with home-build STM and AES. The other AO facility used a TEA CO_2 laser and a solenoid-type PSV, and equipped with XPS. The former system generated AO beam with the mean translational energy of 4.7 eV, and the flux of 4.0×10^{12} atoms/cm^2/s. The flux of AO of this source corresponds to that in the altitude of 500 km in the LEO. The later system was the laser detonation-type AO source originally developed by PSI. This source can deliver a hyperthermal AO beam with translational energy of approximately 5 eV. The AO flux generated by the CO_2 laser-type source was calculated to be over 3×10^{14} atoms/cm^2/s at the sample position of 47 cm away from the nozzle throat which corresponds to that in the altitude of 250 km in LEO. The CO_2 laser-type hyperthermal AO source contains hyperthermal O_2 component as well as hyperthermal AO component. In contrast, a feature of the former system is not to have hyperthermal O_2 component in the beam, even though the AO flux is lower than the laser detonation-type source. [Chapter 2]

(2) Making use of the *in-situ* analysis capability of the target surface for this AO facility, the effect of ambient air exposure on the AO-exposed polyimide was investigated. The experimental results clearly showed that the atomic percentage of C and O at the AO-exposed polyimide film depends on the AO fluence when target surface was kept in UHV. In contrast, ambient air exposure lead to a steady-state surface (C: 65 %, O: 25 %, and N: 10 %) of AO-exposed Kapton-H film not regarding the AO fluences. Also the amount of oxygen before the ambient air exposure was found to be as high as 30 %, and it decreased to 25 % after air exposure. These results suggested the necessary to carry out *in-situ* surface analysis of AO-exposed materials. [Chapter 4]

(3) As for the reaction for making volatile products, the positive and negative roles of the adsorbed oxygen (or preliminary oxidation) were suggested. Namely, the interaction of hyperthermal AO with HOPG and polyimide are mainly etching reaction by forming volatile products such as CO and CO_2, however, the experimental results indicated that the surface oxides were also formed in the reaction. In the AO/HOPG system, the surface oxide coverage reached the saturated value of 0.94 at sample temperature of 300 K. The oxygen coverage decreased with increasing the surface temperature and it reached 0.16 at 570 K. On the other hand, CO and CO_2 from the AO-exposed HOPG surface increased with increasing sample temperature. Therefore, it was considered that the surface oxide prevented the formations of CO and CO_2. [Chapter 3] In contrast, at the AO/polyimide system, the surface oxide also increased with increasing the AO fluence and reached the saturate value. The computer-simulated QCM data strongly suggested that the great fraction of material loss was occurred at the oxidized surface (the mass loss rate was estimated to be two orders larger than that at clean polyimide surface). These experimental results clearly showed that mass loss mechanisms of polyimide was under the influence of the presence of surface oxide. [Chapter 4]

(4) In this thesis, a new reaction scheme of hyperthermal AO considering the surface roughness was proposed based on the STM data. The hillock-like structure was formed on the AO-exposed HOPG surfaces. The formation of the hillock-like structure is thought to be formed under the effect of the directed beam which has high translational energy. The

reaction yield of hyperthermal AO with the atomically flat HOPG (0001) surface was estimated to be 1.0×10^{-3}. However, that of the surface with hillock-like structure was reported to be 0.13 by the flight experiment flown on STS-46. This high reaction yield would be explained by the combination of the multiple bounce effect at the surface covered by hillocks and the appearance of the oxygen-covered prism planes of HOPG due to the formation of hillocks. [Chapter 3]

(5) A potential of the laser detonation-type AO source to the surface processing (or modification) was demonstrated. A Si(100) surface was successfully oxidized in the hyperthermal AO beam even at room temperature. The terminal oxidation thickness reached a few nanometers. All of the oxidation curves at 297 K showed two oxidation stages; the fast oxidation process was followed by relatively slow process. These experimental results suggested that the dominant driving force of the hyperthermal beam oxidation of Si was the increase in lattice temperature due to the energy transfer from the incident AO to the SiO_2 surface. Since the energy transfer is physical process, lattice temperatures of any material surfaces exposed to hyperthermal AO beam were expected to increase due to the energy transfer (depending on the mass of the surface species). It is natural to consider that the increase of lattice temperature at the surface assists many reactions (etching, adsorption/desorption, oxidation or other reactions). Therefore, it was concluded that the energy transfer will help to overcome the potential barrier, and promoted the reaction which is realistic only at high temperatures. This experimental results demonstrated that the laser detonation-type source has a capability to be applied as a new surface processing (or modification) technique at low bulk temperature. [Chapter 5]

Acknowledgement

The author would like to thank Professor Masataka Umeno of Osaka University for his advice and supports throughout this study.

Many thanks are due to Professors Masaaki Yokoyama, Yoshizo Takai of Osaka University for their helpful comments and suggestions.

Grateful acknowledgment is given to Professors Shigenori Kanaya, Shunichi Fukuzumi, Mikiji Miyata, Shozo Yanagida, Yoshiki Ichioka, and Drs. Kiyoshi Yasutake and Takayoshi Shimura of Osaka University for their helpful suggestions.

Special thanks are given to Professor Nobuo Ohmae, and Dr. Masahito Tagawa of Kobe University for their advice and encouragement throughout this study.

Professor Timothy K. Minton of Montana State University and Dr. Alain Paillous of ONERA are gratefully acknowledged for their helpful supports and information on the experiments.

Dr. Hirokazu Tahara of Osaka University is given many thanks for his helpful advice and encouragement.

Mr. Hiroki Hara of Kubota Cooperation is acknowledged for his help with XPS measurements.

Dr. Masashi Arita and Mr. Masao Akiyama of Nissan Motors and Mr. Katsuhiro Kishi of NASDA are all acknowledged for their help with building the facility.

Many thanks are due to Ms. Shirley Chung of Jet Propulsion Laboratory, California Institute of Technology for providing the information on the flight experiment.

Dr. Toshiharu Katayama of Mitsubishi Electric Corporation is acknowledged for supplying silicon samples.

The author wish to thank the members of Applied Surface Science Laboratory, Department of Material & Life Science, Osaka University, in particular, Messrs. Toshiharu Ishida, Koshiro Yamakawa, Toru Suetomi, Junichi Ikeda, Yasuhiko Kurozumi, and Yuichiro Ninomiya, for their supports in experiments.